

AFRL-ML-WP-TR-1998-4021



CORE PROGRAMS OF HIGH-PERFORMANCE COMPOSITE MATERIALS

A. Crasto, D. Anderson, R. Esterline, C. Hill, R. Kim,
W. Lee, W. Price, B. Rice, and A. Roy

University of Dayton Research Institute
300 College Park Avenue
Dayton, OH 45469-0168

APRIL 1998

Interim Report for Period 15 September 1996 – 14 September 1997

Approved for public release; distribution unlimited

19980808661
252

MATERIALS AND MANUFACTURING DIRECTORATE
AIR FORCE RESEARCH LABORATORY
AIR FORCE MATERIEL COMMAND
WRIGHT-PATTERSON AIR FORCE BASE, OH 45433-7734

NOTICE

USING GOVERNMENT DRAWINGS, SPECIFICATIONS, OR OTHER DATA INCLUDED IN THIS DOCUMENT FOR ANY PURPOSE OTHER THAN GOVERNMENT PROCUREMENT DOES NOT IN ANY WAY OBLIGATE THE US GOVERNMENT. THE FACT THAT THE GOVERNMENT FORMULATED OR SUPPLIED THE DRAWINGS, SPECIFICATIONS, OR OTHER DATA DOES NOT LICENSE THE HOLDER OR ANY OTHER PERSON OR CORPORATION; OR CONVEY ANY RIGHTS OR PERMISSION TO MANUFACTURE, USE, OR SELL ANY PATENTED INVENTION THAT MAY RELATE TO THEM.

THIS REPORT IS RELEASABLE TO THE NATIONAL TECHNICAL INFORMATION SERVICE (NTIS). AT NTIS, IT WILL BE AVAILABLE TO THE GENERAL PUBLIC, INCLUDING FOREIGN NATIONS.

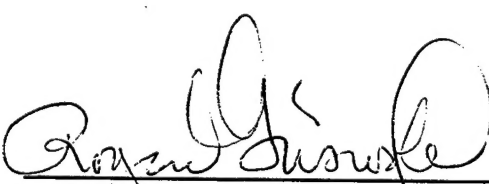
THIS TECHNICAL REPORT HAS BEEN REVIEWED AND IS APPROVED FOR PUBLICATION.



James R. McCoy
JAMES R. McCOY, Research Chemist
Composites Team
Structural Materials Branch



L. Scott Theibert
L. SCOTT THEIBERT, Chief
Structural Materials Branch
Nonmetallic Materials Division



Roger D. Griswold
ROGER D. GRISWOLD, Assistant Chief
Nonmetallic Materials Division
Materials and Manufacturing Directorate

Do not return copies of this report unless contractual obligations or notice on a specific document requires its return.

REPORT DOCUMENTATION PAGE

Form Approved
OMB No. 0704-0188

Public reporting burden for this collection of information is estimated to average 1 hour per response, including the time for reviewing instructions, searching existing data sources, gathering and maintaining the data needed, and completing and reviewing the collection of information. Send comments regarding this burden estimate or any other aspect of this collection of information, including suggestions for reducing this burden, to Washington Headquarters Services, Directorate for Information Operations and Reports, 1215 Jefferson Davis Highway, Suite 1204, Arlington, VA 22202-4302, and to the Office of Management and Budget, Paperwork Reduction Project (0704-0188), Washington, DC 20503.

1. AGENCY USE ONLY (Leave blank)			2. REPORT DATE December 1997	3. REPORT TYPE AND DATES COVERED Interim - 15 Sep 96 - 14 Sep 97
4. TITLE AND SUBTITLE CORE PROGRAMS OF HIGH-PERFORMANCE COMPOSITE MATERIALS			5. FUNDING NUMBERS F33615-95-D-5029 PE 62102F PR 4347 TA 34 WU 10	
6. AUTHOR(S) A. Crasto, D. Anderson, R. Esterline, C. Hill, R. Kim W. Lee, W. Price, B. Rice, and A. Roy				
7. PERFORMING ORGANIZATION NAME(S) AND ADDRESS(ES) University of Dayton Research Institute 300 College Park Avenue Dayton, OH 45469-0168			8. PERFORMING ORGANIZATION REPORT NUMBER UDR-TR-97-168	
9. SPONSORING/MONITORING AGENCY NAME(S) AND ADDRESS(ES) Materials and Manufacturing Directorate Air Force Research Laboratory Air Force Materiel Command Wright-Patterson AFB OH 45433-7734 POC: James R. McCoy, AFRL/MLBC, 937/255-9063			10. SPONSORING/MONITORING AGENCY REPORT NUMBER AFRL-ML-WP-TR-1998-4021	
11. SUPPLEMENTARY NOTES				
12a. DISTRIBUTION/AVAILABILITY STATEMENT Approved for public release; distribution is unlimited			12b. DISTRIBUTION CODE	
13. ABSTRACT (Maximum 200 words) <p>Evaluation of composites and components continued from the previous contract. Materials used in the P4 low cost composite program were evaluated. New formulations for the use of electron beam curing of composites were evaluated. Evaluation of bridge rehabilitation materials; environmental and in service testing was conducted. The hydrothermal aging of AFR700 (polyimide) composites were studied by creep and elevated temperature testing. The CTE of composites was measured by strain gages (a method verified by model systems) and used to predict the thermally induced cracking temperatures and cracks from steady state mechanical loadings. Crack growth in the adhesive layers of double lap shear specimens was shown to shift interfaces during testing. Woven and model weave composites were observed during tensile testing and the corresponding failure mechanisms and damage growth determined. The neural network now includes predictions of reaction rates, degree of cure and viscosity from temperature and dc-resistance measurements with specific volume predictions now being developed. A low cost resin infusion system based on RTM has been developed. X-ray diffraction studies of vapor grown carbon fibers were conducted to the degree of graphitization and other phases. The pressing and sintering of mesophase pitch to form carbon plaques in single stage carbonization and graphitization processing and testing was completed. Several new ways of stabilizing pitch were investigated; better infiltration of the fibers is still needed. A new high-char yield resin continued to be investigated as a carbon-carbon resin. Graphitic foams were characterized as functions of both blowing gas and net-shape processing technique.</p>				
14. SUBJECT TERMS Adhesives, AFR700B, carbon-carbon, carbon-epoxy, carbon-phenolic, carbon fiber, carbonization, composite cyanate esters, e-beam, expert system, fabric, FTIR, graphite-epoxy, graphitic foams, hydrothermal aging, infrastructure, mechanics modeling, microcellular, morphology, neural networks, microscopy, oxidation, pitch, polyimides, process modeling, qualitative process controls, sensors, sintered carbon, space materials, stabilization, thermal analysis, thermal cycling, thermo-oxidative stability, thermosets, and XRD.			15. NUMBER OF PAGES 143	
16. PRICE CODE				
17. SECURITY CLASSIFICATION OF REPORT Unclassified	18. SECURITY CLASSIFICATION OF THIS PAGE Unclassified	19. SECURITY CLASSIFICATION OF ABSTRACT Unclassified	20. LIMITATION OF ABSTRACT SAR	

CONTENTS

Section	Page
1 CHARACTERIZATION OF FIBERS, MATRIX RESINS AND COMPOSITES	1
1.1 COMPOSITE FABRICATION	1
1.2 CHARACTERIZATION OF COMPOSITES AND THEIR CONSTITUENTS	1
1.2.1 P4 Composite Panels and Binder Resin Analysis	1
1.3 THERMAL ANALYSIS	10
1.4 ELECTRON BEAM CURE OF COMPOSITES FOR AEROSPACE STRUCTURES	10
1.5 COMPOSITES FOR INFRASTRUCTURE REHABILITATION	14
1.5.1 Environmental Durability of Adhesive Joints	14
1.5.1.1 Experimental Details	14
1.5.1.2 Failure of Lap-Shear Joints	16
1.5.1.3 Effect of Temperature on Lap Shear Strength	16
1.5.1.4 Effect of Moisture on Lap Shear Strength	17
1.5.1.5 Effect of Thermal Cycling on Lap Shear Strength	18
1.5.1.6 Fatigue Performance of Lap Shear Specimen	18
1.5.2 Rehabilitation of Concrete Beams with Fiber-Reinforced Composites	20
1.5.2.1 Durability of Composite Plate Reinforcement in the Field	20
1.5.2.2 External Reinforcement of Concrete Beams with Composite Rods	23
1.6 LIFETIME PERFORMANCE OF POLYIMIDE COMPOSITES IN AEROSPACE STRUCTURES	26
2 MECHANICS OF POLYMER-MATRIX COMPOSITES	33
2.1 DIMENSIONAL STABILITY OF COMPOSITES AFTER MICRORACKING	33
2.1.1 Measurement of Composite CTE	33
2.1.2 Influence of Microcracking on Laminate CTE	36
2.1.2.1 Analytical Background	36
2.1.2.2 Experimental Results	37
2.1.2.3 Comparison Between Prediction and Experiment	38
2.2 TRANSVERSE CRACKING OF CROSS-PLY LAMINATES	41
2.2.1 Experimental Approach	42
2.2.2 Onset of Cracking under Mechanical Loading	42
2.2.3 Onset of Cracking under Thermal Loading	43

CONTENTS (Continued)

Section		Page
2.3	EXPERIMENTAL INVESTIGATION OF CRACK-FRONT PROFILE IN BONDED COMPOSITE MATERIALS	50
2.3.1	Bonding Process Selection	50
2.3.2	Test Procedure	51
2.3.3	Damage Observation	52
2.3.4	Crack Front Profile	55
2.4.	THREE-DIMENSIONAL MIXED VARIATIONAL MICRO-MECHANICS MODEL FOR TEXTILE COMPOSITES	58
2.5.	COMPARISON OF <i>IN SITU</i> DAMAGE ASSESSMENT IN UNBALANCED FABRIC COMPOSITE AND MODEL LAMINATE OF PLANAR (ONE-DIRECTIONAL) CRIMPING	63
2.5.1	Introduction	64
2.5.1.1	Unbalanced (6:1) Woven Composite Laminate	66
2.5.1.2	Model Laminate	67
2.5.2	Experimental Procedure	68
2.5.3	<i>In Situ</i> Damage Observation	70
2.5.3.1	5HS Unbalanced (6:1) Laminate ($[0]_{2T}$)	70
2.5.3.2	Model Laminate ($[90/0_2]_S$, $[90/0_2/90]_S$, 0.027)	71
2.5.4	Conclusions	77
3	PROCESSING SCIENCE OF COMPOSITES	79
3.1	INTEGRATION OF SENSORS FOR INTELLIGENT COMPOSITES PROCESSING	79
3.1.1.	Neural Network for Prediction of Reaction Rate, Degree of Cure, Viscosity and dc-Resistance	79
3.1.2	Neural Network for Prediction of Specific Volume Change During Cure	79
3.1.3	Thermal Conductivity Measurement	81
3.2	LOW-COST RESIN INFUSION PROCESSING	82
4	CARBON-CARBON AND CARBONACEOUS MATERIALS	84
4.1.	CARBONIZATION OF PITCH AND OTHER CARBON-CARBON PRECURSORS	84
4.2	CHARACTERIZATION VAPOR-GROWN CARBON FIBERS	84
4.3	INTELLIGENT PROCESSING OF CARBON-CARBON	86

CONTENTS (Concluded)

Section	Page
4.4 SINTERED CARBON PROCESSING	87
4.4.1 Sintered Pitch Panels	87
4.4.2 Composite Panel Production	88
4.4.3 Pitch Analysis – Thermoplasticity	90
4.5 STABILIZATION OF PITCH	92
4.5.1 Internal Stabilizers	92
4.5.2 FTIR Studies of Pitch	95
4.5.3 Thermal Oxygenation Study	95
4.6 EVALUATION OF A NEW HIGH CHAR YIELD RESIN	99
4.6.1 SMU Composites	100
4.6.2 In-House Composites	103
4.6.3 In-House Resin Synthesis	104
4.7 PITCH-BASED GRAPHITIC FOAMS	105
4.7.1 Foams Produced Using Nitrogen Gas	105
4.7.2 Foaming Produced Using Carbon Dioxide Gas	107
4.7.3 Modeling of Bubble Growth	107
4.7.4 Foam Net-Shape Processing - Microscopy Studies	109
4.8 AD HOC ACTIVITIES	116
 5 REFERENCES	120
 PUBLICATIONS, PRESENTATIONS AND PATENTS	124

FIGURES

Figure	Page
1 Optical Microscopy Photos of Composite Panels Made by “Budd “Slurry” and “Textron” for the P4 Project	7
2 Bubble Cross-Section in the Budd Slurry Panel	9
3 Dynamic Mechanical Analysis Data for Neat EBC Resins and a Thermally Cured Baseline Epoxy	12
4 Tensile Moduli of Neat EPC Resins and Thermally Cured 3501-6	13
5 Tensile Strength Retention of Neat EBC Resins and Thermally Cured 3501-6	13
6 Sketch of Double-Lap-Shear Specimen	15
7 Lap-Shear Strength of Wet and Dry Specimens as a Function of Temperature	17
8 Composite Plates Bonded to the Lower Surface of an Outer 8.5-m Concrete Beam of a Vehicular Bridge	21
9 Maximum Bending Moments of Aged and Unaged 8.5-m Concrete Beams, with and without External Composite Plate Reinforcement	22
10 Comparison of Maximum Bending Moments of 2.6-m Concrete Beams without External Reinforcement, with Composite Plate Reinforcement and with Composite Rod Reinforcement, vs. Measured Central Deflections	24
11 Comparison of Maximum Bending Moments of 8.5-m Concrete Beams without External Reinforcement, with Composite Plate Reinforcement and with Composite Rod Reinforcement, vs. Measured Central Deflections	25
12 Tensile Modulus of AFR700B Neat Resin vs. Temperature	28
13 Tensile Strength of AFR700B Neat Resin vs. Temperature	28
14 Tensile Stress-Strain Data for Unaged AFR700B Neat Resin at Three Test Temperatures	29
15 Tensile Creep Data from Tests on AFR700B Neat Resin at Three Temperatures, with Three Applied Stresses at Each Temperature	30

FIGURES (Continued)

Figure		Page
16	Fracture Toughness of AFR700B Neat Resin after Hygrothermal Aging in Saturated Steam	32
17	Glass Transition Temperatures of AFR700B Neat Resin after Hygrothermal Aging in Saturated Steam	32
18	Thermal Strain of a $[0]_{8T}$ through Heating and Cooling Cycles	35
19	Thermal Strain of a $[90]_{8T}$ Laminate through Heating and Cooling Cycles	35
20	Variation in CTE of a $[0_2/90_2]_S$ Laminate in Two Normal Directions	37
21	Cross-ply Transverse Crack Unit Cell	38
22	Thermal Strain as a Function of Temperature and Crack Density for a $[0_2/90_2]_S$ Laminate	39
23	Comparison of Experimental and Predicted CTEs	39
24	Micrograph Showing Transverse Cracks in a $[0_2/90_2]_S$ Laminate with Secondary Partial Cracks at/Near the State of Crack Saturation	40
25	Variation of $[0_2/90_2]_S$ Laminate Elastic Properties with Crack Density	41
26	Acoustic Emission Showing Onset of Microcracking for $[0/90/0]$ Laminate	44
27	Acoustic Emission Showing Onset of Microcracking for $[0/90_2/0]$ Laminate	44
28	Acoustic Emission Showing Onset of Microcracking for $[0/90_3/0]$ Laminate	45
29	Acoustic Emission Showing Onset of Microcracking for $[0/90_4/0]$ Laminate	45
30	Micrograph Showing Onset of Transverse Crack for $[0/90/0]$ Laminate	46
31	Micrograph Showing Onset of Transverse Crack for $[0/90_2/0]$ Laminate	46
32	Micrograph Showing Onset of Transverse Crack for $[0/90_3/0]$ Laminate	47
33	Micrograph Showing Onset of Transverse Crack for $[0/90_4/0]$ Laminate	47

FIGURES (Continued)

Figure		Page
34	Steady State Cracking Prediction versus Experiment	48
35	Parallel Plate TMA: Temperature and Viscosity Profiles of FM300-2K Adhesive Using the Manufacturer's Recommended Cure Cycle	51
36	Parallel Plate TMA: Temperature and Viscosity Profiles of FM300-2K Adhesive Using the Modified Cure Cycle	51
37	Specimen Configuration and Representative Strain Gage Locations of the Double Lap-Shear Specimen	52
38	Measured Strains at Locations 4, 5, 6, and 7	53
39	Interlaminar Normal Strains at a Damage Sensitive Location for Several Incremental Loading	54
40	Micrograph (in Fluorescent Field) Indicating Crack Initiation at the Middle Adherend Interface	54
41	Interlaminar Normal Strains at a Damage Sensitive Location for Several Incremental Loadings Beyond Crack Initiation in the Bond	56
42	Edge Micrograph Showing Interface Crack at the Middle Adherend Interface Taken after a Load of 90 Percent of Failure	56
43	Edge Micrograph Showing Interface Crack Moving from One Adherend Interface to the Other	57
44	Crack Front Profile in Two Representative Specimens	57
45	RVE of a 2D Textile Composite	59
45(b)	RVE of the Model	59
46	(a) Schematic of the Weaving Pattern of a Fabric Composite, (b) A Realistic Representation of an RVE of a Fabric Composite where Adjacent Yarns of the Same Weave Patterns Are Squashed Together to Represent a Subregion of The RVE	65

FIGURES (Continued)

Figure		Page
47	Schematic Representation of the Model Laminate	66
48	Cross-sectional Micrograph of the Unbalanced (6:1) Fabric (Woven) Laminate before Loading	67
49	Cross-sectional Micrograph of the Model Laminate	68
50	Specimen Configuration of the Model Laminate Showing Location of the Strain Gages	69
51	Stress-Strain Curves of the Specimens Prepared in the Warp and Fill Directions of the Unbalanced 5HS (6:1) Woven Composite Laminate Subjected to Tensile Loading	69
52	Stress-Strain Curves of the Model Laminate Subjected to Tensile Loading	70
53	<i>In situ</i> Cross-sectional Micrograph of the 5HS Unbalanced (6:1) Woven Composite Specimen at Two Different Locations Indicating Initiation of Yarn Interface Cracks at 65 Percent of Failure Load	72
54	<i>In situ</i> Cross-sectional Micrograph of the 5HS Unbalanced (6:1) Fabric Composite Specimen at Two Different Locations Revealing Delaminations in the Vicinity of Yarn Crimping at 98 Percent of the Failure Load	72
55	Surface of the Warp Specimens of Unbalanced Fabric Composite Revealing Damage Path	73
56	Failure Modes in Warp and Fill Specimens of the 5HS Unbalanced Fabric Composites, Respectively	73
57	Specimen Geometry Description for the Damage Evolution Study	74
58	<i>In situ</i> Cross-sectional Micrograph of the Model Laminate at 37 Percent of Far-Field Strain	75
59	<i>In situ</i> Cross-sectional Micrographs of the Model Laminate at 44 Percent of Far-Field Strain	75

FIGURES (Continued)

Figure	Page
60 (a) <i>In situ</i> Micrograph of the Upper Edge of the Specimen at 90 Percent of the Failure Load (b) An enlarged view of the area in (a) containing the broken fibers	76
61 (a) <i>In situ</i> Micrograph of the Lower Edge of the Specimen at 90 Percent of the Failure Load (b) An enlarged view of the area in (a) containing the broken fibers	78
62 Edge Micrograph of Section AA Shown in Figure 57	78
63 Specific Volume of 3501-6 During Cure	80
64 Specific Volume of 3501-6 During Cure (After Correction for Volume of Noncondensable Gas)	80
65 Specific Volume of 3501-6 During Cure	81
66 Polarized Light Optical Micrograph Showing Distribution of Anisotropic Powder within the Fiber Tows	91
67 SEM of Sintered Microstructure	91
68 Weight Gain of AR Pitch in an Air Oven as a Function of Time at 150°C	96
69 Weight Gain of AR Pitch in an Air Oven as a Function of Temperature for 48 Hours	96
70 Expansion and Penetration for Several Button Made with Pitch Treated at the Temperatures and Times Listed	97
71 Bright-Field and Fluorescence Optical Micrographs of PCP Composites	102
72 Fluorescence Optical Micrograph of a PI Composite	102
73 Comparison between Model Predictions and Measured Porosity versus Volume Expansion in CO ₂ Blown Carbon Foams	109
74 Photographs of “Net-Shaped” Foams	110

FIGURES (Concluded)

Figure		Page
75	Cutting Diagram for the Rectangular Foams Blocks	112
76	Cutting Diagram for the Cylindrical Foam Blocks	113
77	Average Bubble Sizes in the Center of the Foam Specimens as a Function Viewing Direction	115
78	Average Bubble Sizes in the Central Part of the Foam Specimens as a Function of Location from the Center of the Foam to the Outer Part	115
79	Examples of Small-Cell (Left) and Large-Cell (Right) Regions in Foams	117
80	Average Bubble Sizes in the Central Part of the Foam Specimens as a Function of Position from the Center of the Foam to the Outside Edge, Top Edge and Bottom Edge	118
81	Example of Crushed Cells	119
82	Example of Occasional Very Large Cells	119

TABLES

Table	Page
1 Composites Fabricated	2
2 Composite Mechanical Testing for the Period 16 Sep 96 – 15 Sep 97	5
3 Samples Obtained for Analysis	8
4 Fatigue Performance of Lap-Shear Specimens	19
5 Experimental Cracking Loads	48
6 Cracking Temperature Prediction	49
7 Summary of Fabric Compression Studies	83
8 XRD Results for Lot #1 Pyrograf III™ Fiber	85
9 XRD Results for Lot #2 Pyrograf III™ Fibers	85
10 XRD Results for Lot #3 Pyrograf III™ Fibers	86
11 Pressing Conditions and Processing Success	88
12 Physical and Mechanical Results Data	89
13 Pressing Conditions and Additives for Pitch Composites with Internal Oxidants	93
14 Carbonization Results for Pitch Composites Containing Internal Oxidants	94
15 Pressing Conditions for “Fain” Stabilized Pitch Composites	98
16 Carbonization Results for “Fain” Stabilized Pitch Composites	99
17 Summary of Results for PCP Composites	103
18 Processing and Characterization of Foams Processed with N ₂	106
19 Processing and Characterization of Foams Processed with CO ₂	108
20 Net-Shaped Processing Samples	111

FOREWORD

This report was prepared by the University of Dayton Research Institute under Air Force Contract No. F33615-95-D-5029, Delivery Order No. 0001. The work was administered under the direction of the Nonmetallic Materials Division, Materials Directorate, Air Force Research Laboratory, Air Force Materiel Command, with Dr. James R. McCoy (AFRL/MLBC) as Project Engineer.

This report was submitted in December 1996 and covers work conducted from 15 Sep 1996 through 14 Sep 1997.

EXECUTIVE SUMMARY

Routine evaluation of composites and components continued from the previous contract. Materials used in the P4 low cost composite program were evaluated by microscopy and FTIR. The polyester matrix resins used in these glass composites composed the surface bubble material but the fibers were generally well dispersed and well impregnated. The use of electron beam curing of composites for aerospace was continued with the evaluation of new formulations using cationic initiators. DSC on the e-beam cured materials showed incomplete cure relative to thermally cured panels.

Also continued was evaluation of bridge rehabilitation materials. Specimens were subjected to accelerated aging in water and thermally cycled before double lap shear testing was performed. The shear strengths dropped when tested above or below room temperature with the wet specimens performing better than the dry ones due to a plasticization effect which increases toughness. Thermally cycled specimens actually performed better up to 800 freeze-thaw cycles. Fatigue studies were also conducted. Testing of a composite reinforced beam after one year in service showed minimal reduction in strength. The use of embedded rods instead of plates was examined which appears to be a more viable field modification.

AFR700 (polyimide) composites were subjected to accelerated aging studies in saturated steam; the aged samples show slight increase in stiffness at elevated temperatures. Creep studies showed the nonlinear creep is fully recovered on release at ambient and 550°F but is not fully recovered at 650°F.

Strain gages were used to measure the CTE of composites and standard materials such as aluminum, titanium, and a ceramic standard. The multiple location gages gave excellent agreement among themselves as well as the standards. Composites were then transversely cracked and the CTE measured again; the CTE decreases as the number of cracks increase in agreement with model predictions. Transverse cracking was also studied as a function of steady state mechanical loading and thermally induced cracking.

The validity of the double lap shear test was examined. The crack front in these specimens was shown to shift from one adhesive interface to the other as the crack grows; an effect not considered in previous work. The free edge effects in the unidirectional composites tested did not influence the results. Woven and model epoxy composites that simulate a weave in one direction were examined *in situ* during tensile testing; three dimensional stress fields must be considered in these constructions. Initial damage in these composites are at the yarn interface or intra-yarn delamination near the crimp zone in the real woven system but 90° cracks in the model composites: the model composites are still useful for predicting crack growth mechanisms.

The processing science of composites continues to improve with the use of neural network software. The network now includes predictions of reaction rates, degree of cure and viscosity from temperature and dc-resistance measurements; T_g prediction is implicit in the other

predictions. Prediction of specific volume now being developed. A low cost resin infusion system based on RTM has been developed: the pressure assisted vacuum bag resin infusion system pumps resin into a dry preform which can then be cured in an autoclave.

Carbonization control work was limited to expanding the current FTIR database on pitch and problems with the GC/MS. A shorter and heated transfer line was identified as a requirement to prevent condensation of materials along the route between the furnace and the GC/MS apparatus. Characterization of vapor grown carbon fibers by x-ray diffraction showed that the currently manufactured fibers have lower degrees of graphitization than previous fibers. Work on this CRADA with Applied Sciences Inc. is now drawing to a close. Panels of the a high-char yield resin were carbonized and tested; the results are encouraging but the need for panels with lower initial void content is still a problem. Synthesis of the resin was completed to resolve that issue.

The work on internal stabilizers was able to prevent bloating in composites on carbonization but with little pitch matrix left to hold the composite together. An alternative lower temperature oxygen stabilization method was examined. The sintering of pitch work completed the test matrix of pitch from last year and introduced some new experiments and fibers to the testing with limited success. The need to better infiltrate the pitch into fiber bundles was identified as a key issue for all of these projects and is the subject of current pitch prepegging research.

Graphitic foams were examined as functions of blowing gas; a good understanding of the processing parameters which need to be controlled was found. Net shaped foam articles were produced by several means; blowing into a mold proved to be the most promising although the uniformity of the foams was good by any of the processing methods.

SECTION 1

CHARACTERIZATION OF FIBERS, MATRIX RESINS AND COMPOSITES

1.1 COMPOSITE FABRICATION

A list of composites fabricated during this reporting period is given in Table 1.

1.2 CHARACTERIZATION OF COMPOSITES AND THEIR CONSTITUENTS

Composite mechanical testing performed during this reporting period is given in Table 2.

1.2.1 P4 Composite Panels and Binder Resin Analysis

Two glass composite panels and three neat resin binder samples from the P4 research area were brought in for analysis. The panels had undesirable bumps or bubbles on the surface as currently manufactured. The purpose of this study was to determine a) what material forms the bumps on the composite panels and b) is the proposed change in binders for Textron similar to the original binder. Table 3 lists these five samples.

The neat resin samples were examined by DSC, TGA, and FTIR. The panels were photographed, the surface bubbles scraped off for FTIR, and then cut for microscopy samples. Both optical and scanning electron microscopy was performed on the panels. The optical microscopy plugs were mounted using fluorescent dyed potting resin.

The FTIR results showed that the bubbles from the Textron panel were virtually identical chemically to the DSM Neoxil 950 resin. The Budd slurry panel bubbles were likewise chemically the same as the Eastman Kodel 410. The DSM Neoxil 950 and Reichhold ATLAC resins were very much the same chemistry with only slight differences noted in the IR peaks in the fingerprint region. All three binder resins appeared to be aromatic polyesters probably from phthalic acid and an aliphatic oligomeric glycol.

The thermal analysis of the binder resins showed melting points of ~60°C for DSM and Reichhold with a lower heat of fusion and higher melting point (80°C) for the Eastman sample. None of the resins lost any significant weight by TGA until well above 300°C.

Microscopy showed that the resin adequately infiltrated the fiber bundles (see Figure 1) for both manufacturers. The Textron panel had some small areas where the resin may

TABLE 1
COMPOSITES FABRICATED

Material	Panel Size	Orientation	No. of Plies	Remarks
3501-6/AS4	6x6	[0] _{4T}	4	
3501-6/AS4	6x6	[0] _{8T}	8	
3501-6/AS4	6x6	[0] _{16T}	16	2 each
3501-6/AS4	6x6	[0] _{32T}	32	2 ea.
3501-6/AS4	6x6	[0] _{64T}	64	2 ea.
3501-6/AS4	12x12	[0/+45/-45/90] _{2S}	8	
3501-6/AS4	12x12	[+45/0 ₂ /-45/90] _{2S}	24	
3501-6/AS4	12x12	[0/ \pm 45/90] _S	8	2 ea.
3501-6/AS4	12x12	[\pm 45] _{2S}	8	2 ea.
3501-6/AS4	12x12	[0/ \pm 45/90] _S	8	Sensors between 90°'s
3501-6/AS4	12x12	[+45/0/-45/90] _S	8	
3501-6/AS4	6x12	[0 ₂ /+45/-45/0 ₂ /90] _S	14	2 ea.
3501-6/AS4	12x12	[0] _{16T}	16	2 ea.
3501-6/AS4	6x6	[0/90 ₃] _S	8	
3501-6/AS4	6x6	[0/90/90/90] _S	8	
3501-6/AS4	12x12	[0/90] _{4S}	16	3 ea.
AS4-3501-6	12x12	[0 ₂ /90 ₂] _{2S}	24	
AS4-3501-6	6x6	[0] _{12T}	12	2 dielectric sensors
AS4-3501-6	12x12	[0] _{16T}	16	4 ea.
AS4-3501-6	10x10	Resin plate	12	
AS4-3501-6	12x12	[0/90] _{4S}	16	4 ea.
AS4-3501-6	12x12	[0 ₂ /90 ₂] _{2S}	16	4 ea.
AS4-3501-6	12x12	[\pm 45] _{2S}	8	
IM7/5250-4	12x12	0/90/0	3	
IM7/5250-4	12x12	0/90 ₂ /0	4	

TABLE 1 (Continued)
COMPOSITES FABRICATED

Material	Panel Size	Orientation	No. of Plies	Remarks
IM7/5250-4	12x12	0/90 ₃ /0	5	
IM7/5250-4	12x12	0/90 ₄ /0	6	
IM7/5250-4	6x6	[0 ₂ /90 ₂] _S	8	With starter crack
IM7/5250-4	6x9	[0/90/0/90] _S	8	Thermocouple @ midpoint
IM7/5250-4	12x12	[\pm 45] _{2S}	8	2 ea.
IM7/5250-4	12x12	0/90 ₂ /0	8	
IM7/5250-4	12x12	[0] _{8T}	8	8 ea.
IM7/5250-4	12x12	[0] _{4T}	4	2 ea.
IM7/5250-4	12x12	[0] _{3T}	3	
IM7/5250-4	12x12	[0] _{6T}	6	
IM7/5250-4	12x12	[\pm 45] _{2S}	8	2 ea.
IM7/5250-4	12x12	[0] _{24T}	24	1" Kapton @ midpoint
IM7/5250-4	12x12	[0 ₂ /90 ₂] _S	8	
IM7/5250-4	12x12	[0/90] _{3S}	12	
IM7/5250-4	12x12	[\pm 45] _{2S}	8	25 ea.
IM7/5250-4	12x12	[0] _{8T}	8	
IM7/5250-4	12x12	[0] _{16T}	16	2 ea.
IM7/5250-4	12x12	[0] _{20T}	20	2 ea.
IM7/5250-4	12x12	[\pm 45] _{2S}	8	For Ran Kim
IM7/5250-4	12x12	[90/90/+30/-30] _S	8	
IM7/5250-4	1x6	[90] _{8T}	8	
IM7/5250-4	12x12	{\pm 30/90 ₂] _S	8	
IM7/5250-4	6x6	[0 ₂ /90 ₂] _T	4	Russell Cure B no caul plate
IM7/5250-4	6x6	[0 ₂ /90 ₂] _T	4	Cure C 2 runs
IM7/5250-4	6x6	[0 ₂ /90 ₂] _T	4	Run cure B #2

TABLE 1 (Concluded)
COMPOSITES FABRICATED

Material	Panel Size	Orientation	No. of Plies	Remarks
IM7/5250-4	12x12	[0/+45/90/-45] _S	8	
IM7/5250-4	12x12	[0] _{24T}	24	1" Kapton @ mid-plane
AS4C/1995	12x12	[0] _{8T}	8	Teresa's training
AS4C/1995	12x12	[±45] _{2S}	8	Teresa's training
AS4C/1995	12x12	[0/+45/90/-45] _S	8	Teresa's training
AS4C/1995	12x12	[0] _{24T}	24	2 ea. – Teresa's training
AS4C/1995	6x6	[0 ₂ /90 ₂ /0 ₂ /90 ₂ /0 ₄] _S	24	Triangle inserts
AS4C/1995	6x6	[0/0/+45/-45/0/0/90] _S	14	
AS4C/1995	6x6	[0] _{16T}	16	
AS4C/1995	6x12	[0/0/+45/-45/0/0/90] _S	14	Sensor wire inserts
Radel	6x6	[0/+45/90/-45] _S	8	4 ea.
Radel	12x12	[0/+45/90/-45] _{4S}	32	6 ea.
APCIII/AS4	12x12	[±45] _{2S}	8	4 ea.
APCII/AS4	12x12	[+45/0/-45/90] _S	8	4 ea.
Phenolic/SC1008	12x12	[0] _{8T} water solution	8	For Cornelius
XN70/RS-3	4x6	[0 ₄ /90 ₄] _T	8	
XN70/RS-3	6x6	[0/90/0/90] _S	8	
AFR-PEEP2/T650	2x6	Warp aligned flipped	10	Powder on top
AFR-PEEP2/T650	6x9	Warp aligned flipped	10	Powder in middle
AFR700B/T650-35	6x6	[0] ₄ warp aligned	4	
AFR700B/T650-35	6x6	[0] ₈ warp aligned	8	
AFR700B/T650-35	6x6	[0] ₁₂ warp aligned	12	
AFR700B/T650-35	6x6	[0] ₁₆ warp aligned	16	

TABLE 2

COMPOSITE MECHANICAL TESTING FOR THE PERIOD 16 SEP 96 - 15 SEP 97

COMPOSITE	MECHANICAL TESTS				REMARKS
	Tension	Compression	Flex	Shear	
AS4/3501-6	76	21	15	67	25 - CTE, DEF, STR, REL.
AS4/CAT-M	22				
AS4C/1995	15		10	5	
AS4/E-Beam	9				
AS4/CAT B			24		
AS4/CAT B E-Beam			30		
AS4/RT Resin		2		1	
AS4/Various	19		18		
IM7/5250-4	139	10		2	19 Mode I, II
3501-6 Resin	16				1 - CTE
Carbonized Pitch	8				
Carbonized Foam	38	55	13	6	
Carbon/Carbon	20		46		
Sintered Carbon			20		
Carbon Fiber		9	6		
Graphitic Foam	2				
Graphite Tube			1		
Graphite Rods	3		3		1 - CTE
CAT B					1 - CTE
RB 47					1 - CTE, 12 Com. Ten.
CAT M	15				
T300/938	2				

TABLE 2 (Concluded)

COMPOSITE MECHANICAL TESTING FOR THE PERIOD 16 SEP 96 - 15 SEP 97

COMPOSITE	MECHANICAL TESTS					REMARKS
	Tension	Compression	Flex	Shear	Other	
AFR700B	93		10			47 Com. Ten.
Graphite/Epoxy Cloth		4	8			
Fiberglass/Epoxy	86	37	1			
T650-351 AFR-PEPE-2	10			30		
T300 Fabric/AR Pitch	54					
Glass Rod/828-D 230	4					
XN70/RS3	37				8 - CTE, 6 C.T., 1 DEF	
INVAR					1 - CTE	
EPON 828	11				3 - Push out	
Nylon Spectra Vectran					14 - Rupture	
Concrete/Graphite Rod			1			
Aluminum	6	2	2		1 thermal cracking	
Aluminum/Fabric Tube		2				
VGCF/Epoxy		2				
VGCF/3501-6		3				
Hysol EA 9412 Black	4					
N/CAS III	6					
Sigma/7040	1					
Polysulfide Rubber	3					
Leather, Cardboard, Steel	9					

Budd | 100 μm Textron | 100 μm

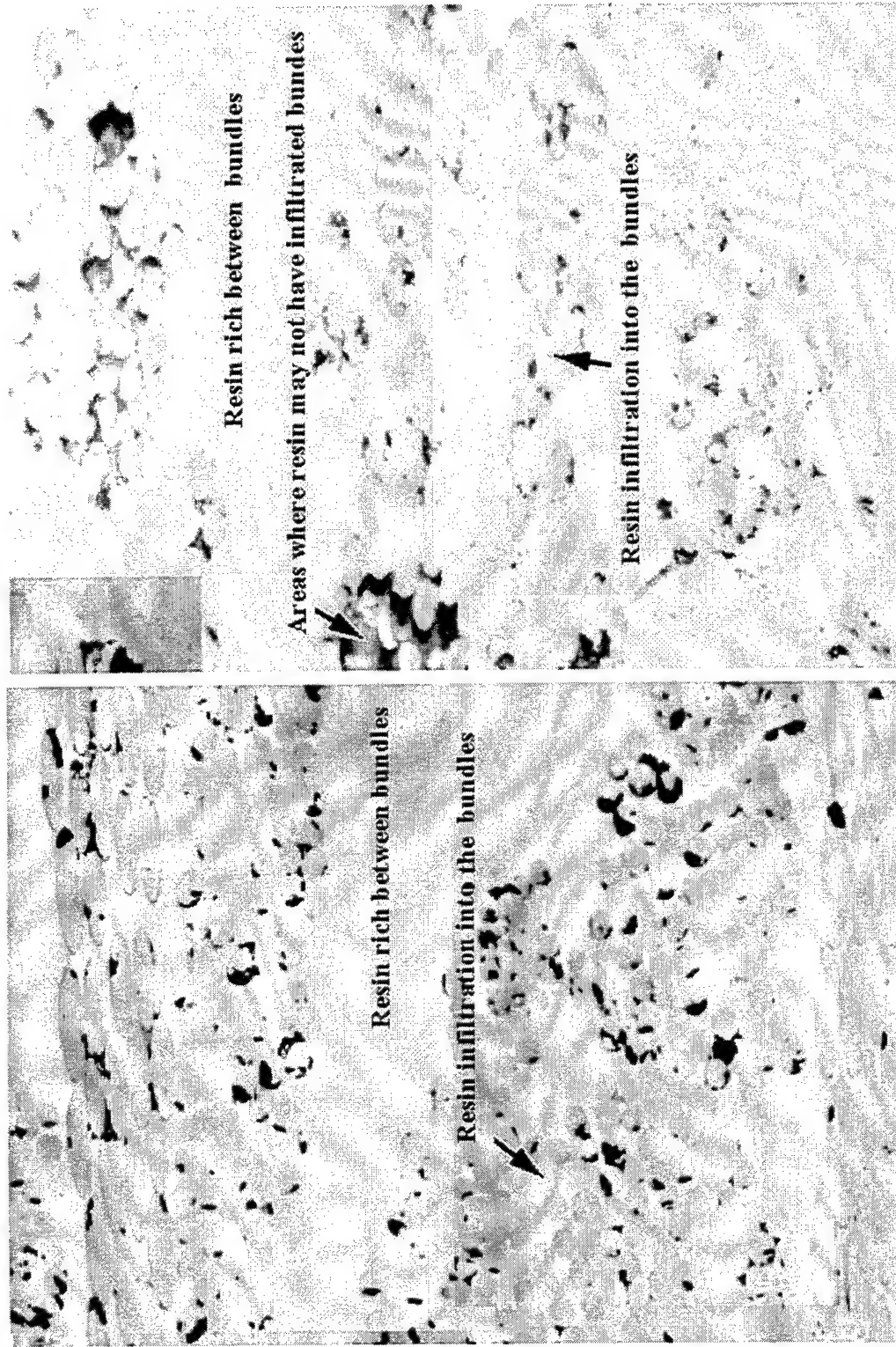


Figure 1. Optical Microscopy Photos of Composite Panels Made by "Budd Slurry" and "Textron" for the P4 Project.

TABLE 3
SAMPLES OBTAINED FOR ANALYSIS

Textron panel (many small bubbles on surface)
 DSM Neoxil 950 binder resin currently used by Textron
 Reichhold ATLAC proposed binder for Textron
Budd Slurry panel (many bubbles, some quite large on surface)
 Eastman Kodel 410 fiber used as binder by Budd

not have penetrated completely. The brittle glass fibers fracture during polishing which can sometimes obscure the true nature of the cause of the observed defects.

At lower magnification, optical microscopy revealed that the larger bubbles of the Budd slurry panel occurred at resin rich areas in the composite. Figure 2 shows the cross-section of a bubble in this panel. The fibers, present as bundles, were all pushed to the opposite side of the panel. Contrast in these micrographs between the composite resin and the potting resin is very low in bright field except when combined with fluorescent microscopy. While not shown here, this combination allowed for easy distinction of these resins under the microscope. The SEM did not show any structure not observed in the optical microscope.

The Textron panel did not have any large bubbles pushing out of the surface but did show more internal bubbles in the region where the surface bubbles had been observed. There also appeared to be several fiber bundles not fully infiltrated by resin; this was more easily observed by SEM.

In conclusion, the bubbles forming the surface defects in these panels are composed primarily of the binder resins. The Budd slurry panel had larger bubbles coming from resin rich areas. The Textron panel had fiber bundles not fully infiltrated by resin but this does not appear to have contributed to the surface bubbles.

Both the DSM and Reichhold resins have the same thermal and chemical properties. Therefore, the proposed change in binders for Textron will probably not significantly change the processing or composite quality.

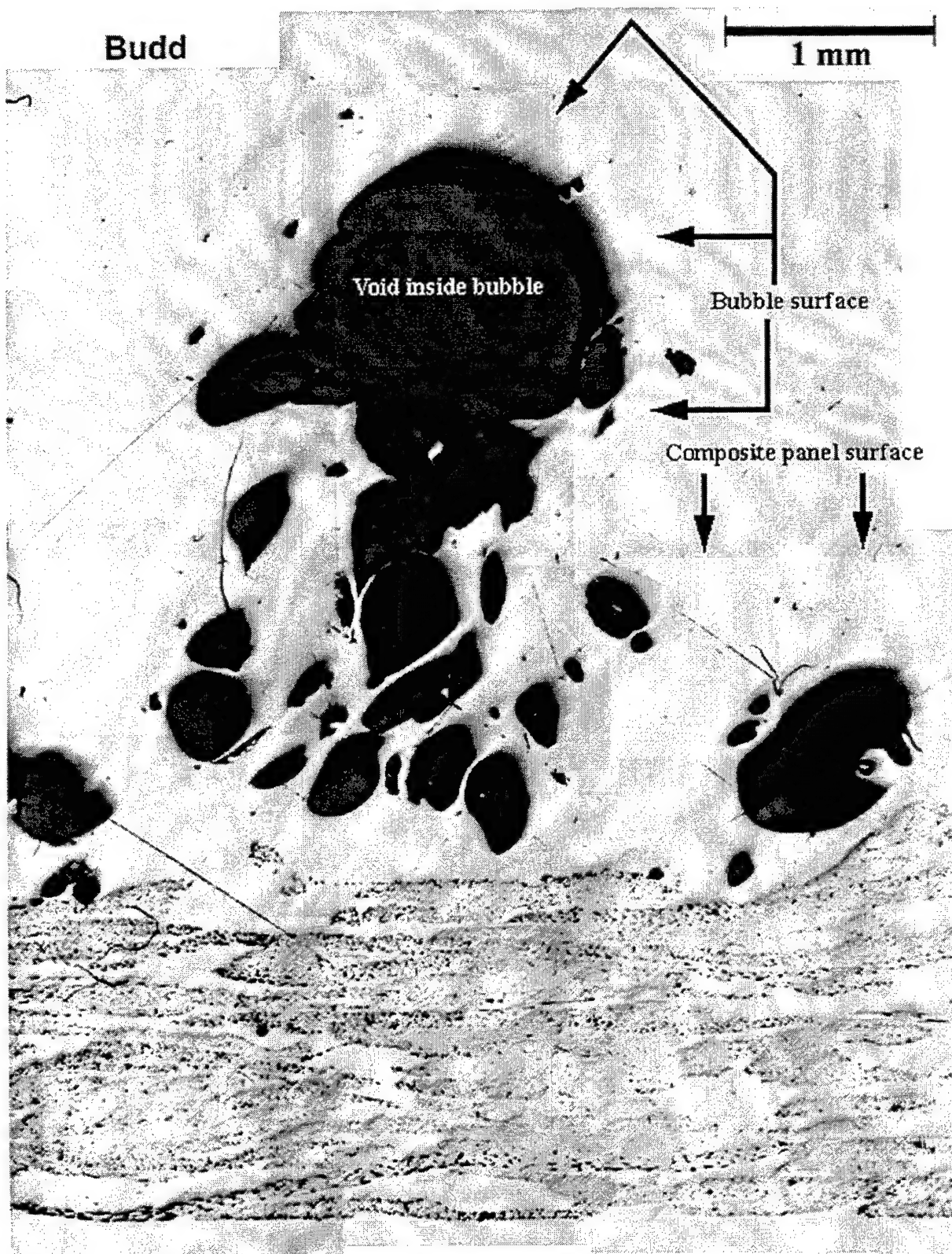


Figure 2. Bubble Cross-Section in the Budd Slurry Panel.

1.3 THERMAL ANALYSIS

A total of 118 experiments were conducted with the Rheometrics RDS-II. The materials investigated include AFR700B, 3501-6, PolyX 1302, CAT-M, Hysol 9460, RB47, EA9396, FM300, LTM 45, AR pitch, SC1008, and ACP.

1.4 ELECTRON BEAM CURE OF COMPOSITES FOR AEROSPACE STRUCTURES

In the electron beam (EB) cure of composites, high-energy electrons from an accelerator initiate polymerization and crosslinking of the matrix resin. This process requires special resin chemistry. Most commercially available EB-curable polymers have ethylene unsaturation and cure via a free-radical mechanism. In epoxies this unsaturation may be introduced through acrylation or methacrylation of the terminal epoxy groups. However, conventional epoxy resins may also be EB-cured through a cationic mechanism, using the appropriate catalyst. EB-cure of composite structures offers a number of advantages over traditional autoclave cure:

- Selectable-temperature curing. Cure at ambient temperature allows the use of inexpensive tooling, while cure at the service temperature of the finished part reduces thermal residual stresses during its use.
- Reduced cure time. A 50-kW accelerator can cure about 1200 kg of composites per hour [1]. This is several times faster than conventional thermal cure in an autoclave, even though composite components are cured in batches as opposed to one at a time with EB cure.
- Improved material handling. EB-cure resins may be stored under ambient conditions and have longer shelf life than thermal-cure formulations. EB processing is continuous and components may be individually cured immediately after assembly, facilitating production scheduling and inventory control.
- Reduced solvent usage and volatile generation.
- Controllable energy input (and lower consumption) with minimal waste. Comparisons of energy required to cure specific composite parts ranging in mass from 0.3 to 16 kg showed a 10 times lower energy requirement for EB cure compared to autoclave cure [2].
- Greater design flexibility. This process allows the cure of selected areas only, the co-cure of different matrix materials, fabrication of unsymmetrical and unbalanced composites, uniform

cure of a range of thickness in the same part, and incorporation of metal inserts and fixtures prior to cure.

All these attractive features combine to create a process which is inherently less expensive than autoclave cure, particularly when high throughput is required. In addition, EB cure could be a potentially enabling technology for the fabrication of very large structures such as cryogenic fuel tanks and for the processing of critical composite space structures, where reduced thermal stresses are essential for dimensional stability in the space environment. Success of this technology, however, is dependent on development of the appropriate material systems and processes. The state of the art can be assessed by selecting one or more specific structural applications and evaluating how EB-cured candidate systems meet their property/performance requirements. Alternatively, the characteristics of state-of-the-art EB-cured material systems may be directly compared with a baseline thermally cured system already in use in aerospace structures. This is the approach followed to evaluate candidate EBC materials for aerospace applications.

In the past year, a new resin formulation, CAT-M from Applied Poleramics, was evaluated for application in aerospace structures. The resin consists of a blend of diglycidyl and tetraglycidyl ethers of bisphenol-A cured with proprietary cationic curing agents. A variety of physical and mechanical characterizations were conducted and some of the results are shown in Figures 3-5, compared to EBC materials evaluated earlier and baseline thermally-cured 3501-6. From Figure 3, it is apparent that CAT-M represents an improvement over its EBC counterparts in mechanical performance at elevated temperature, but is inferior to thermally cured 3501-6. This was validated in tensile tests on the neat resins (Figures 4 and 5). This improvement does not come at the expense of toughness, however, which was found to be equivalent to that of CAT-B from compact tension tests. From DSC tests on neat (uncured and electron beam-cured) resins, CAT-M was found to undergo additional thermal cure to a greater extent than its predecessor, CAT-B. By this thermal measurement technique, EB-cured CAT-B showed a degree of cure of 89 percent, compared to only 75 percent for CAT-M.

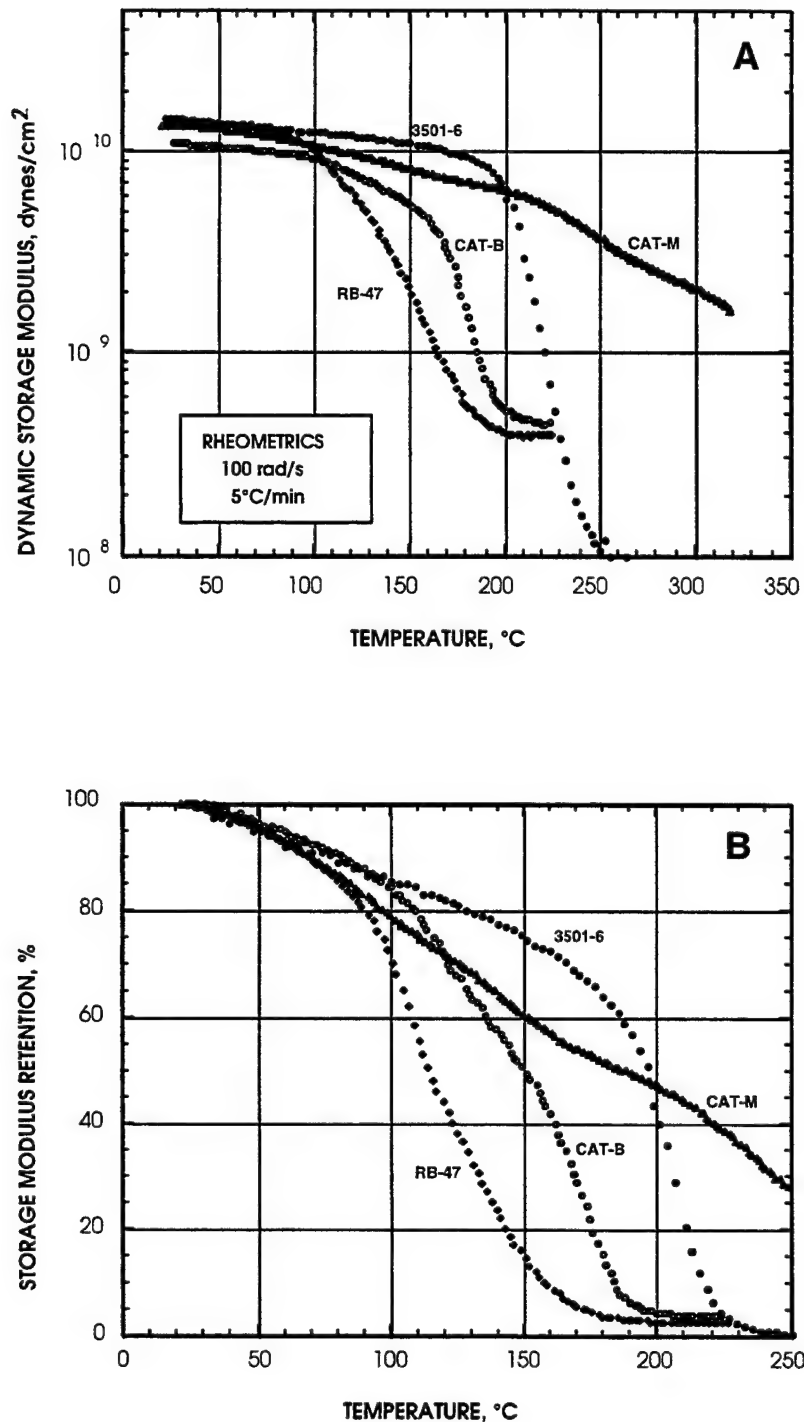


Figure 3. Dynamic Mechanical Analysis Data for Neat EBC Resins and a Thermally Cured Baseline Epoxy. (A) Comparison of dynamic storage moduli, (B) Retention of storage modulus, expressed as a percentage of the initial modulus, as a function of temperature.

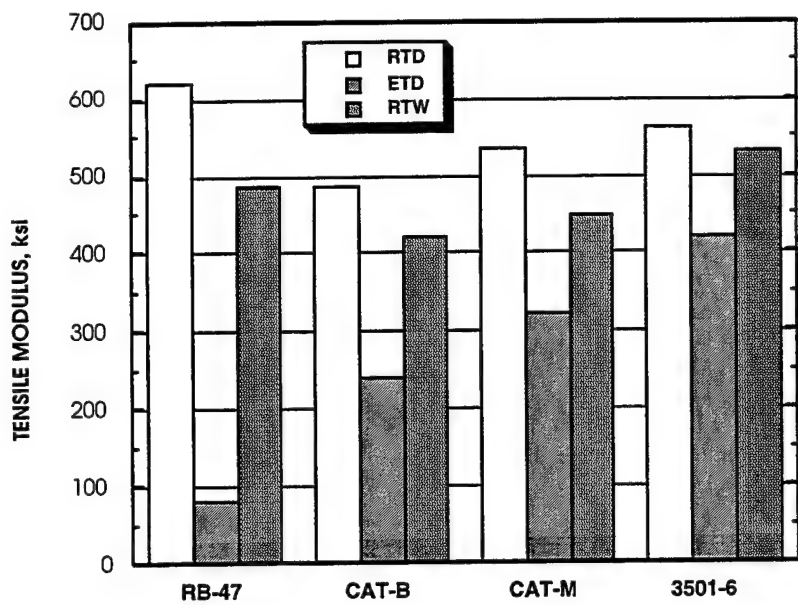


Figure 4. Tensile Moduli of Neat EPC Resins and Thermally Cured 3501-6. (Test conditions: RTD = 23°C, dry; ETD = 121°C, dry; RTW = 23°C, wet, after boiling in water for 24 hours.)

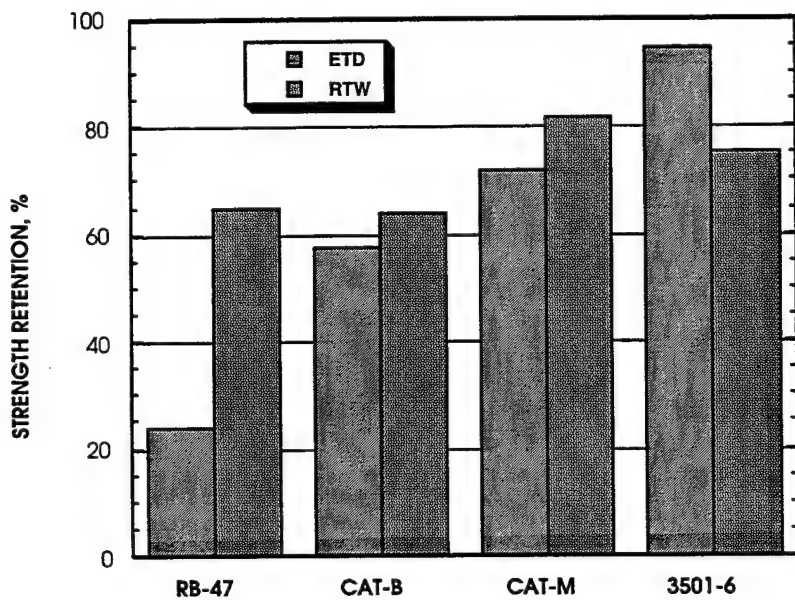


Figure 5. Tensile Strength Retention of Neat EBC Resins and Thermally Cured 3501-6. (Test conditions: ETD = 121°C, dry; RTW = 23°C, wet, after boiling in water for 24 h).

1.5 COMPOSITES FOR INFRASTRUCTURE REHABILITATION

1.5.1 Environmental Durability of Adhesive Joints

Fiber-reinforced composites offer distinct advantages over steel as externally bonded plate reinforcement for concrete structural members. In any structural repair there are two issues which need to be addressed: the mechanical performance of the repaired structure and the durability of the repair over the life of the structure. The mechanical performance can be readily assessed using the appropriate mechanics analysis and experimental validation; evaluating the durability, however, is more complex. In its application, the structure may be subjected to different combinations of temperature and humidity on which are superimposed various monotonic and fatigue loads, exposure to chemicals, etc. To accurately assess the influence of the application environment on repair durability, periodic tests after real-time exposures are required. For structures with long projected lifetimes, such an approach is impractical and leads to long cycle times for the introduction of new materials and processes for repair. Consequently, accelerated aging tests must be conducted. In a recent field demonstration project [3], precured composite plates were bonded to the lower face of concrete beams in a bridge deck with an ambient-cure epoxy adhesive. Load transfer between the plates was achieved through composite doubler joints introduced at four locations along the beam's length. In tests conducted to date, the composite plate has been successfully designed to allow the concrete to fail initially in compression under flexural loading; subsequent failure occurs in the joint. A study was therefore conducted to evaluate the durability of the weakest link in the field rehabilitation scheme, viz. the composite joint, after accelerated exposure to outdoor environmental conditions.

1.5.1.1 Experimental Details

The test specimen selected was a double-lap shear test coupon. The adherends were [0]5 AS4C/1919 composite plates cured between plies of porous Teflon-coated release nylon fabric, which imparted their texture to the composite surface. The adhesive was a two-part epoxy (EA9460 from Dexter Hysol, Inc.), cured at ambient temperature for 48 hours under a pressure of 8 psi to give a uniform bond line 0.15-mm thick. A sketch of the test coupon is shown in Figure 6. Strips of Kapton release tape were utilized during bonding to prevent the

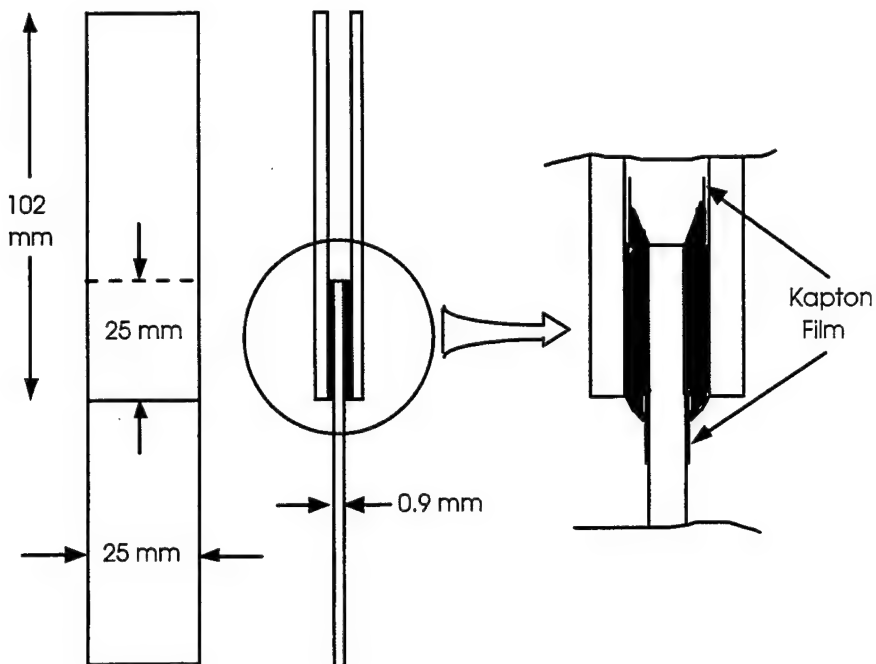


Figure 6. Sketch of Double-Lap-Shear Specimen.

composite/adhesive bond line from extending out of the lap area. The coupons were subjected to a variety environmental conditions to simulate those which could possibly be encountered in the intended application, albeit under an accelerated schedule. One batch of specimens was retained as a control under ambient lab conditions. A second batch was immersed in water at ambient temperature until the specimens were saturated with moisture as determined from periodic measurements of weight gain. A third batch of specimens, immersed in a container of water, was placed in a chamber which was thermally cycled for up to 1000 cycles between -23°C and 27°C.

The entire volume of water in the specimen container was allowed to freeze and then thaw in each cycle. Lap-shear tests were conducted at temperatures ranging from -23°C to 66°C under monotonic loading at a rate of 10 lb/second. Some specimens were also subjected to fatigue loading ($R=0.1$, 10 Hz) at loads of 1800 and 2300 pounds, corresponding to 40 and 50 percent, respectively, of the ultimate strength of control specimens. The glass transition temperature of the cured adhesive was determined by dynamic mechanical analysis and

the coefficients of thermal expansion (CTEs) of the composite plate, neat adhesive and concrete were determined over the temperature range of -40°C to 66°C with strain gages.

1.5.1.2 Failure of Lap-Shear Joints

The surfaces of the composite adherends had the texture of the peel-ply fabric against which they were cured. Mechanical abrasion with 240-grit sandpaper reduced the surface asperities and resulted in only a marginal increase (about seven percent) in average double-lap shear strength. The two-part epoxy adhesive selected for this study was a non-sag, low-viscosity (1500-2500-poise) paste with an adequate working life of 40 minutes. The pressure applied during adhesive cure resulted in a quality bond line with negligible voids. Lap shear tests of the control batch of specimens under ambient conditions resulted in an average lap shear strength of 2240 psi. In general, each lap failed through a combination of shear fracture of the adhesive layer and (predominantly) interfacial failure between the fractured adhesive sections and the two adherends. From an examination of the outer adherends the adhesive layer near the composite free edges appears rough, suggesting some cohesive failure, while the adhesive layer away from these free edges is characteristic of clean interfacial failure. These observations were confirmed by SEM.

1.5.1.3 Effect of Temperature on Lap Shear Strength

Lap shear strengths of unaged (control) specimens were determined over the possible range of outdoor temperatures for this repair application (-23°C to 66°C), and the data are shown graphically in Figure 7. The shear strength appears to peak in the vicinity of 23°C, decreasing by almost 50 percent as the temperature is increased or decreased to the extremes of the test range. Similar trends were observed by other researchers for CFRP composite/epoxy adhesive specimens in double-lap shear tests over the temperature range of -55°C to 132°C [4] and in single-lap tests over the range of 23°C to 90°C [5]. At temperatures below 23°C the failure appears to be predominantly interfacial with the adhesive layer of one lap remaining intact on the outer adherend. The lower strengths with decreasing temperature are in part due to increased tensile stresses in the adhesive due to the mismatch in CTE between the adhesive and [0]5 composite adherend. At temperatures above 23°C the adhesive fractured in a more ductile manner and at random in the lap in combination with interfacial failure. Scanning

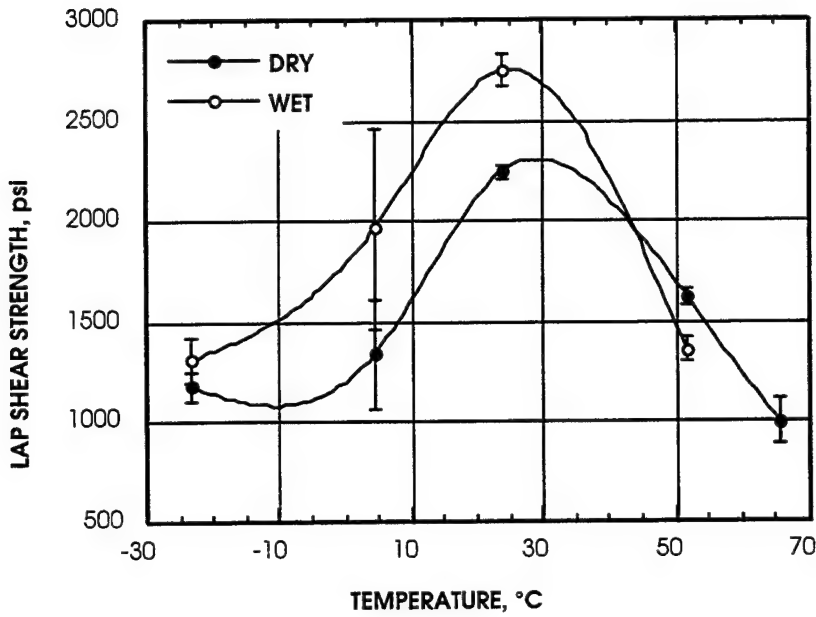


Figure 7. Lap-Shear Strength of Wet and Dry Specimens as a Function of Temperature.

electron micrographs of failed surfaces (tested at 66°C) show evidence of adhesive ductility and tearing. The reduced adhesive strength at this temperature (which is 5°C above its Tg of 61°C) is primarily responsible for the decline in lap shear strength.

1.5.1.4 Effect of Moisture on Lap Shear Strength

The lap shear strength of specimens saturated with moisture at 23°C was measured over the temperature range of -23°C to 66°C, and the results are shown in Figure 7. The general trend is similar to that observed with the dry specimens with the strength peaking around 23°C. At higher temperatures, the resin fractured in a ductile manner in combination with interfacial failure. Plasticization of the adhesive by the absorbed moisture increases its ductility at these temperatures contributing to the lower shear strengths. As with the dry specimens, failure at temperatures below 23°C appeared to be predominantly interfacial with little or no shear fracture of the adhesive layer. In comparing the test results of the wet and dry specimens, however, lap shear strengths of wet specimens below 23°C appear to be significantly higher than those of dry specimens. This may be explained by plasticization of the adhesive by

moisture, which enhances its toughness at room temperature and below when the adhesive is in a glassy state and which reduces residual curing stresses. At temperatures above 23°C the wet shear strength drops off faster than the dry shear strength, since the plasticizing effect of the absorbed moisture reduces the adhesive Tg to near or even below the test temperature. Similar trends were observed in lap shear tests of CFRP/epoxy specimens, before and after hot/wet conditioning, over the temperature range of 23°C to 90°C [5].

1.5.1.5 Effect of Thermal Cycling on Lap Shear Strength

Differences in CTE between the concrete, adhesive layer and composite plate reinforcement induce stresses in these materials and at the corresponding interfaces when a repaired structure is exposed to temperatures above or below the ambient (or cure) temperature. Cycling between outdoor temperature extremes, in the presence of moisture, puts additional stress on the structure due to the expansion of absorbed moisture as it freezes. This thermal cycling is akin to the imposition of mechanical fatigue loading which may degrade the adhesive bond performance in service. To simulate the influence of the outdoor thermal environment on composite joint strength, specimens were subjected to a number of accelerated freeze-thaw cycles between -5°C and 20°C. Specimens were withdrawn periodically from this environment and tested at 23°C. Failure in all cases was predominantly interfacial with very little adhesive residue on the mating adherend. Contrary to expectations, there is a steady increase in lap shear strength with thermal cycling until it appears to plateau after about 800 thermal cycles at a value approximately 15 percent higher than the control sample. This is possibly due to an increase in adhesive toughness with increasing moisture pickup during thermal cycling, through plasticization of the resin in its glassy state at room temperature. As was seen earlier, the lap shear strengths of moisture-saturated specimens at 23°C are 23 percent higher than corresponding (dry) control specimens.

1.5.1.6 Fatigue Performance of Lap Shear Specimen

Composite joints in plate reinforcement of concrete bridge beams will be subjected to fatigue loading as live loads pass over the bridge, and their fatigue life is therefore an important consideration in material selection and design. The fatigue life of lap-shear specimens was determined at fatigue stresses of 40 percent and 50 percent of the lap shear

strength of control specimens. The cycles to failure at each stress level (Table 4) are low in comparison to the expected life of the structural repair of a bridge beam. However, the fatigue stresses are substantially higher than a joint might experience in this particular application and were selected primarily to determine the influence of environmental exposure. Moisture-saturated specimens tested to failure at the higher stress level displayed no appreciable difference in fatigue life compared to the corresponding control specimens. Failure of all fatigued specimens appeared to have initiated at the free edge, in the adhesive near the composite surface, across the entire specimen width. This failure appeared to propagate inward with increasing fatigue cycles until the specimen failed catastrophically at the interface.

TABLE 4
FATIGUE PERFORMANCE OF LAP-SHEAR SPECIMENS

Conditioning	Cycles to Failure at 900 psi	Weibull Parameters	Cycles to Failure at 1150 psi	Weibull Parameters
None	35938 61547 69269 70039 90884 91332 408340	$\alpha = 1.2$ $\beta = 127,014$	961 4287 4603 4837 5108 5200 20037 24150 28546	$\alpha = 1.1$ $\beta = 11,308$
1000 thermal cycles			4402 5357 8842 34067	$\alpha = 1.2$ $\beta = 14,077$

1.5.2 Rehabilitation of Concrete Beams with Fiber-Reinforced Composites

Over the last two years appropriate composite and adhesive M&P has been developed in the lab [6] and implemented in the rehabilitation of a concrete box-beam bridge in the field [3]. In the latter study, composite plates were bonded to the lower face of 8.5-m concrete beams in a bridge deck, across the entire span, with an ambient-cure epoxy adhesive. Doubler joints were introduced at four locations along the beam's length to connect the composite plates. Flexural tests showed a significant increase in maximum bending moment of such an externally reinforced beam compared to a beam without composite reinforcement. In the past year, the durability of this field reinforcement was evaluated.

1.5.2.1 Durability of Composite Plate Reinforcement in the Field

Rehabilitated beams [3] were retained in service (with corresponding exposure to the elements, temperature fluctuations, deicing chemicals and static and dynamic loads for one year. Over this period of time, bond integrity was monitored using an acoustic tap-hammer technique to detect regions where the composite plate debonded from the adhesive layer. Measurements were made one, three and 10 months after the rehabilitation. Change in the debonded area with time is shown in Figure 8 for regions corresponding to a plate near the end of the beam and an adjacent composite doubler joint. The percentage of debonded area increases slightly with time from 1 to 10 months, although with the lack of a baseline (0 months) it is unclear if the debonded areas documented after the first month of exposure were actually present immediately after adhesive cure or generated in the first month of service. Application of a vacuum bag (and the corresponding 50-67 kPa of air pressure) can deform a thin composite plate during adhesive cure to conform to a curvature in the beam, giving rise to interlaminar tensile stresses at the bond line (after adhesive cure and removal of the vacuum bag) as the composite attempts to return to its original shape. These stresses could give rise to initial debonding. If this is true, additional work is necessary to optimize the applied pressure during adhesive cure; it must be large enough to ensure adequate contact and wet out of the adherends by the adhesive (and minimal voids), but not too large to generate unacceptable stresses after cure, resulting in composite/adhesive debonding.

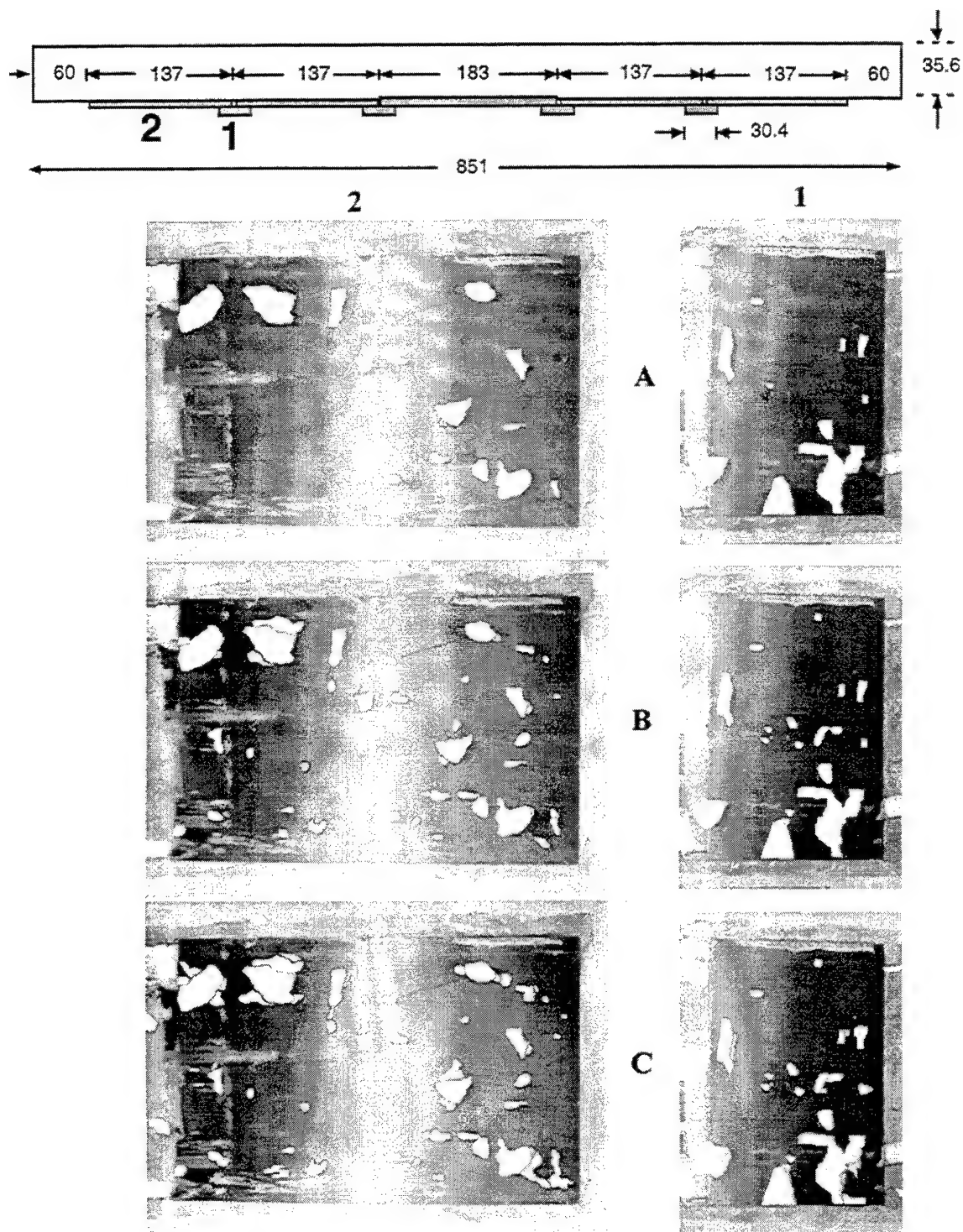


Figure 8. Composite Plates Bonded to the Lower Surface of an Outer 8.5-m Concrete Beam of a Vehicular Bridge. Debonded areas between composite and adhesive are shown in black. (1) composite bonded to concrete; (2) composite bonded to composite in a lap joint; (A) one month of exposure; (B) three-months exposure; (C) 10-months exposure.

After a year in service, one of the exterior externally reinforced beams of the bridge was removed and tested in flexure under conditions identical to those employed for the baseline beams. A comparison of the test results with those of the baseline beams is shown in Figure 9. As is evident from the plot, a year's exposure to the outdoor application environment (and the resulting increase in composite/adhesive debonding) resulted in a minimal reduction in the maximum bending moment of the beam. As with the unaged, externally reinforced beam, ultimate failure was preceded by longitudinal splitting of the [0]5 composite plate and precipitated by fracture of the concrete in compression and instantaneous failure of the composite/composite lap at an inner doubler joint. Which of these two failure events occurred first is uncertain, although comparison with earlier tests [3] appears to suggest the latter.

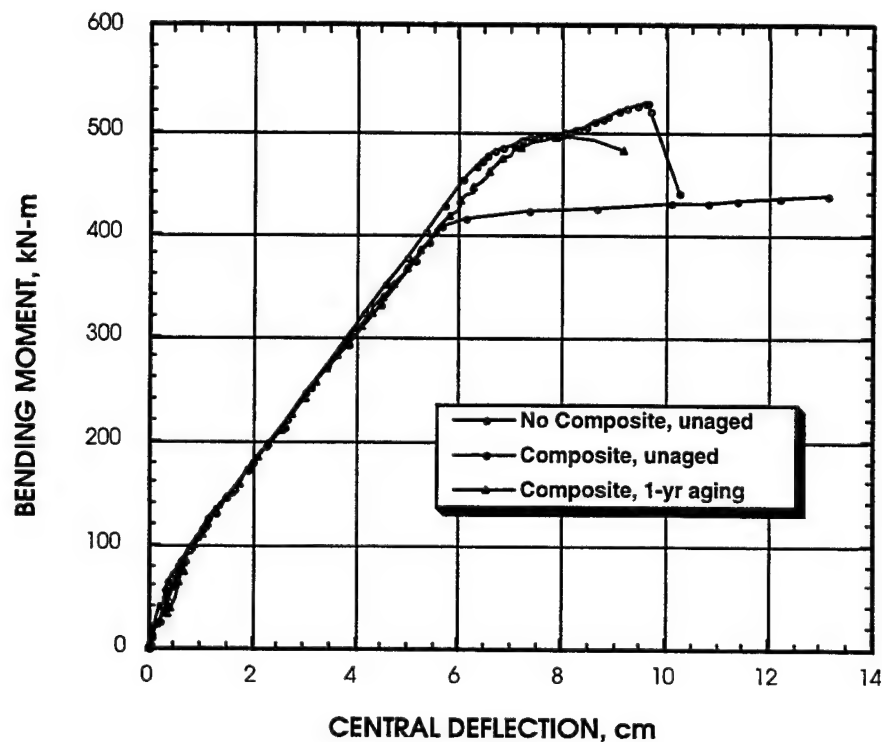


Figure 9. Maximum Bending Moments of Aged and Unaged 8.5-m Concrete Beams, with and without External Composite Plate Reinforcement.

Post-failure examination of the composite/composite lap region revealed areas between composite and adhesive that were initially unbonded in addition to those which debonded later, in service.

1.5.2.2 External Reinforcement of Concrete Beams with Composite Rods

There are a number of disadvantages to employing composite plate reinforcement for the rehabilitation of concrete bridge beams:

- Plates have to be fabricated in sizes that are practical and convenient to transport to the field site, necessitating the development of efficient composite joining techniques for beams with long spans.
- Plate reinforcement typically covers the entire lower surface of the rehabilitated beam, restricting the drainage of absorbed water in the concrete; accumulation of this water at the bond line accelerates its degradation.
- Optimum bonding requires careful and consistent surface preparation of the plate and application of pressure during adhesive cure, to promote intimate contact between adhesive and adherends and minimize voids.
- Free-edge, thermal and residual stresses, in conjunction with the service environment, can promote plate debonding and consequent loss of reinforcing capability over time.

Some of these disadvantages can be overcome by using composite rods (of the same cross-sectional area as the plate) embedded in parallel, longitudinal grooves cut into the tensile face of the beam. Continuous lengths of pultruded rods can be transported to the field in rolls and cut to the necessary length, thereby avoiding composite joints. Since the rods cover a small fraction of the beam's lower surface, drainage of absorbed water is not hindered. The ratio of composite bonded surface to volume is substantially lower than for a plate; this, coupled with the fact that the rods are completely embedded in the adhesive makes them less susceptible to interfacial degradation in service. Pultruded rods are also less expensive to fabricate than precured composite plates and easier to employ in the field, requiring no applied pressure during adhesive cure.

In our work, unidirectional pultruded T-300/vinyl ester rods (8-mm dia.) from DFI Pultruded Composites, Inc. were used as the reinforcement. The adhesive used was a

two-part epoxy (EA9460 from Dexter Hysol, Inc.) which cures under ambient conditions. Test beams, 2.6 m and 8.5 m in length were the same as used in earlier studies [3,6]. Rectangular grooves, 12.7 mm deep and 10.2 mm wide, were machined into the tensile faces of these beams with a portable masonry power cutter and lined with beads of the epoxy adhesive. Composite rods, the length of the beam, were sanded, wiped clean with acetone, and embedded in the epoxy within the grooves. The adhesive was then allowed to cure overnight under ambient conditions. The beams were tested in accordance with ASTM C78-84, as described in earlier reports [3,6].

In initial studies, four composite rods (with a total cross-sectional area of 1.97 cm^2) were used in 2.6-m beams to replace the plate (1.45 cm^2 cross-sectional area) employed in earlier studies. The larger area of the reinforcing rods was compensated by their closer proximity (in grooves) to the beam's neutral axis. Figure 10 shows a plot of beam bending moments vs. central deflection, comparing the baseline beam (without composite reinforcement) to beams with external composite plate and rod reinforcements. The test data for the two

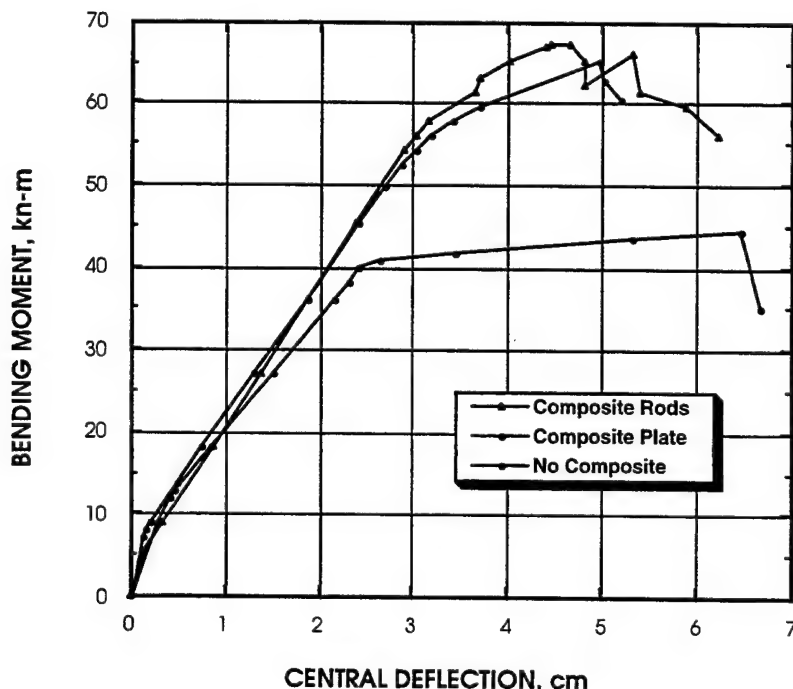


Figure 10. Comparison of Maximum Bending Moments of 2.6-m Concrete Beams without External Reinforcement, with Composite Plate Reinforcement and with Composite Rod Reinforcement, vs. Measured Central Deflections.

reinforcement types are similar. The failure modes, however, were different. Ultimate failure in both beams initiated with compression fracture of the concrete. In the plate-reinforced beam, secondary, catastrophic failure occurred almost instantaneously through composite fracture or composite/composite lap failure. In the rod-reinforced beam, however, secondary failure was noncatastrophic, with limited debonding and partial fracture of the embedded rods, allowing the beam to sustain the applied load with gradual deformation up to the limits of the test fixture. Total extension of the rods during loading did not exceed 1 percent, and post-failure examination revealed no slippage of the rods at the beam ends.

The success with the rod reinforcement of 2.6-m beams led to a scale-up of this reinforcing scheme to 8.5-m beams. Eleven composite rods (with a total cross-sectional area of 5.43 cm^2) were embedded in parallel grooves equally spaced on the lower surface of the beam. This beam was loaded in flexure, under conditions similar to those employed for the baseline 8.5-m beams (without composite and with composite plate reinforcement), and the data are displayed in Figure 11. The beam with rod reinforcement stacks up well against the beam

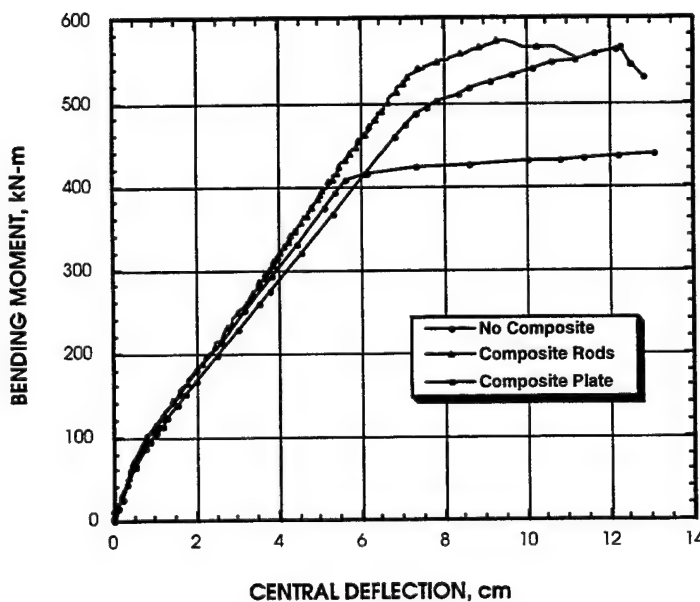


Figure 11. Comparison of Maximum Bending Moments of 8.5-m Concrete Beams without External Reinforcement, with Composite Plate Reinforcement and with Composite Rod Reinforcement, vs. Measured Central Deflections.

with plate reinforcement, even though the comparison favors the latter because of its higher composite cross-sectional area (6.13 cm^2). For an equivalent or slightly larger rod area (to compensate for the closer proximity of the rods to the beam's neutral axis), the beam would have a significantly higher maximum bending moment (at ultimate failure) compared to a beam with plate reinforcement. This difference in maximum bending moments may be explained by the differences in failure modes. In the beam with plate reinforcement, it appears that premature lap-joint failure triggered ultimate failure of the beam; in the beam with rod reinforcement, the concrete failed first in compression, at a higher applied bending moment, followed by noncatastrophic secondary failure events (partial rod debonding and fracture).

1.6 LIFETIME PERFORMANCE OF POLYIMIDE COMPOSITES IN AEROSPACE STRUCTURES

The properties of polyimide resins and composites are adversely influenced by exposure to hygrothermal environments as a result of physical degradation and changes in the cured resin chemistry. Aerospace structures made from these materials are frequently subjected to cycling between ambient and hygrothermal environments with a cumulative deterioration in structural performance over the life of the structure. To accurately predict the lifetime performance of these structures, it is necessary to quantify the changes in key mechanical properties and then use the data in conjunction with a life prediction model. Changes in the glass transition temperatures of these materials as a function of hygrothermal exposure has been well documented; however, how these changes influence mechanical performance over the spectrum of potential service temperatures has not been established. From earlier studies, it was found that extensive hydrolytic degradation of polyimide resins renders these materials more brittle. In addition, fiber-matrix interfacial bond strength, while low to begin, is further reduced after hygrothermal exposure. Consequently, key composite mechanical properties identified as being sensitive to the extent of hygrothermal degradation are the matrix resin toughness, fiber-matrix interfacial bond strength, and creep at elevated temperatures. Changes in these properties were followed as a function of hygrothermal degradation and correlations sought with a standard measure of the extent of degradation, namely the drop in the glass transition temperature.

Specimens were subjected to accelerated hydrolytic aging in a saturated steam environment at various temperatures and for various lengths of time. Tests conducted include

fracture toughness and creep measurements on neat resin, and 90° flexure of unidirectional carbon fiber-reinforced composites. The results from aged specimens were compared with those from unaged baseline specimens.

Figures 12 and 13 show plots of the baseline static stiffness and strength, respectively, of the neat resin at three test temperatures. On the same plots are shown the corresponding data for specimens aged for 24 hours at 150°C in saturated steam. From these figures, it can be seen that both stiffness and strength drop off with temperature, as expected, although the aged specimens show an increase in both strength and stiffness compared to the corresponding baseline specimens. Figure 14 shows representative stress-strain data at three test temperatures. All curves are nonlinear, with the nonlinearity increasing with the test temperature. The difference in stress-strain behavior between as-processed and aged specimens is negligible at room temperature, but becomes noticeable at the elevated temperatures. A slight increase in stiffness is observed for the aged specimens.

Tensile creep tests were conducted at 23, 500, and 650°F in an air-circulating oven mounted on an MTS test machine. A specimen was allowed to equilibrate at the test temperature before being instantly loaded to the desired creep load and maintained under constant load for a predetermined period of time (60 min.). The test machine was operated under load control which ensured minimum fluctuation in the applied load. Three creep loads were selected at each test temperature to investigate the nonlinear creep behavior. Load and strain were continuously recorded as functions of time on an X-Y recorder for the first ten minutes and intermittently at ten-minute intervals thereafter. Figure 15 shows the total strains (instantaneous and creep) as a function of time for each test temperature. From these plots it is evident that the creep strain is nonlinear for these loads and increases with temperature. It was also observed that the recovery of creep strain was almost complete in tests conducted at 23°C and 500°F, whereas a considerable portion of the creep strain was not recovered at 650°F. This creep study will be continued to include lower creep loads and specimens aged for longer periods of time.

The apparent fracture toughness of the neat resin, K_Q , was also determined from compact tension tests. Specimens were tested under ambient conditions after aging for 2 to 196 hours at

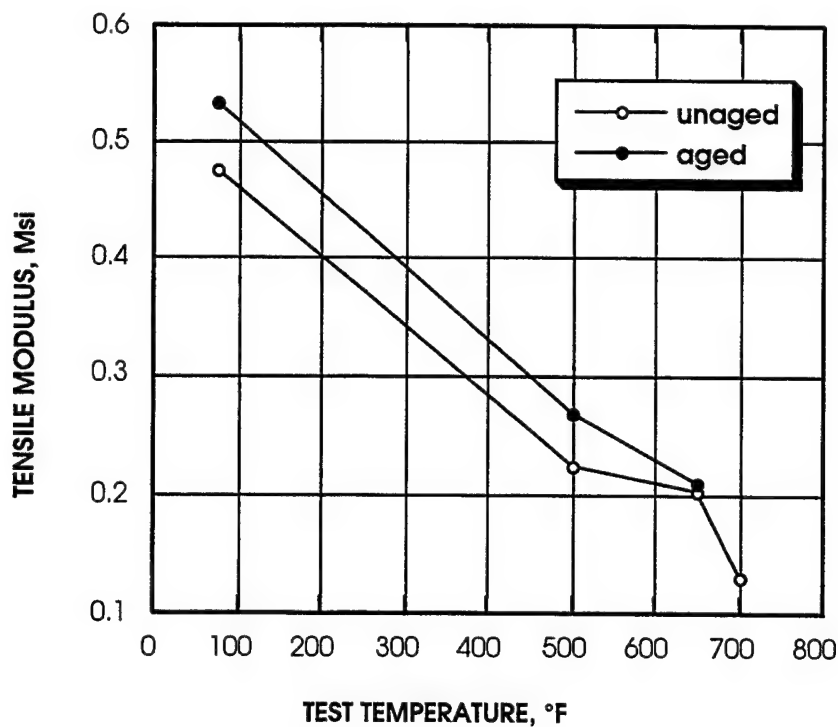


Figure 12. Tensile Modulus of AFR700B Neat Resin vs. Temperature.

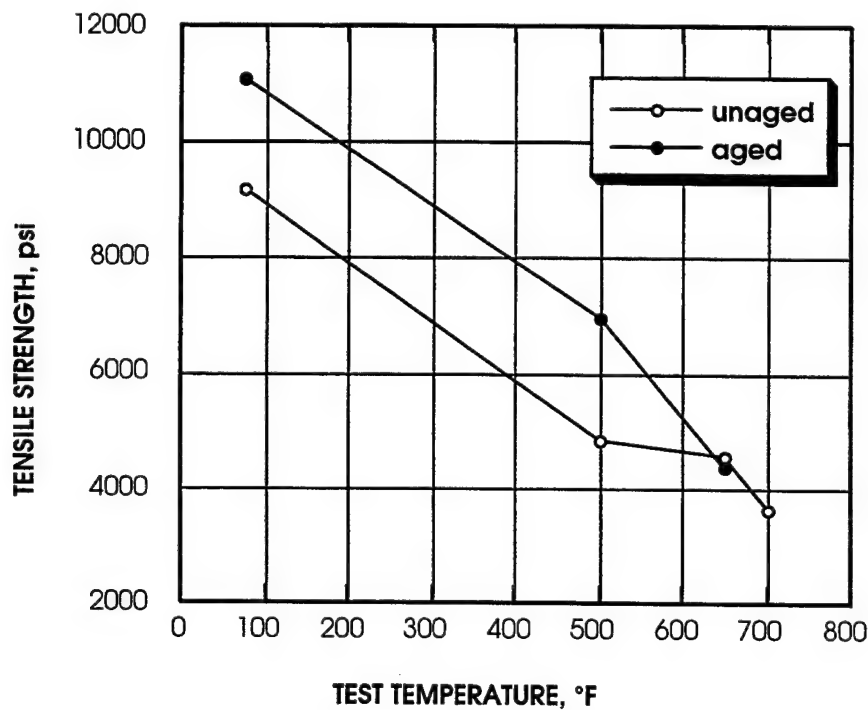


Figure 13. Tensile Strength of AFR700B Neat Resin vs. Temperature.

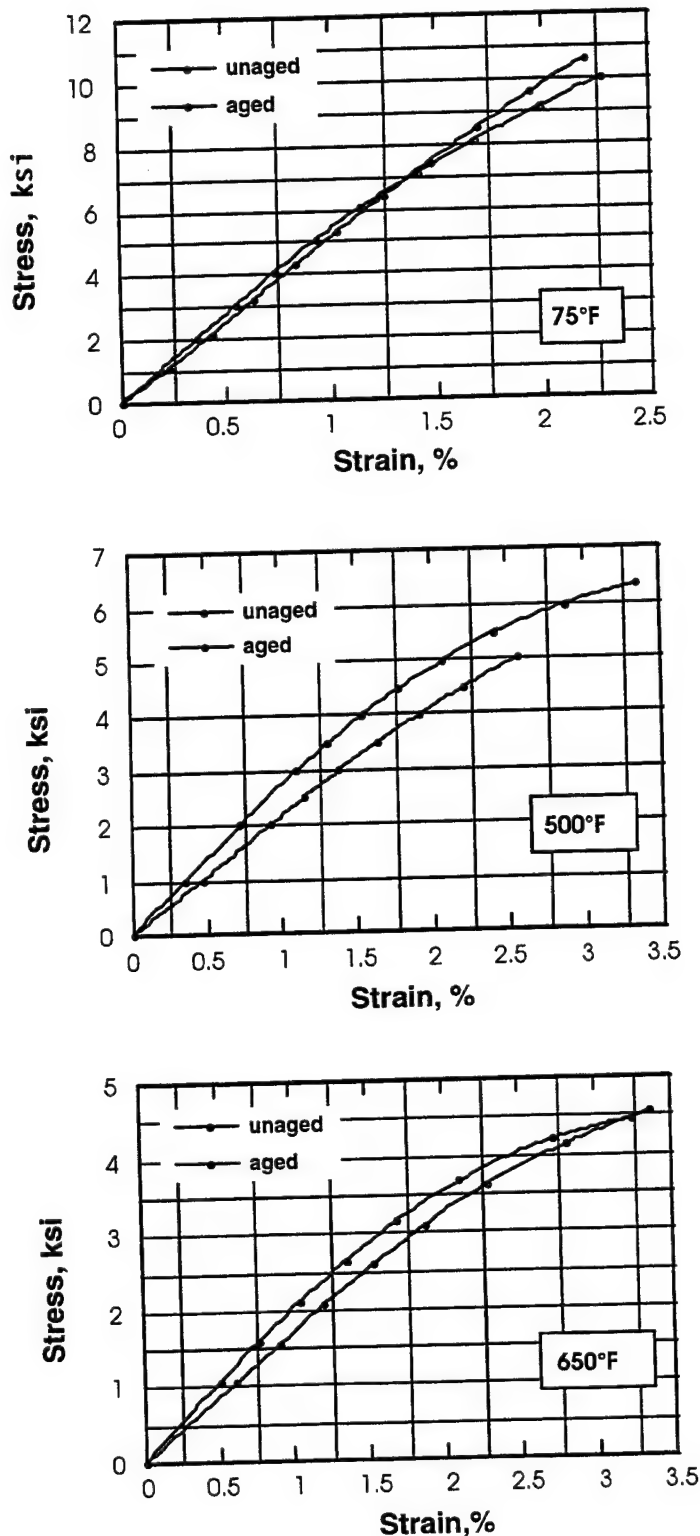


Figure 14. Tensile Stress-Strain Data for Unaged AFR700B Neat Resin at Three Test Temperatures.

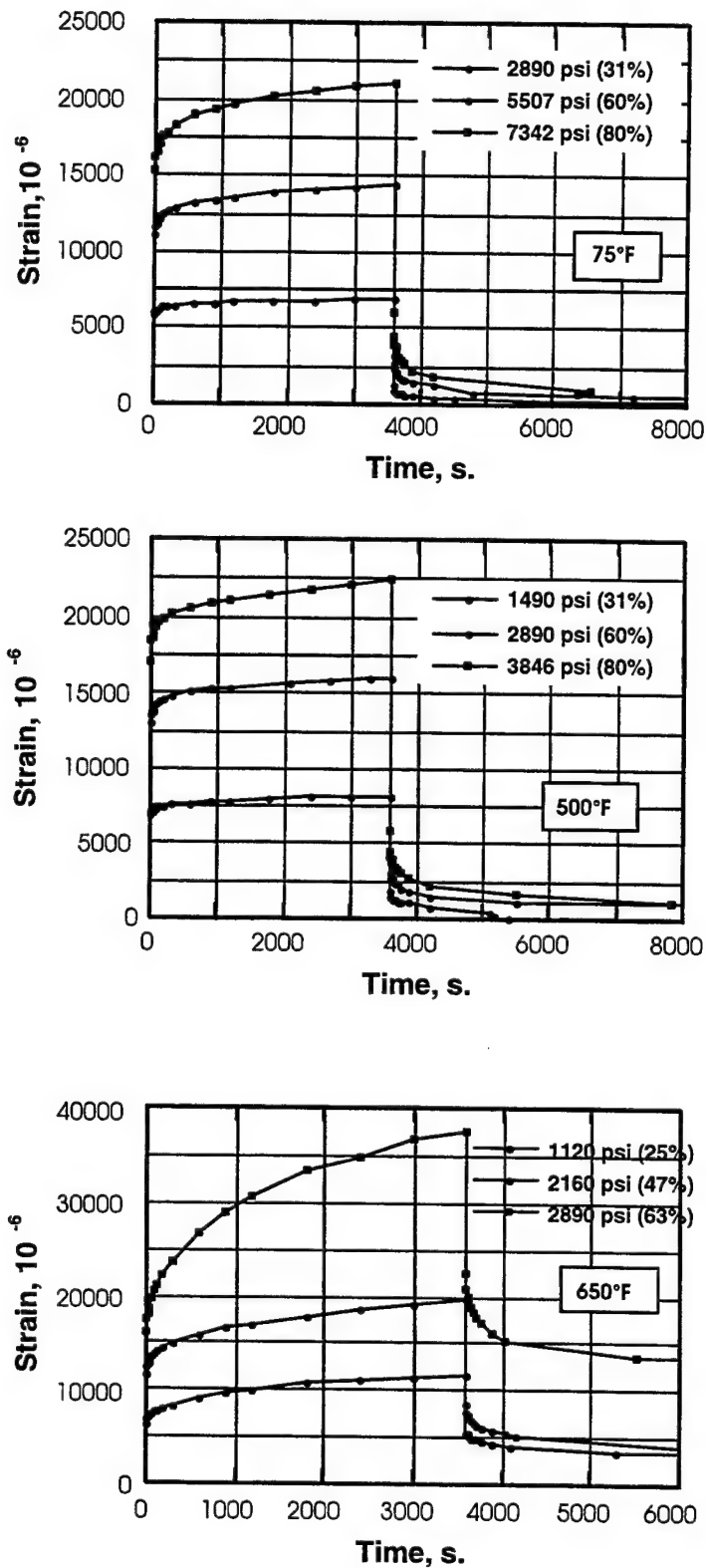


Figure 15. Tensile Creep Data from Tests on AFR700B Neat Resin at Three Temperatures, with Three Applied Stresses at Each Temperature.

temperatures ranging from 150°C to 200°C. The resulting data are plotted in Figure 16. The corresponding glass transition temperatures (taken from the G" peaks of dynamic mechanical analysis tests) are plotted in Figure 17. Both plots show similar trends: the property declines more rapidly and to a lower value with increasing aging temperature. Attempts to extend the data out to longer aging times at each test temperature were unsuccessful as this caused significant microcracking, making testing impossible. This study will be continued to include additional time/aging temperature combinations.

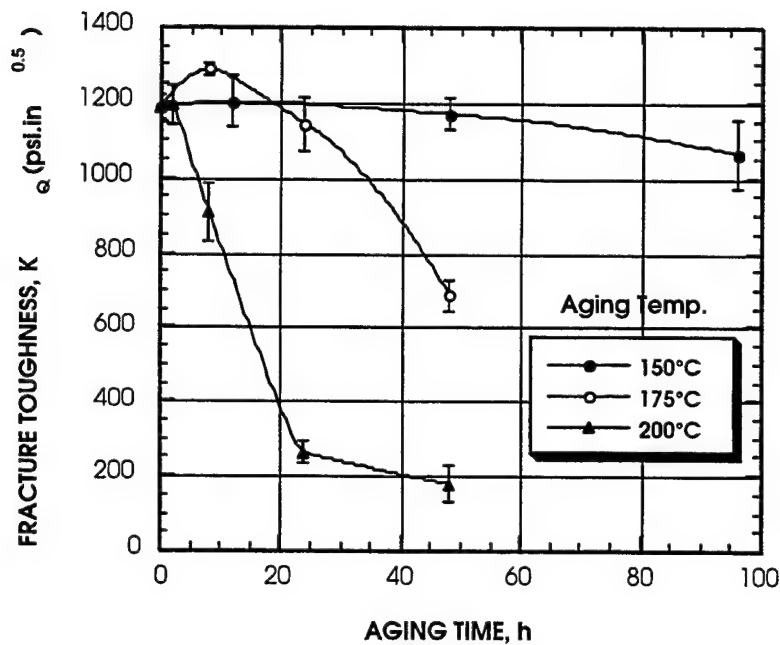


Figure 16. Fracture Toughness of AFR700B Neat Resin after Hygrothermal Aging in Saturated Steam.

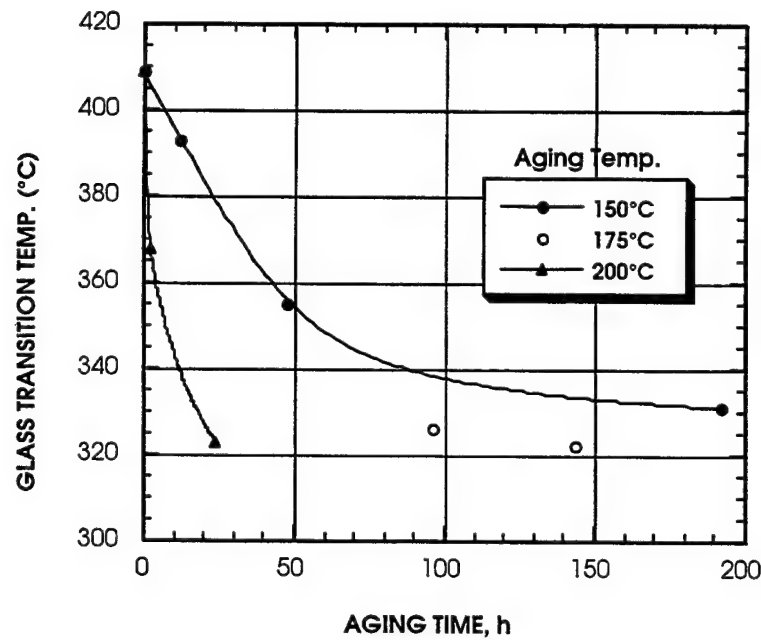


Figure 17. Glass Transition Temperatures of AFR700B Neat Resin after Hygrothermal Aging in Saturated Steam.

SECTION 2

MECHANICS OF POLYMER-MATRIX COMPOSITES

2.1 DIMENSIONAL STABILITY OF COMPOSITES AFTER MICRORACKING

Many space structures require not only high stiffness but precision alignment and dimensional stability as well, which makes the low CTE of carbon fiber composites attractive. Composite laminates can be tailored to obtain a near-zero CTE which is essential to maintaining the dimensional stability of composite structures in a space thermal environment. However, laminate CTE can change in service due to physical damage or material property changes associated with exposure to temperature fluctuations, outgassing, atomic oxygen, radiation, etc. Therefore, optimum selection and application of composites in space structures requires an understanding of how the service environment influences dimensional stability. For this study, we have selected to investigate the influence of a common form of physical damage, viz. microcracking in the off-axis plies, on changes in CTE (and hence dimensional stability) of composite laminates. A number of studies have been reported in this area [7-9], but the influence of microcracking on changes in laminate CTE is still not fully understood.

The main objective of this study, therefore, is to investigate the influence of transverse ply cracks on the variation in in-plane CTE composite laminates under mechanical loading and thermal cycling. A conventional aerospace graphite/epoxy, AS4/3501-6, was selected over candidate composite materials for space structures since it exhibits characteristics ideal for a generic study of this nature: it is well-characterized, exhibits consistent properties with little variation and is not cost-prohibitive. In this report, transverse ply cracks were introduced in tensile coupons of cross-ply laminates by axial loading in increments. After each incremental loading, the specimen's CTE was measured with strain gages and correlated with the measured crack density. These experimental correlations were compared with those from an analytical model. The details of this work can be found in reference [10].

2.1.1 Measurement of Composite CTE

Composite CTEs were measured using strain gages in conjunction with a computer-controlled temperature chamber and data acquisition system. Ultra-low-expansion titanium silicate (with a maximum thermal strain of 10 ppm over the temperature range of

interest) was used as the reference material. WK-series 350 Ω strain gages from Micro Measurements, Inc., with a gage length of 0.25 in., were employed. The strain gages were mounted with a high-temperature adhesive, cured as recommended by the manufacturer.

The measurement system employed can accommodate eight channels; one was used for temperature, one for time, and the remaining six for collecting thermal strains. A software program controlled the chamber temperature, allowing prescribed ramps to a series of temperatures, holds for a fixed period of time to allow the specimen temperature to equilibrate, and continuous acquisition of temperature and strain data. Data were collected during both heating and cooling cycles. A specimen was cycled between -150°F and 250°F at a rate of 5°F/min and held for 15 minutes at each increment of 40°F of temperature. Thermal strains recorded at the end of each holding period were utilized for determination of CTE. The resolution of strain and temperature measurement with this experimental setup is better than 1×10^{-6} and 1°F, respectively. The correction for transverse sensitivity of the strain gage was made from the information supplied by the manufacturer.

The accuracy and reliability of this measurement technique was verified with two materials of known CTE, aluminum (Al-2024-T4) and titanium (Ti-6Al-4V) alloys. The average measured CTEs for these materials are $12.73 \times 10^{-6}/^{\circ}\text{F}$ and $4.88 \times 10^{-6}/^{\circ}\text{F}$ for the aluminum and titanium alloys, respectively, which compare very well with the corresponding published handbook values of $12.9 \times 10^{-6}/^{\circ}\text{C}$ and $4.9 \times 10^{-6}/^{\circ}\text{F}$. The excellent reproducibility of the measurement technique was demonstrated by a variation of less than one percent in the CTE between consecutive measurements for four strain gages. The measured apparent thermal strain due to the mismatch in electrical properties of active gage and compensation gage over the test temperature range varies from near-zero to 50×10^{-6} which corresponds to a maximum apparent CTE of $0.125 \times 10^{-6}/^{\circ}\text{F}$.

To measure lamina longitudinal and transverse CTEs a rectangular coupon, 4" x 1", was sectioned from an [0]_{8T} composite panel, and one longitudinal and one transverse strain gage were mounted on each face. Thermal strains from all four gages were measured simultaneously in the temperature range of -150°F to 250°F. Because of the considerable scatter of the very low longitudinal CTE, a total of three specimens were tested in this manner for this property. Figures 18 and 19 show some of the typical strain data recorded, with the longitudinal thermal strain

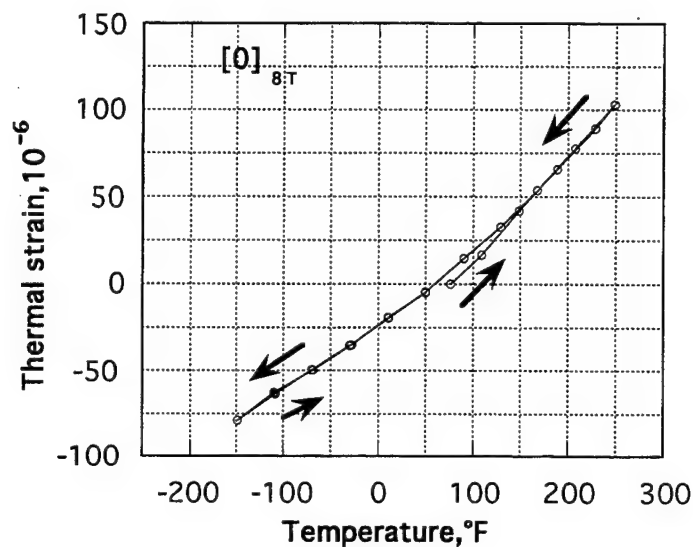


Figure 18. Thermal Strain of a $[0]_{8T}$ laminate through Heating and Cooling Cycles.

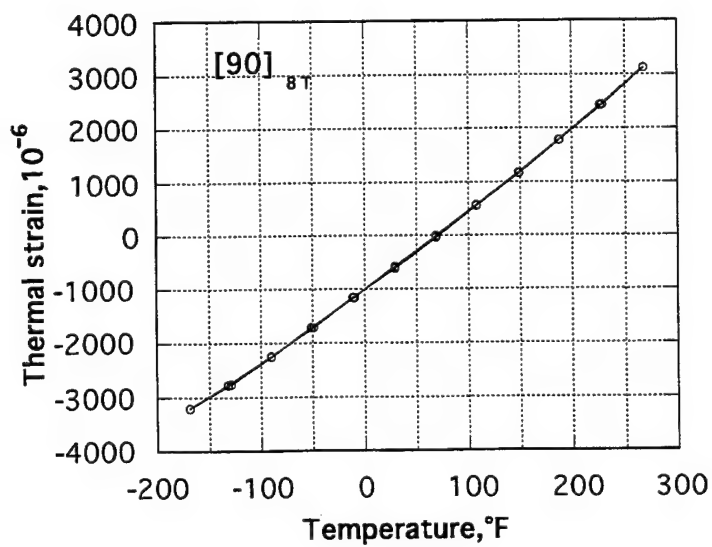


Figure 19. Thermal Strain of a $[90]_{8T}$ laminate through Heating and Cooling Cycles.

corrected for the transverse sensitivity of the strain gages. The CTE was obtained from a linear fit to the data over the entire test temperature range. The longitudinal CTE (of six specimens) ranged from 0.15 to $0.31 \times 10^{-6}/^{\circ}\text{F}$, with an average value of $0.22 \times 10^{-6}/^{\circ}\text{F}$, while the transverse CTE ranged from 13.99 to $14.71 \times 10^{-6}/^{\circ}\text{F}$, with an average value of $14.37 \times 10^{-6}/^{\circ}\text{F}$. The longitudinal CTE data have a wider scatter than the transverse data. The source of this scatter could be apparent strains from a mismatch in electrical properties of the two strain gages, and material variations within the laminate which arise from local variations in ply thickness, fiber alignment and fiber volume.

The CTEs of a $[0_2/90_2]_S$ laminate were determined from a 6" x 12" panel. Three locations on the panel were selected for CTE measurements, and back-to-back axial and transverse gages were mounted at each location. Figure 20 shows typical axial and transverse thermal strains as functions of temperature. Excellent reproducibility with this measurement technique is demonstrated from a comparison of data from two consecutive runs. The CTEs were determined from a linear fit to the data in Figure 20 over the test temperature range. The axial CTE (six measurements at three back-to-back locations) ranges from 1.39 to $1.59 \times 10^{-6}/^{\circ}\text{F}$, with an average value of $1.47 \times 10^{-6}/^{\circ}\text{F}$, while the transverse CTE ranges from 1.44 to $1.73 \times 10^{-6}/^{\circ}\text{F}$, with an average value of $1.59 \times 10^{-6}/^{\circ}\text{F}$. The corresponding coefficients of variation are 5.6 percent and 6.8 percent, respectively. The CTE predicted by the model used in this study is $1.464 \times 10^{-6}/^{\circ}\text{F}$, calculated from the average values of the longitudinal and transverse CTEs of the $[0]_{8T}$ composite. This is in excellent agreement with the value of $1.456 \times 10^{-6}/^{\circ}\text{F}$ obtained from laminated plate theory.

2.1.2 Influence of Microcracking on Laminate CTE

2.1.2.1 Analytical Background

The analytical model used in this study, developed by Schoeppner and Pagano [11], employs the variational theorem by Reissner [12] to predict the stress fields and energy release rates for cracked flat laminates containing orthotropic layers. The model can be used to examine the initiation, propagation and interaction of damage for thermoelastic problems in flat laminates under generalized plane strain conditions. A two-dimensional (2-D) representative volume element for uniform transverse crack spacing in a graphite-epoxy $[0_2/90_2]_S$

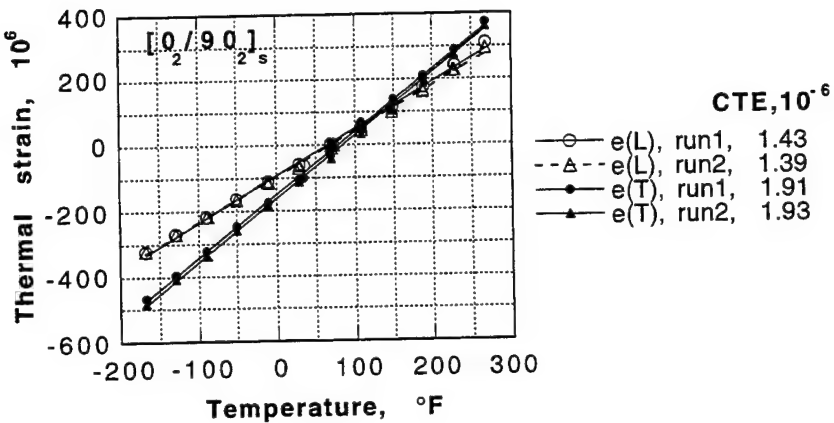


Figure 20. Variation in CTE of a $[0/90]_s$ Laminate in Two Normal Directions. (L: parallel to fiber in the surface ply; T: perpendicular to fiber in the surface ply).

laminate was used to model the change in the axial coefficient of thermal expansion (CTE) α_x as a function of crack density. Figure 21 illustrates the analytical model for the $[0/90]_s$ laminate. For the unit or periodic cell of length L , it is assumed that transverse cracks extend the full depth of the 90° layers in the cross-ply laminates and that the cracks are normal to the layer interface. It is assumed that lamina interfaces are perfectly bonded and that the traction free cracks are equally spaced. Furthermore, free edge effects are neglected in this 2-D model.

2.1.2.2 Experimental Results

Specimens 6" long and 1" wide were prepared from a $[0/90]_s$ panel such that the fibers in the surface layers were parallel to the specimen length. Specimen edges were ground and then polished to enhance their microscopic examination. An axial and a transverse strain gage were mounted on the specimen and the initial CTE in the axial direction measured prior to loading, as described earlier. Specimens were then loaded to a level at which transverse cracks initiated under the strain gage, as determined by monitoring acoustic emission during loading. The polished edges of the specimen were examined under a microscope to determine the nature of the transverse cracking and determine the crack density below the strain

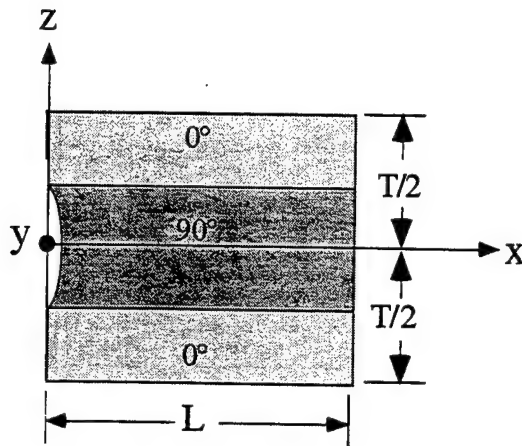


Figure 21. Cross-ply Transverse Crack Unit Cell.

gage. As defined by the analytical model, only transverse cracks which extended over the entire specimen width as well as the thickness of the 90-degree plies were counted. After the crack density was determined, the specimen was subjected to another increment of loading to obtain new cracks. Figure 22 shows a plot of thermal strain versus temperature for a representative specimen, for a range of crack densities. The applied stress, crack density and corresponding CTE are also shown in the figure. This incremental loading was repeated a number of times until the crack density reached saturation, i.e., when additional load produced no further increase in crack density. A total of four specimens were tested in this manner.

2.1.2.3 Comparison Between Prediction and Experiment

The variation in CTE as a function of crack density for a $[0_2/90_2]$ laminate is plotted in Figure 23. The lines in the plot are theoretical predictions obtained from unidirectional composite properties considering the scatter in the CTEs α_x and α_y ; the solid line represents the average value, and the two dashed lines represent the upper and lower bounds calculated from the largest and smallest values of the longitudinal CTE determined from $[0]_{8T}$ composites, as detailed earlier. The symbols in the plot are the experimental data from the four test specimens. The experimental CTE data tend to deviate from the analytical bounds in the region where the crack density reaches a limiting value, as seen in Figure 23. As the crack density approaches the limiting value, a number of partial cracks appear near the major transverse crack, as seen in Figure 24. These partial cracks were not included in the analysis.

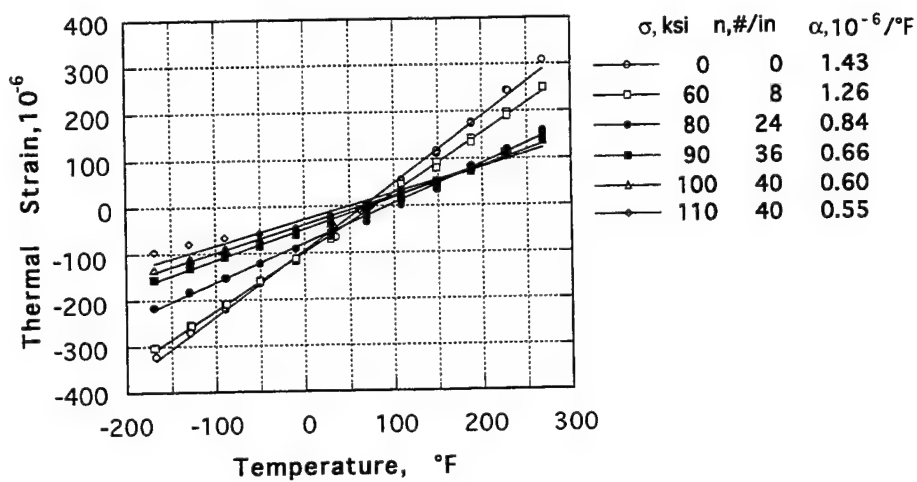


Figure 22. Thermal Strain as a Function of Temperature and Crack Density for a $[0/90]_s$ Laminate.

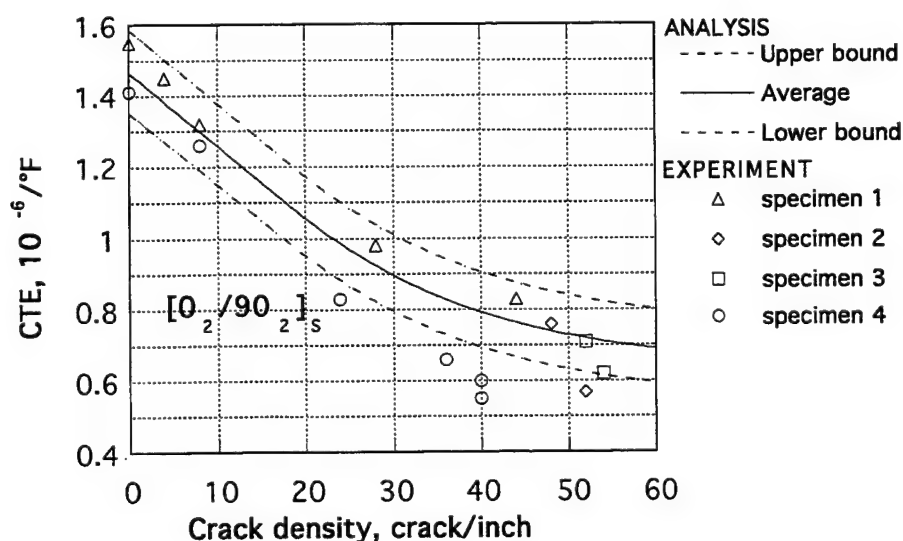


Figure 23. Comparison of Experimental and Predicted CTEs.

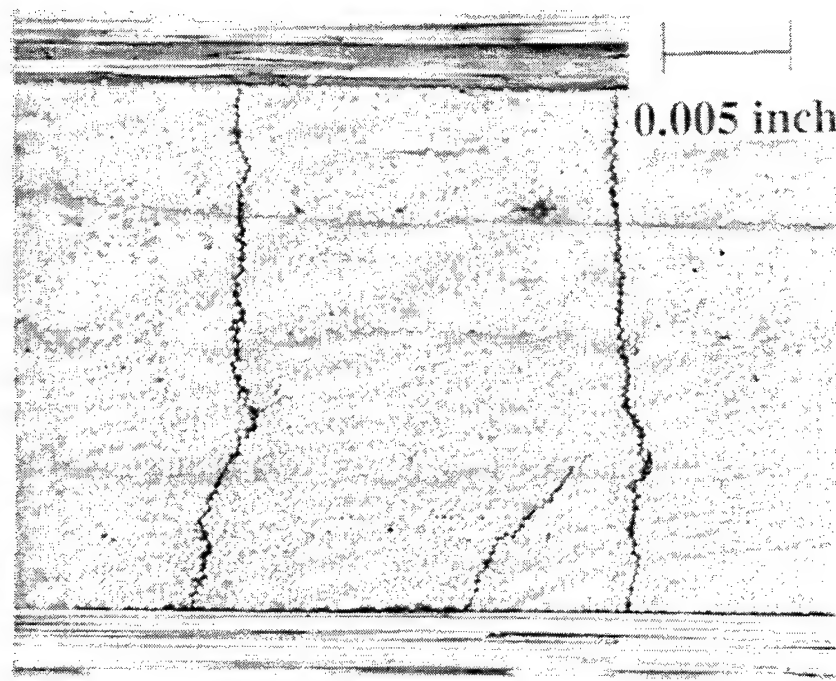


Figure 24. Micrograph Showing Transverse Cracks in a $[0_2/90_2]_s$ Laminate with Secondary Partial Cracks at/Near the State of Crack Saturation.

The variations in modulus and Poisson's ratio with crack density for a typical specimen are shown in Figure 25. A sharp drop in the values of both these properties at a crack density of 40 in^{-1} demonstrates the influence of the partial cracks on the observed correlations. In addition, further opening of the existing cracks may also contribute to the observed deviation between experiment and prediction. It should be noted that the large variation of Poisson's ratio with increasing crack density has not been considered in the analysis.

In summary, strain gages provide an inexpensive yet accurate means of measuring very low CTEs (and CTE changes) of composite laminates provided care is taken to minimize extraneous sources of error. The analytical model employed to predict this variation in CTE due to transverse cracking demonstrates great potential. The use of strain gages provides the flexibility to correlate localized damage with changes in composite CTE. This work is being extended to investigate variations in laminate CTE due to thermally induced microcracking.

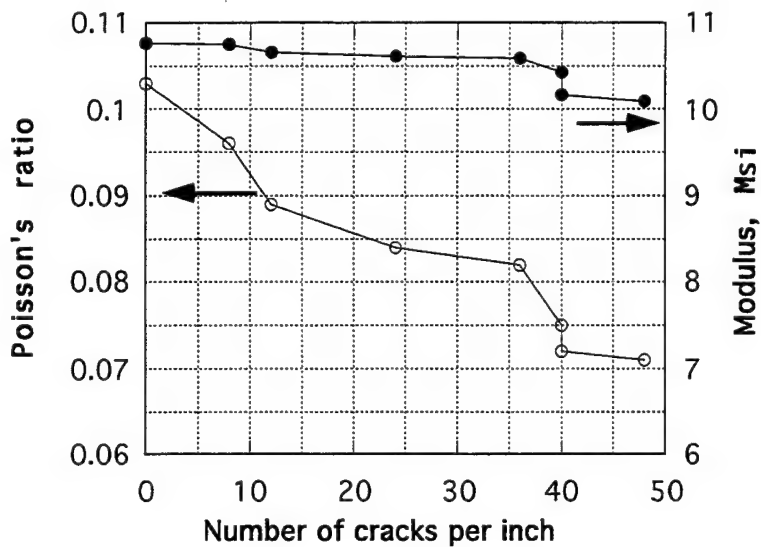


Figure 25. Variation of $[0/90]_s$ Laminate Elastic Properties with Crack Density.

2.2 TRANSVERSE CRACKING OF CROSS-PLY LAMINATES

Composites for space applications such as advanced satellites will require the use of new and/or improved materials so that more stringent dimensional stability requirements can be met. Transverse cracking often results in the loss of strength and stiffness, changes in the coefficient of thermal expansion and also provides pathways for moisture or other corrosive agents. Transverse matrix cracking in off-axis plies of composite laminates is believed to be the first visible form of damage, usually preceding delamination and fiber breakage. The origins of transverse matrix cracks are in the growth and coalescence of local damage in the form of fiber-matrix debonds and matrix microcracks and/or transverse fiber cracking and may be strongly influenced by localized variations in fiber spacing and fiber volume content.

In this work, an experimental study has been conducted on the initiation of ply-level damage under loading and processing stresses and imposed thermal loading to compare with results obtained from the analytical model [11]. The details of analytical model development and results can be found in reference [13].

2.2.1 Experimental Approach

The material system used in this study was IM7/5250-4 graphite/polyimide supplied in prepreg form. Unidirectional laminates and four different cross-ply laminates, [0/90/0]_s, [0/90₂/0]_s, [0/90₃/0]_s, and [0/90₄/0]_s were fabricated in an autoclave according to the manufacturer's recommend cure cycle. All panels were subjected to post cure at 227°C for 5 hours and 40 minutes in an oven.

All of the elastic properties were determined using ASTM D3039 and D3518 standard test except ν_{23} . This Poisson's ratio was determined from a [90₈] coupon under tension, in which axial strain and transverse strain in the z-direction were measured using small strain gages (0.81 mm long). The transverse gage was mounted on the free edge. Two axial strain gages, one on the flat surface and one on the free edge were mounted for comparison. Both strains are practically identical. The transverse ν_{23} was obtained from the transverse strain divided by the axial strain. G_{1c} for room temperature was determined using double cantilever beam according to the ASTM D5528. Thermal expansion coefficients α_x and α_y were measured using strain gages in conjunction with a computer-controlled temperature chamber and data acquisition system. The measured material properties for the analyses are

$$E_1=165.48 \text{ GPa}, \quad E_2=E_3=10.34 \text{ GPa}, \quad G_{12}=G_{13}=5.79 \text{ GPa}$$

$$G_{23}=3.31 \text{ GPa}, \quad \nu_{12}=\nu_{13}=0.31, \quad \nu_{23}=0.56$$

$$\alpha_1=0.45 \times 10^{-6}/^\circ\text{C}, \quad \alpha_2=\alpha_3=24.66 \times 10^{-6}/^\circ\text{C}, \quad G_{1c}=225 \text{ J/m}^2$$

Stress free temperature=180°C

Ply thickness=0.127 mm

A [0/90₄] unsymmetric laminate, which was curved due to residual stresses, was heated and observed to flatten at 180°C, which is the assumed stress free temperature.

2.2.2 Onset of Cracking under Mechanical Loading

Straight-sided coupon specimens were cut from the four panels, [0/90/0], [0/90₂/0], [0/90₃/0], and [0/90₄/0] using a diamond-impregnated saw. All specimens were 15.2 cm long and 2.5 cm wide and 2.5-cm fiberglass end-tabs were attached leaving 10.2 cm long gage section. The side edges were ground with sandpaper and then polished with 5 and 1 micron polishing powder in order to enhance the microscopic images. All specimens were

inspected under a microscope to examine fabrication or preparation induced damage prior to each test. No damage has been observed prior to testing.

The onset of the first ply failure was determined using an acoustic emission technique. An acoustic emission transducer was mounted on the flat surface of the specimen using vacuum grease and an elastic band. Specimens were loaded with monitoring axial and transverse strains, and were unloaded at the first indication of the first ply failure by the acoustic emission. Figures 26-29 show representative acoustic events indicating the first ply failure for each laminate. Both polished edges were subjected to microscopic examination to confirm the presence of the first ply failure and their nature. It was observed that there were 22 partial-width cracks in the [0/90/0] laminate whereas one full-width crack in the other three laminates. Figures 30-33 show micrographs indicating the first ply failure for each laminate. All transverse cracks extended to entire thickness of the 90-degree plies and some cracks in the [0/90₄/0] laminate deflected into the 0/90 interface as delamination. Nearly all transverse cracks in [0/90₃/0] and [0/90₄/0] observed on one edge of the specimen had a corresponding crack at the same lengthwise location on the other side of the specimen. This suggests that those cracks might extend to the full-width of the specimen. To delineate these cracks observed on the free edges, all specimens were subjected to x-ray radiograph with an aid of x-ray image enhancing penetrant. The x-ray radiographs indicated that none of the observed edge cracks extended the full-width of the specimen. To clarify the contradiction between corresponding edge cracks and the x-ray radiographs, four specimens, one of each laminate, were cut in halves lengthwise and polished to microscopically examine the internal transverse cracks. Cracks were also found in the interior of the specimen that aligned with the original free edge cracks for [0/90₂/0]_s, [0/90₃/0]_s, and [0/90₄/0]_s laminates. This confirms that all transverse cracks observed on the free edges in these three laminates extended to full-width of the specimen. No internal cracks were observed in the [0/90/0], indicating that the cracks observed on the edges were partial-width cracks. Table 5 shows the first transverse crack occurred in all specimens under uniaxial tensile loading. Figure 34 shows the comparison of experimental data with analytical predictions [13].

2.2.3 Onset of Cracking under Thermal Loading

The onset of the first ply failure was also investigated under thermal loading. A [0/90₄/0], which theoretically has the lowest first ply failure stress level of the four

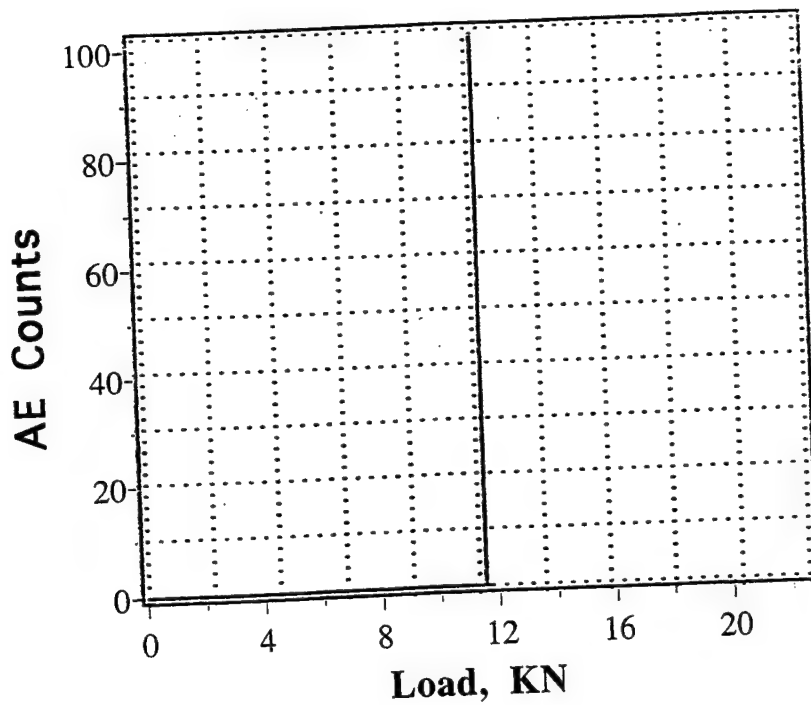


Figure 26. Acoustic Emission Showing Onset of Microcracking for [0/90/0] Laminate.

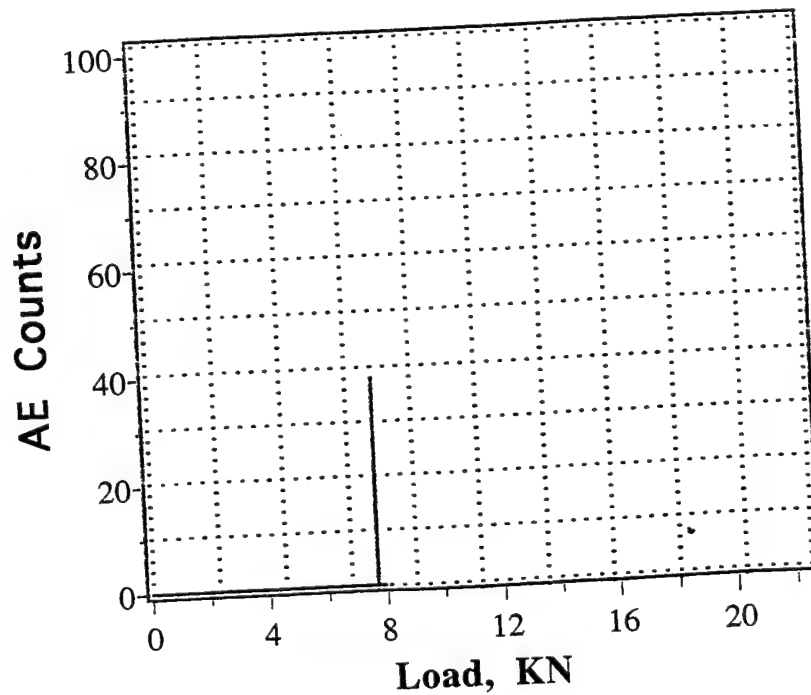


Figure 27. Acoustic Emission Showing Onset of Microcracking for [0/90₂/0] Laminate.

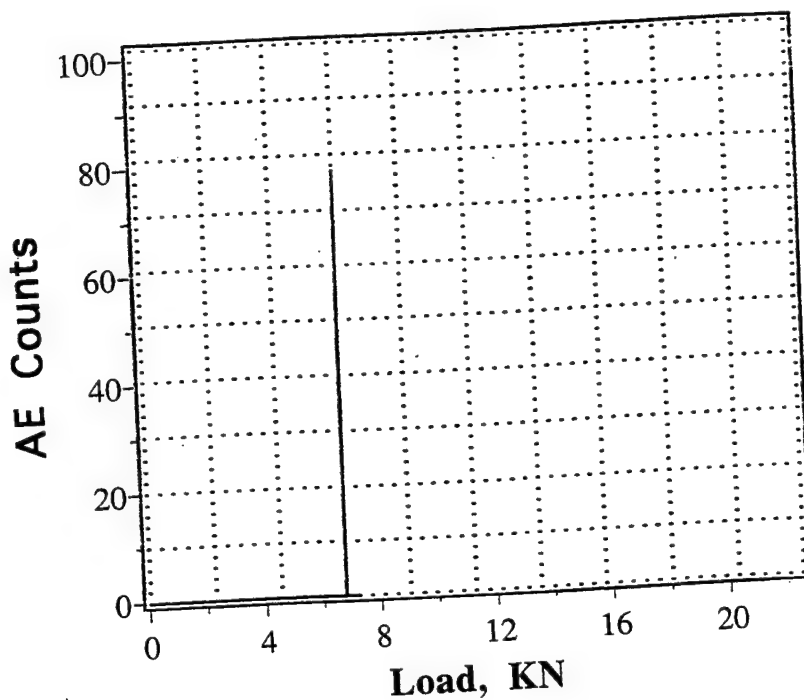


Figure 28. Acoustic Emission Showing Onset of Microcracking for [0/90₃/0] Laminate.

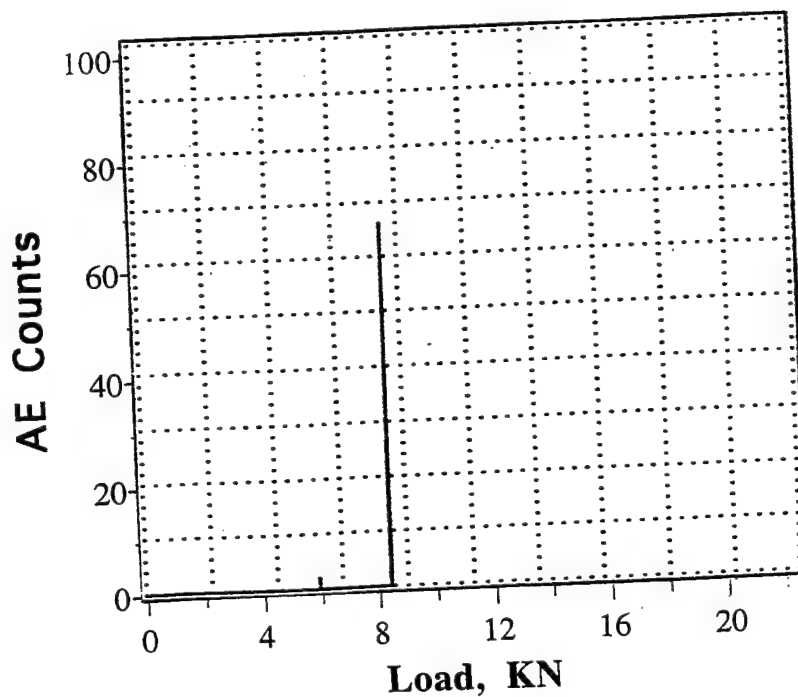


Figure 29. Acoustic Emission Showing Onset of Microcracking for [0/90₄/0] Laminate.

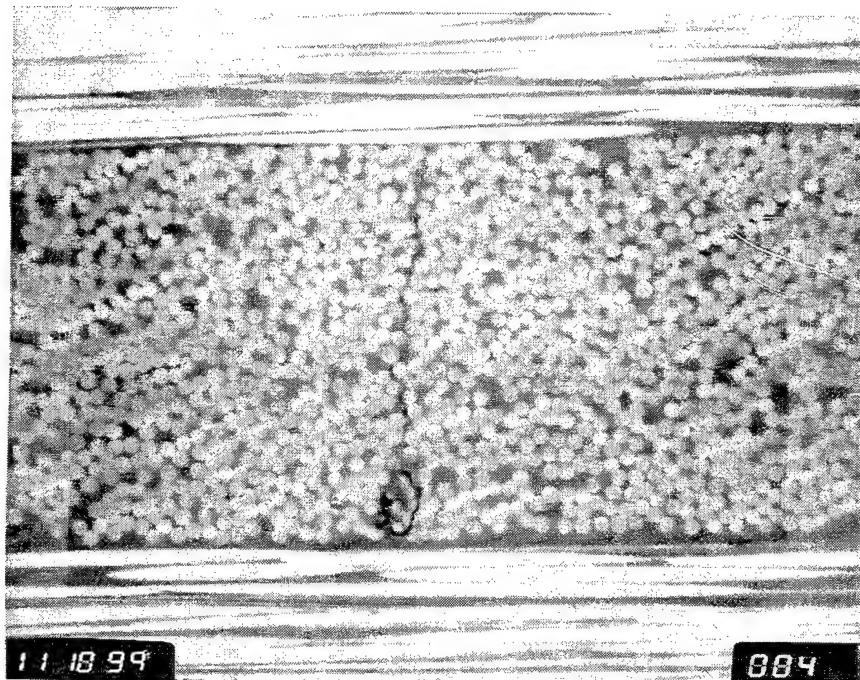


Figure 30. Micrograph Showing Onset of Transverse Crack for [0/90/0] Laminate.

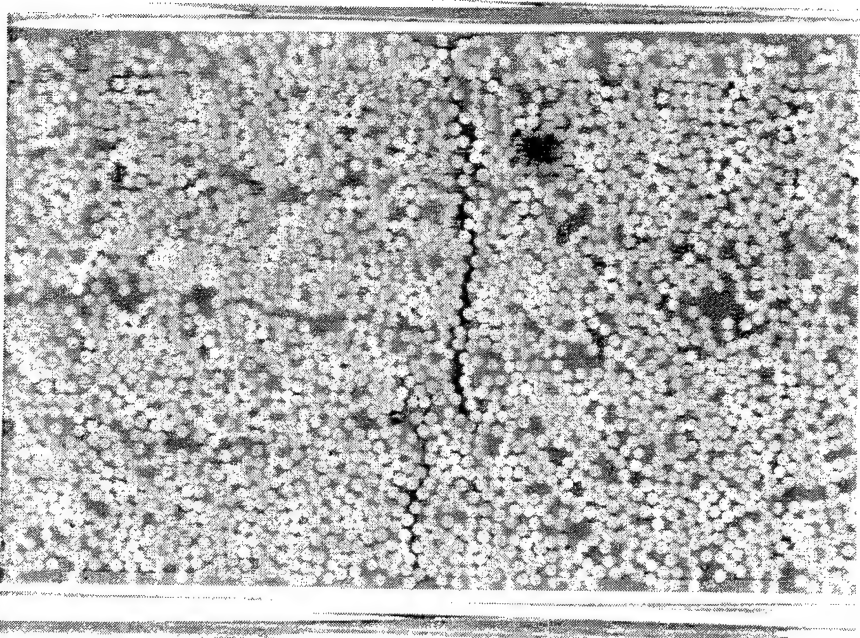


Figure 31. Micrograph Showing Onset of Transverse Crack for [0/90₂/0] Laminate.



Figure 32. Micrograph Showing Onset of Transverse Crack for [0/90₃/0] Laminate.

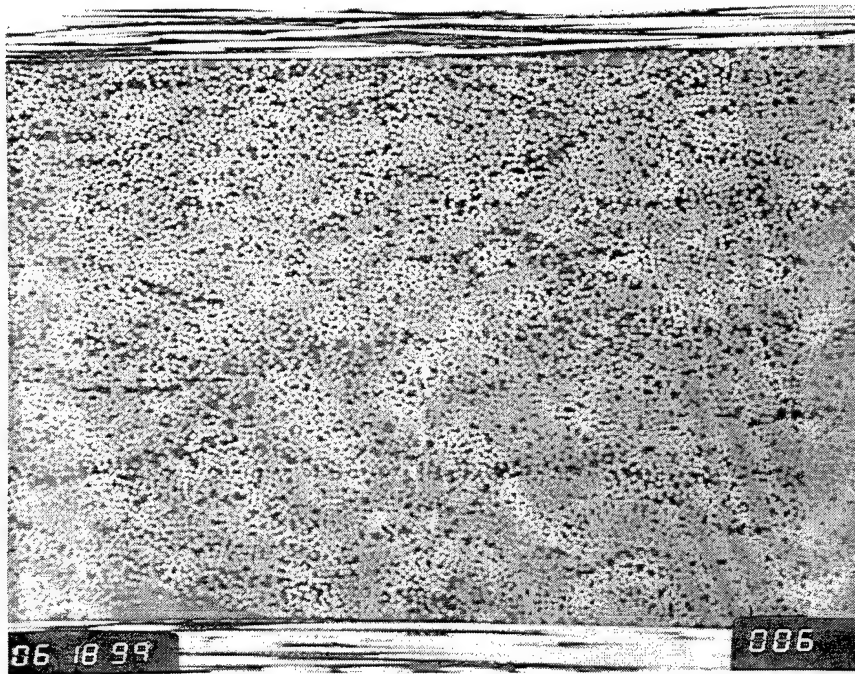


Figure 33. Micrograph Showing Onset of Transverse Crack for [0/90₄/0] Laminate.

TABLE 5
EXPERIMENTAL CRACKING LOADS

Laminate	Spec. ID	Load (MPa)	E* (GPa)	Partial Cracks	Full Cracks
[0/90/0]	P5/ 1-2	845.81	107.70	3	0
	P5/ 1-2	969.62	107.70	7	0
	P5/ 1-3	1049.97	108.04	22	0
	P5/ 1-6	852.27	108.52	4	0
	P5/ 1-7	928.61	108.80	8	0
[0/90 ₂ /0]	P5/ 2-2	574.48	88.81	1	0
	P5/ 2-3	574.98	87.98	1	0
	P5/ 2-6	568.96	83.70	1	0
	P5/ 2-7	611.42	84.60	0	2
[0/90 ₃ /0]	P5/ 3-2	441.98	73.91	0	1
	P5/ 3-3	437.49	73.84	0	1
	P5/ 3-6	405.48	67.22	0	1
	P5/ 3-7	453.71	68.40	0	1
[0/90 ₄ /0]	P5/ 4-2	294.74	64.05	1	0
	P5/ 4-2	334.40	64.05	0	2
	P5/ 4-3	350.35	62.60	0	1
	P5/ 4-6	466.21	62.19	0	1
	P5/ 4-7	420.72	61.50	0	1

E* = Initial Modulus

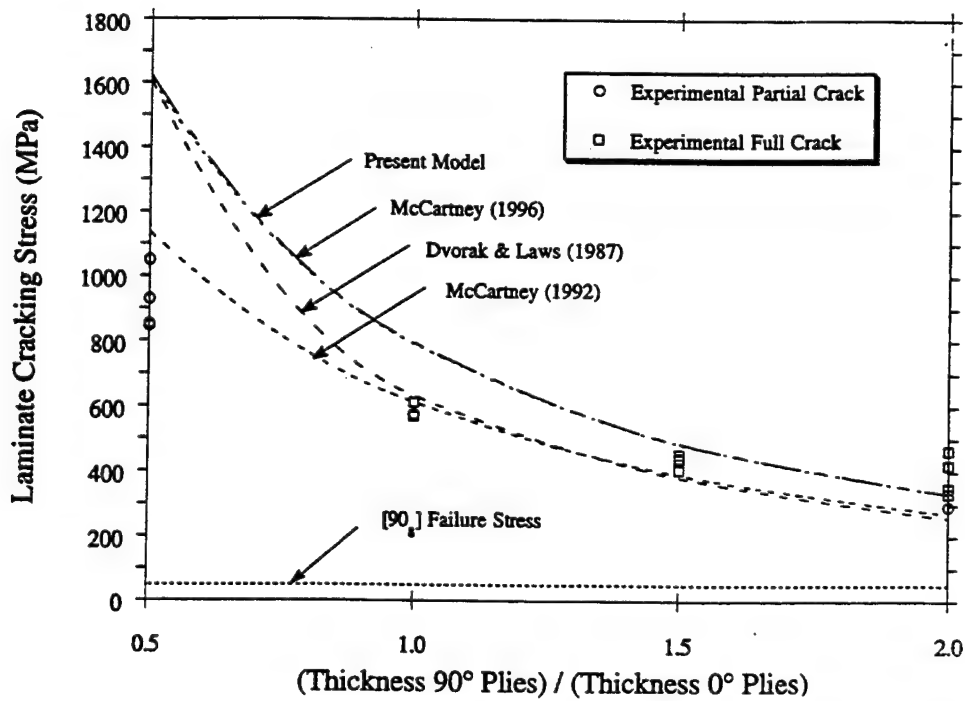


Figure 34. Steady State Cracking Prediction versus Experiment.

laminates, was tested. All free edges of the specimens were polished and subjected to pretest microscopic examination. No cracks were observed. Two tensile coupon specimens (15.2 x 2.5 cm) were subjected to a thermal loading of -118°C in an insulated chamber with a cooling rate of 5.5°C/minute. Specimens were held to 10 minutes at -118°C and removed from the chamber to inspect the transverse cracks. No cracks were found. To increase the magnitude of the thermal loading, two [0/90₄/0] 5.1 x 5.1 cm specimens were prepared and subjected to -196°C by submerging into a liquid nitrogen tank for 10 minutes. No transverse crack was found on any of the four free edges. Two 2 x 2-cm specimens were also prepared and subjected to -269°C by submerging into a liquid helium tank for 10 minutes. Microscopic examination, again, revealed no transverse cracks on any of the free edges. The analytical model [13] predicts the first transverse cracks at -229°C for this laminate as shown in Table 6.

TABLE 6
CRACKING TEMPERATURE PREDICTION

Laminate	Present Model
[0/90/0]	-601°C
[0/90 ₂ /0]	-380°C
[0/90 ₃ /0]	-284°C
[0/90 ₄ /0]	-229°C

In summary, the initiation and propagation of ply-level matrix cracks in graphite/bismaleimide cross-ply laminates subjected to thermo-mechanical loading has been examined. Evidence for steady state cracking has been shown for [0/90₃/0] and [0/90₄/0] laminates whereas the [0/90/0] and [0/90₂/0] laminates exhibited stable ply-level transverse cracking or partial edge cracks. Predictions of steady state crack growth for pure thermal loading and for mechanical loadings by various models compared with the experimental. Work continues on the study of the specimen width effect on the occurrence of steady state cracking in these laminates and to develop a technique to detect the initial micromechanical damage.

2.3 EXPERIMENTAL INVESTIGATION OF CRACK-FRONT PROFILE IN BONDED COMPOSITE MATERIALS

The use of adhesively bonded composite structures is expected to increase for two primary reasons. The first is the drive to reduce the assembly cost in composite structures by applying the concept of large, highly integrated bonded and co-cured structures. The second is the need to perform repairs on composite structures. These repairs often necessitate the use of bonded scarf joints. A primary concern regarding the use of adhesively bonded joints in primary load-bearing structures is the environmental durability of the bond. This study attempts to identify failure modes seen in adhesively bonded composite structures and environmental effects on bonded composite structures. The crack front profile is expected to provide information whether the free-edge effect has any significant effect on the crack propagation or not.

All the test data reported in this report, however, are for tests performed in room temperature and dry conditions (i.e., without aging the specimens in an environmental chamber). The specimen geometry selected was double-lap type to reduce the large amount of global bending observed in single-lap configurations. The adhesives included in the study were Cytec FM300-2U and FM300-2M, and the carbon/epoxy AS4/3501-6 composite was used as the adherent. In order to be consistent with the curing temperature of heat blanket field repair, the curing temperature of the adhesive was chosen to be 125°C (257°F).

2.3.1 Bonding Process Selection

A study for process selection was carried out to control and minimize the void content in the bond line. Unidirectional 16-ply (0.080-inch thick) AS4/3501-6 carbon/epoxy composite was used as the adherent. The adherents were prepared for bonding by hand sanding the bonding surface and then cleaned with acetone. Then, in order to minimize the ingress of moisture from the adherend (AS4/3501-6 composite) during curing of the adhesive bond, the adherend was vacuum dried overnight prior to bonding. The manufacturer's recommended cure cycle was first used to cure the bond which yielded a considerable amount (over the acceptable limit) of void content in the adhesive. In order to modify the cure cycle to minimize void content, parallel plate thermomechanical analysis (TMA) of the adhesive was performed. Figure 35 shows the adhesive viscosity and temperature profiles using the manufacturer's recommended cure cycle. For the manufacturer's recommended cycle, as revealed in Figure 35, there was a sharp viscosity increase of the adhesive within a very short time (less than 10 min.). Such short

time duration of viscosity increase was not sufficient to suppress the void formation even by applying 100 psi of external pressure. In order to slow down the rate of viscosity increase, a modified two-step cure cycle was adopted. The viscosity and temperature profiles of the adhesive using the modified cure cycle are shown in Figure 36. The modified cure cycle contains a temperature hold at 100°C for 25 min. to slow down the viscosity rise of the adhesive, and then the rest of the curing was done at the 125°C hold. An external pressure of 100 psi was applied at the beginning of the 100°C-temperature hold. The void content in the bond line using the modified cure cycle was less than two percent, quantified by optical microscopic inspection of polished edges of the bonded specimens. The modified cure cycle was thus selected and used to prepare all the double-lap shear specimens [14, 15].

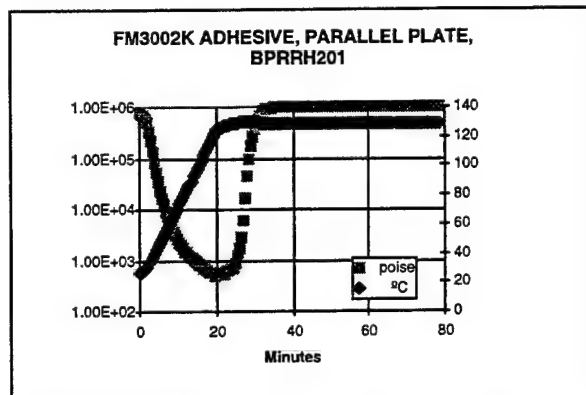


Figure 35. Parallel Plate TMA: Temperature and Viscosity Profiles of FM300-2K Adhesive Using the Manufacturer's Recommended Cure Cycle.

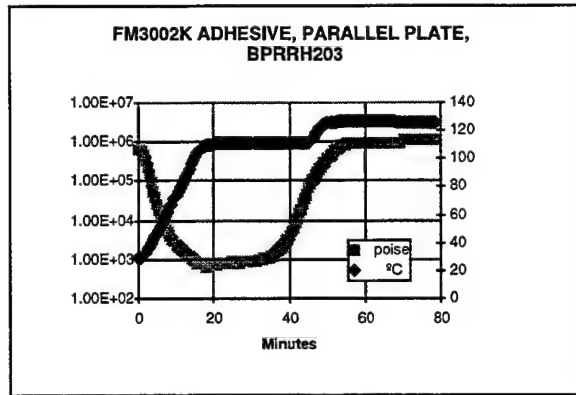


Figure 36. Parallel Plate TMA: Temperature and Viscosity Profiles of FM300-2K Adhesive Using the Modified Cure Cycle.

2.3.2 Test Procedure

Static tests were performed to monitor the initiation and growth of damage in unconditioned specimens. Very small strain gages (typically 0.032 and 0.015 inches in size), edge polishing coupled with optical microscopy, fluorescent microscopy, and acoustic emission sensors were used to monitor damage progression. The specimen configuration of the double lap-shear specimens and the representative locations where strain gages were installed to measure strains are shown in Figure 37. The adherends were made of 16-ply [0] unidirectional

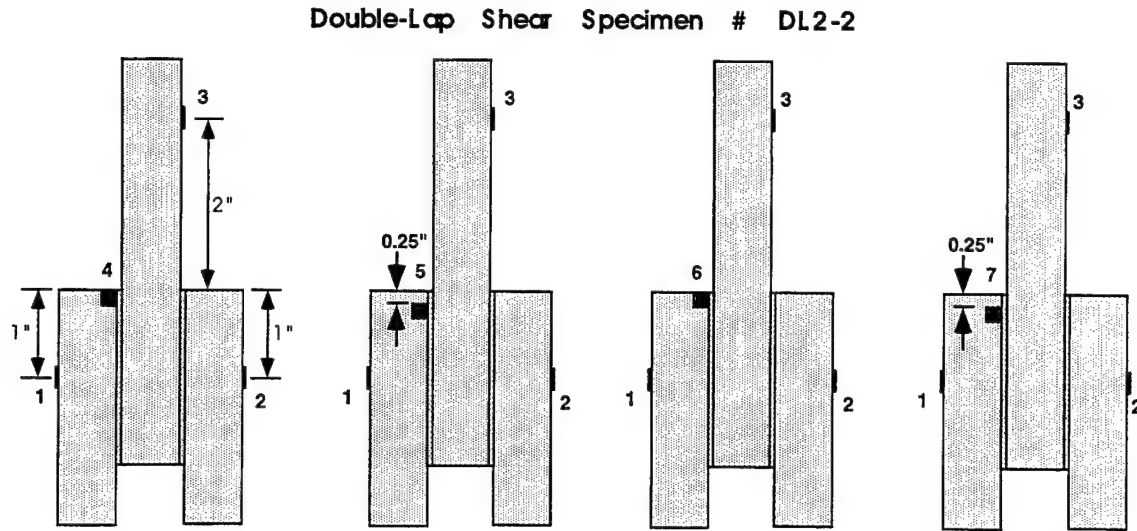


Figure 37. Specimen Configuration and Representative Strain Gage Locations of the Double Lap-Shear Specimen.

AS4/3501-6 graphite/epoxy composites of 0.09 inches (2.286 mm) in thickness. The average bond line thickness was 0.005 inches (0.127 mm). In order to validate the test procedure, the measured strains were correlated with the analytical predictions before any damage initiation. The analytical prediction indicated a sign reversal of the interlaminar normal strain (ε_3) between locations 4 and 5, and axial strain at location 7 being larger than that in location 6. The measured strains at these four locations, subjected to a tensile loading, are shown in Figure 38. The measured strains at these four locations are qualitatively in agreement with the analytical prediction. A qualitative agreement of the measured strains with that of the analytical prediction ensured validity of the test procedure. In addition, a quantitative correlation of the experimental data with the analytical prediction is being performed [16, 17].

2.3.3 Damage Observation

One of the objectives of this study is to understand damage development mechanism and identify the influence of the free-edge stresses on the bond line crack development. The specimens were loaded incrementally in tension, and at the end of each load

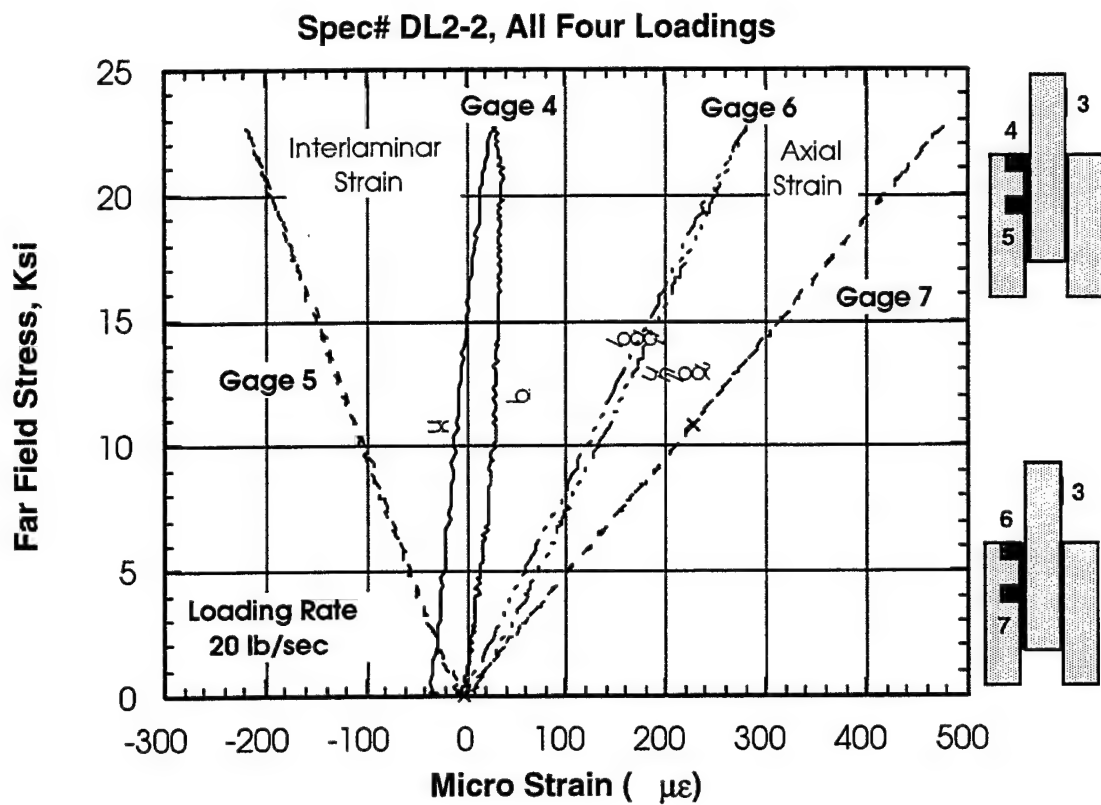


Figure 38. Measured Strains at Locations 4, 5, 6, and 7.

increment, the specimens were unloaded and the edge of the specimen containing the bond line was inspected with an optical microscope for damage. During loading, the specimens were instrumented with an acoustic emission sensor for monitoring damage initiation. In addition, strain gages at locations of strains sensitive to damage were also installed to monitor damage. Among many damage detection techniques, the fluorescent dye penetration technique appeared to be the most effective in detecting damage. Figure 39 shows the strain measured by Gage 5 (location of strain extremely sensitive to damage) in a specimen. As revealed from the strain plot in Figure 39, the second loading indicated an initiation of damage. The specimen was then unloaded and its edge was microscopically inspected for damage. The edge micrograph indicating the crack initiation is shown in Figure 40. The crack initiated at the middle adherent interface crack, and at the bond end where Gage 5 was installed (location of high interlaminar

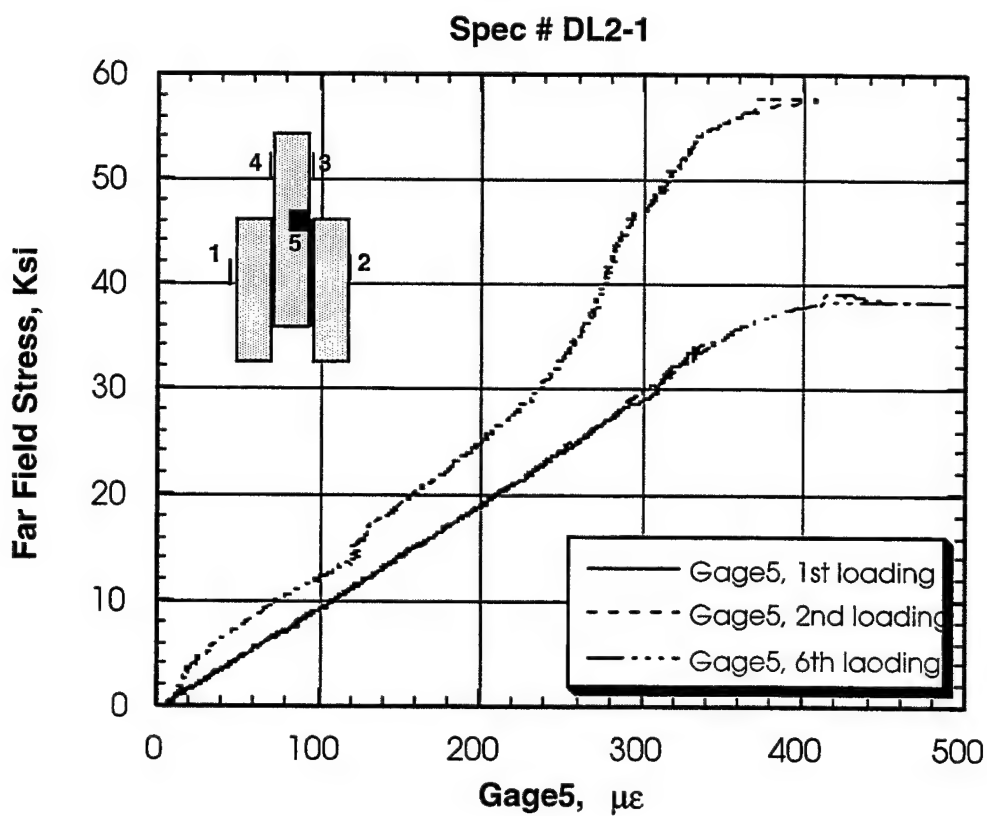


Figure 39. Interlaminar Normal Strains at a Damage Sensitive Location for Several Incremental Loading.

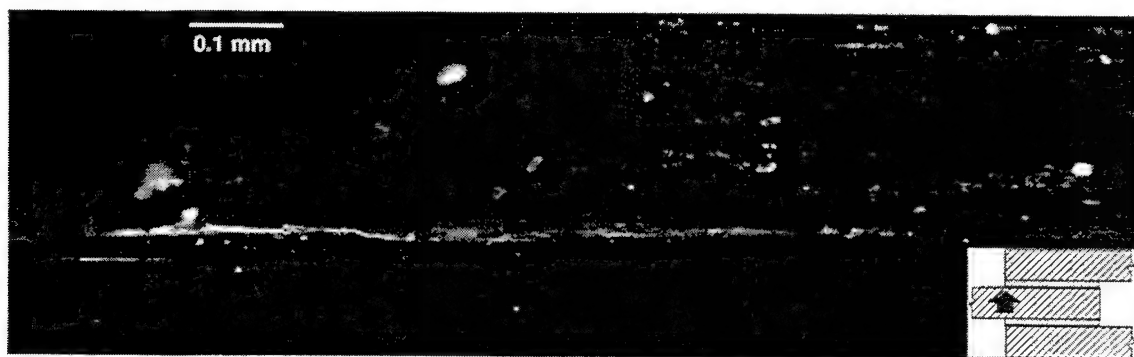


Figure 40. Micrograph (in Fluorescent Field) Indicating Crack Initiation at the Middle Adherend Interface.

normal and shear strains). The crack initiation took place at a stress level of 67 percent of that at final failure.

Besides crack initiation, tests were conducted to understand the crack propagation phenomenon. The specimens were loaded incrementally in tension beyond crack initiation, following the same procedure as was followed in the case of the crack initiation study. The interlaminar normal strain measured by Gage 4 installed (at a damage sensitive location) on a specimen used for damage propagation study is shown in Figure 41. At the peak load of the first loading, the strain gage, accompanied by the acoustic emission sensor, indicated damage development. The edge micrograph of the specimen showing crack developed at the middle adherend interface is shown in Figure 42. The observation of the crack along the bond line revealed that the crack moved from the middle adherent interface to the outer adherent interface at a distance of 19 mm from the crack initiation end of the bond, Figure 43. The micrographs shown in Figures 42 and 43 were taken at a loading of 90 percent of the failure load. The crack moving from one interface to the other was consistently observed in all specimens.

2.3.4 Crack Front Profile

The above crack observation on specimen edge provides crack propagation phenomenon on the bond edge. Due to the material property discontinuity between the adhesive and the adherent at the bond line, the free-edge stresses may influence the crack front near the specimen edges. In order to study the influence of the free-edge stresses on the crack front profile, specimens were loaded to 50 percent of the failure load which was sufficient to initiate damage (confirmed with signals from the acoustic emission sensor). Crack enhancing dye was applied at the cracked end of the specimen. The excess dye was carefully wiped off, and the specimen was unloaded and stored in a desiccator for two weeks to let the dye dry. Then the specimen was loaded to failure. The failure surface covered with the crack enhancing dye proves the crack front occurred at the previous load. The crack front in two representative specimens is shown in Figure 44. For all practical purposes, the crack front appears to be uniform from edge to the interior of the specimen width. Thus the effect of the free-edge stresses appear to be insignificant on the crack front profile. Consequently, the effect of the free-edge stresses may be ignored in analyzing the crack propagation in bonded joints of unidirectional composites.

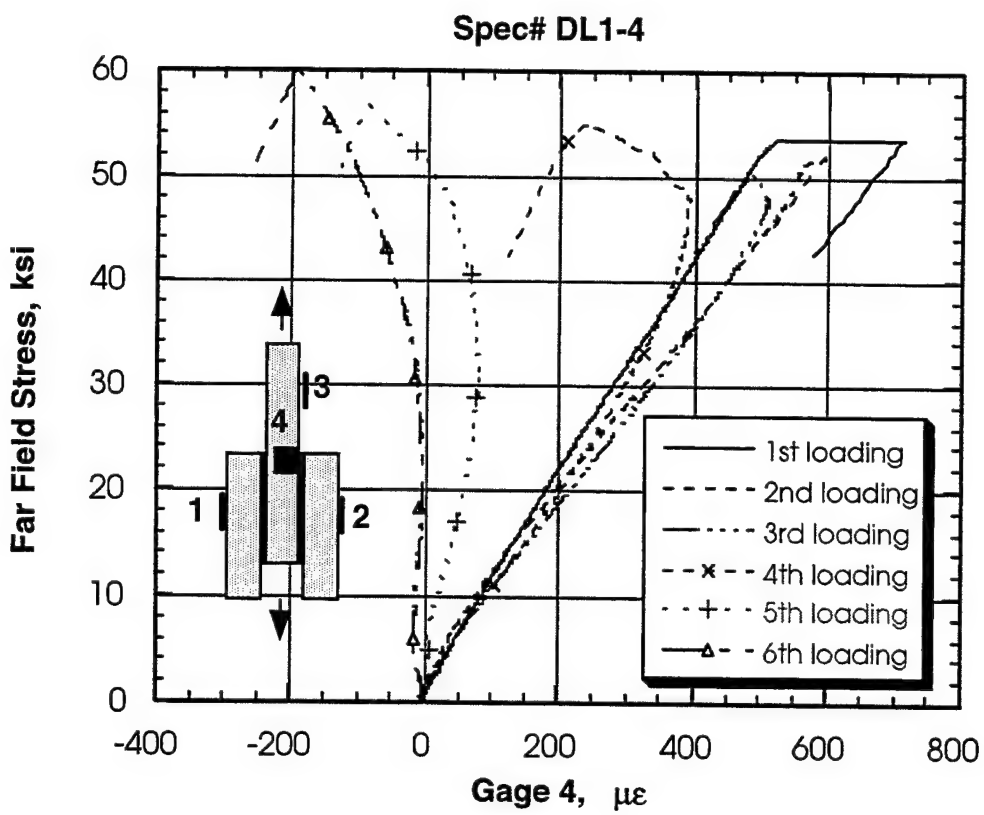


Figure 41. Interlaminar Normal Strains at a Damage Sensitive Location for Several Incremental Loadings Beyond Crack Initiation in the Bond.

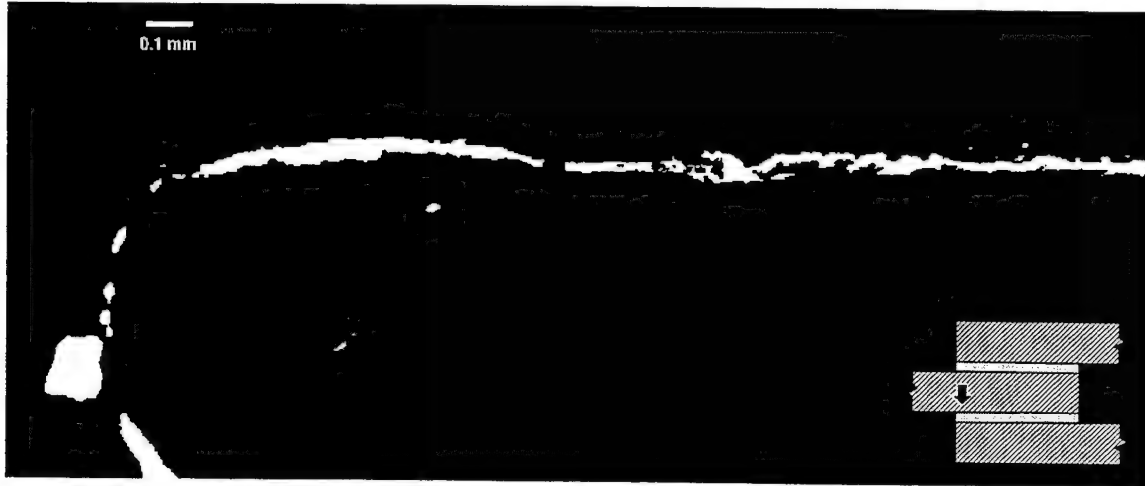


Figure 42. Edge Micrograph Showing Interface Crack at the Middle Adherend Interface Taken after a Load of 90 Percent of Failure.

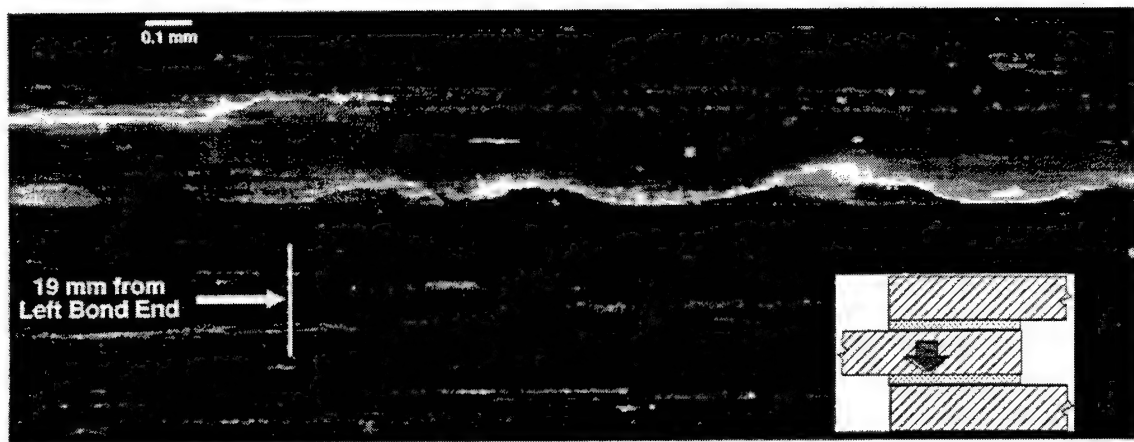


Figure 43. Edge Micrograph Showing Interface Crack Moving from One Adherend Interface to the Other. The micrograph was taken after a load of 90 percent of failure.

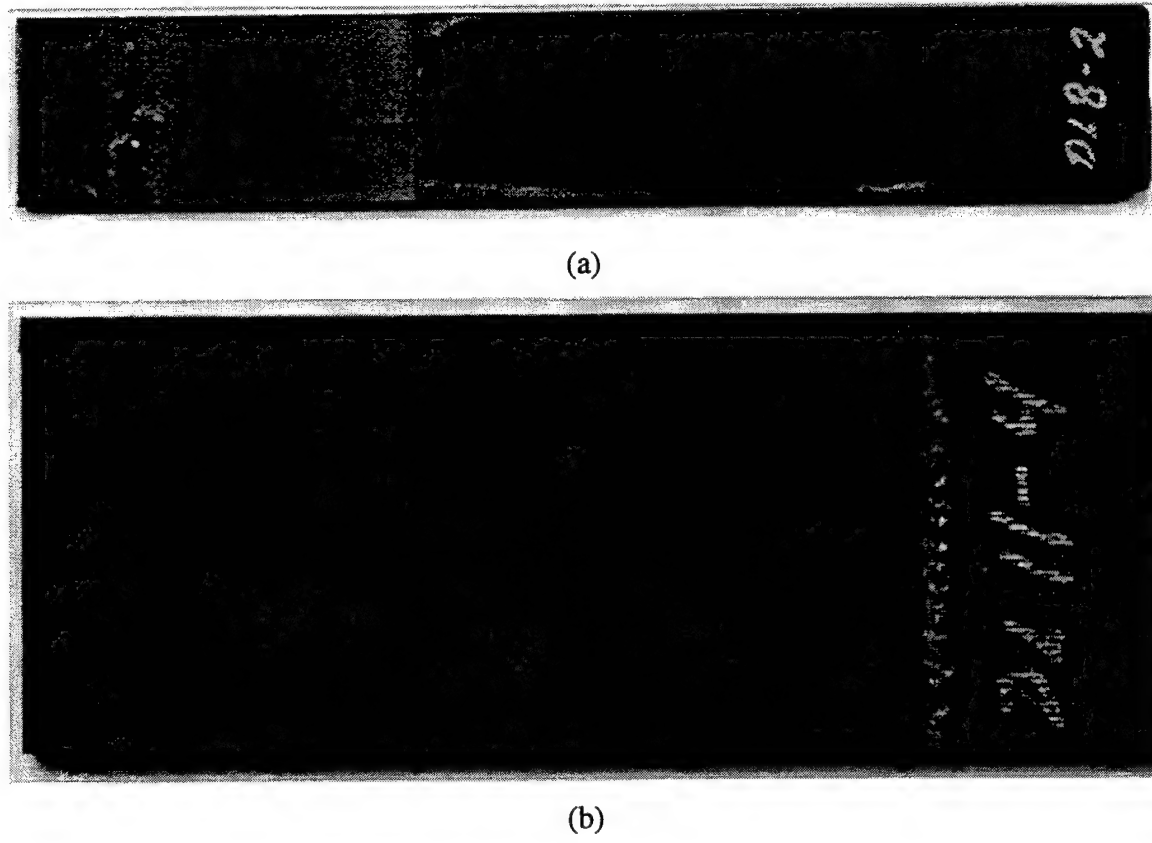


Figure 44. Crack Front Profile in Two Representative Specimens.

In summary, damage evolution in bonded joints of unidirectionally reinforced composites is studied. The crack development process observed at the specimen edge reveals that the crack propagate along an interface then traverses to the other interface. The study of the crack front profile indicates that the influence of the free-edge stresses on crack propagation is practically insignificant for bonded unidirectionally reinforced composites. Stress analysis of the crack development process is needed to study the failure mechanism.

2.4 THREE-DIMENSIONAL MIXED VARIATIONAL MICROMECHANICS MODEL FOR TEXTILE COMPOSITES

The fiber preforms used in composites manufacturing, instead of the traditional unidirectional preps, have been proven to provide low-cost composite parts. Moreover, complex geometry or contoured parts, which are difficult to make from unidirectional composites, can conveniently be made with fiber preforms. The two-dimensional woven fabric (textile) of fiber tows is known to be one of the most widely used fiber preforms in producing structural composite parts. To achieve the optimum structural properties of these parts, there is an urgent need to develop a basic understanding of deformation/damage mechanics and failure mechanisms of textile composites.

The failure in textile composites in general occurs in the vicinity of two perpendicular yarn crimping over and under to each other, Figure 45. In the vicinity of the yarn crimping, the stress is three-dimensional. To optimize the material properties and improve the performance of textile composites, we need to understand the physics and identify the stress components influencing the failure mechanism. Experimental observation [18] of damage initiation in textile composites reveals that the damage initiates in the form of interface cracks in the vicinity of yarn crimping, which is strongly influenced by the interlaminar stresses at the interface region. Thus, an accurate prediction of the interlaminar stresses at the interface region is needed to reliably analyze damage and failure in woven composites. Most of the research work in this area, however, is based on two-dimensional stress analysis which does not reliably predict the interlaminar stresses. Further, traditional finite-element analysis only predicts stresses accurate at the Gaussian integration points; thus, even three-dimensional finite element analysis does not yield accurate interlaminar stresses at the interface.

In order to obtain reliable interlaminar stresses at the yarn interface, a three-dimensional analytical model is developed based on the Reissner variational principle. An accurate

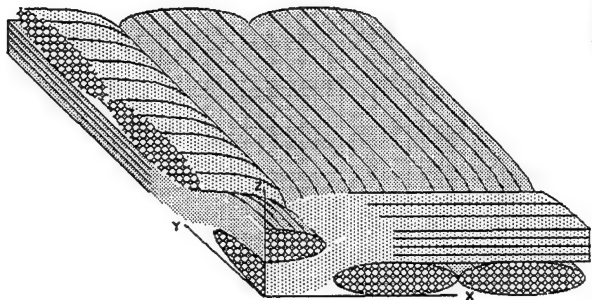


Figure 45. RVE of a 2D Textile Composite.

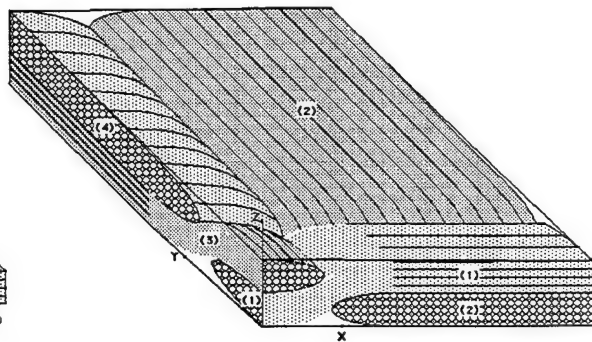


Figure 45(b) RVE of the Model.

prediction of the interlaminar stresses at the yarn interface is obtained by satisfying the interface traction continuity conditions and the equilibrium of stresses pointwise. The representative volume element (RVE) of the model is divided into several subregions; each subregion is occupied by a characteristic fabric yarn. The in-plane stresses within a yarn are assumed to vary linearly in the thickness direction, and the expressions for the interlaminar stresses are obtained by satisfying the three-dimensional equilibrium equations. After performing the thickness integration, the model yields a set of partial differential and algebraic equations which is solved by using cubic splines. The analytical derivation of the governing equations of the model is described below.

The governing equations of elasticity, in terms of the Cartesian coordinates, (x, y, z), can be obtained from the following variational equation, developed by Reissner [12]

$$\delta J = 0 \quad (1)$$

where

$$J = \int_V F dV - \int_{S'} \tilde{\tau}_i u_i dS \quad (2)$$

and

$$F = \frac{1}{2} \sigma_{ij} (u_{i,j} + u_{j,i}) - W \quad (3)$$

In these equations, W is the strain energy density expressed in terms of the stresses σ_{ij} ; V is the volume; S the entire surface; $\tilde{\tau}_i$ the prescribed tractions; u_i the displacement components; and S' is the portion of the boundary on which one or more traction components are prescribed.

It is understood that both stresses and displacements are subjected to variation in the application of Equation (1), and summation over the range of repeated subscripts (but not superscripts) is implied throughout the work.

As described above, each yarn is modeled as homogeneous and transversely isotropic. The cross sectional boundary of the yarn is confined by h_1 (lower boundary) and h_2 (upper boundary). Because of yarn waviness and elliptical cross-sectional boundary of the yarns, h_1 and h_2 are functions of both x and y .

The expressions of the stress components are as follows:

$$\sigma_i = p_{ik} f_k^{(i)} \quad (i = 1 - 6, K = 1 - 4) \quad (4)$$

where p_{ik} are functions of x and y , and $f_k^{(i)}$ are functions of z only. The functions $f_k^{(i)}$ associated with the in-plane stresses, as discussed above, are linear functions of z , and $f_k^{(i)}$ associated with the interlaminar stresses are derived by satisfying the linear elasticity equations of equilibrium. Equation (4) is substituted in Equation (2), and the integration with respect to z is performed. Because of the dependence of the subregion surface boundaries (h_1 and h_2) on x and y , Leibnitz's theorem in the following form must be applied on terms involving derivatives in x and y .

$$\int_{h_1(x,y)}^{h_2(x,y)} \frac{\partial}{\partial \xi} G(x, y, z) dz = \frac{d}{d\xi} \int_{h_1(x,y)}^{h_2(x,y)} G(x, y, z) dz - \frac{\partial h_2}{\partial \xi} G(x, y, h_2) + \frac{\partial h_1}{\partial \xi} G(x, y, h_1) \quad (5)$$

where ξ represents either x or y , and G is a general function of x , y , and z .

After performing the integration of Equation (2) with respect to the thickness (z), using Equation (5) where appropriate, and imposing the interface traction continuity conditions on the first variation of Equation (2), we obtain the following governing equations representing the equilibrium, compatibility, and boundary conditions for the RVE to determine the 23^*N unknown variables.

(a) Equilibrium equations, for $k=1, 2, \dots, N$: (7^*N equations)

$$F_1^{(k)} = (h_2^{(k)} - h_1^{(k)}) \left(\frac{\partial p_{11}^{(k)}}{\partial x} + \frac{\partial p_{61}^{(k)}}{\partial y} \right) + (p_{11}^{(k)} - p_{12}^{(k)}) \frac{\partial h_1^{(k)}}{\partial x} + (p_{61}^{(k)} - p_{62}^{(k)}) \frac{\partial h_1^{(k)}}{\partial y} - p_{51}^{(k)} + p_{52}^{(k)} - p_{53}^{(k)} = 0 \quad (6.1)$$

$$F_2^{(k)} = (h_2^{(k)} - h_1^{(k)}) \left(\frac{\partial p_{12}^{(k)}}{\partial x} + \frac{\partial p_{62}^{(k)}}{\partial y} \right) + (p_{11}^{(k)} - p_{12}^{(k)}) \frac{\partial h_2^{(k)}}{\partial x} + (p_{61}^{(k)} - p_{62}^{(k)}) \frac{\partial h_2^{(k)}}{\partial y} - p_{51}^{(k)} + p_{52}^{(k)} + p_{53}^{(k)} = 0 \quad (6.2)$$

$$\dots \\ F_7^{(k)} = (h_2^{(k)} - h_1^{(k)}) \left(\frac{\partial p_{53}^{(k)}}{\partial x} + \frac{\partial p_{43}^{(k)}}{\partial y} \right) - 2p_{53}^{(k)} \left(\frac{\partial h_2^{(k)}}{\partial x} - \frac{\partial h_1^{(k)}}{\partial x} \right) - 2p_{43}^{(k)} \left(\frac{\partial h_2^{(k)}}{\partial y} - \frac{\partial h_1^{(k)}}{\partial y} \right) + 6p_{34}^{(k)} = 0 \quad (6.7)$$

(b) Subregion compatibility equations, for k=1, 2, ..., N: (4*N equations),

$$\chi_{33}^{(k)} = \chi_{34}^{(k)} = \chi_{43}^{(k)} = \chi_{53}^{(k)} = 0 \quad (7)$$

where

$$\chi_{ij}^{(k)} = \eta_{ij}^{(k)} - E_{ij}^{(k)} - \hat{S}_{iklj}^{(k)} p_{kl}^{(k)}; \quad \hat{S}_{iklj}^{(k)} = \iint S_{ij}^{(k)} f_k^{(k)} f_l^{(k)} dx dy \quad (8)$$

(c) Interface compatibility equations, for k=1, 2, ..., N-1: (12*N-12 equations),

Consider a perfectly bonded interface between k-th and l-th subregions (yarns). Here l-th yarn is considered on top of the k-th yarn (i.e., l-th yarn is at a higher z-value than that of the k-th yarn).

$$\chi_{i1}^{(l)} + \chi_{i2}^{(k)} = 0 \quad \text{for } i = 1, 2, \dots, 6 \quad (9)$$

$$\chi_{12}^{(k)} + \frac{\partial h_k}{\partial x} \chi_{52}^{(k)} + \left(\frac{\partial h_k}{\partial x} \right)^2 \chi_{32}^{(k)} = 0 \quad (10)$$

$$\chi_{22}^{(k)} + \frac{\partial h_k}{\partial y} \chi_{42}^{(k)} + \left(\frac{\partial h_k}{\partial y} \right)^2 \chi_{32}^{(k)} = 0 \quad (11)$$

$$\chi_{62}^{(k)} + \frac{\partial h_k}{\partial x} \chi_{42}^{(k)} + \frac{\partial h_k}{\partial y} \chi_{52}^{(k)} + 2 \frac{\partial h_k}{\partial x} \frac{\partial h_k}{\partial y} \chi_{32}^{(k)} = 0 \quad (12)$$

$$p_{52}^{(l)} - \frac{\partial h_l}{\partial x} p_{12}^{(l)} - \frac{\partial h_l}{\partial y} p_{62}^{(l)} - p_{51}^{(k)} + \frac{\partial h_l}{\partial x} p_{11}^{(k)} + \frac{\partial h_l}{\partial y} p_{61}^{(k)} = 0 \quad (13)$$

$$p_{42}^{(l)} - \frac{\partial h_l}{\partial x} p_{62}^{(l)} - \frac{\partial h_l}{\partial y} p_{22}^{(l)} - p_{41}^{(k)} + \frac{\partial h_l}{\partial x} p_{61}^{(k)} + \frac{\partial h_l}{\partial y} p_{21}^{(k)} = 0 \quad (14)$$

$$p_{32}^{(l)} - \frac{\partial h_l}{\partial x} p_{52}^{(l)} - \frac{\partial h_l}{\partial y} p_{42}^{(l)} - p_{31}^{(k)} + \frac{\partial h_l}{\partial x} p_{51}^{(k)} + \frac{\partial h_l}{\partial y} p_{41}^{(k)} = 0 \quad (15)$$

(d) Boundary conditions (12 equations)

1. Top surface of the RVE (6 equations)

$$\chi_{12}^{(n)} + \frac{\partial h_2^{(n)}}{\partial x} \chi_{52}^{(n)} + \left(\frac{\partial h_2^{(n)}}{\partial x} \right)^2 \chi_{32}^{(n)} = 0 \quad (16)$$

$$\chi_{22}^{(n)} + \frac{\partial h_2^{(n)}}{\partial y} \chi_{42}^{(n)} + \left(\frac{\partial h_2^{(n)}}{\partial y} \right)^2 \chi_{32}^{(n)} = 0 \quad (17)$$

$$\chi_{62}^{(n)} + \frac{\partial h_2^{(n)}}{\partial x} \chi_{42}^{(n)} + \frac{\partial h_2^{(n)}}{\partial y} \chi_{52}^{(n)} + 2 \frac{\partial h_2^{(n)}}{\partial x} \frac{\partial h_2^{(n)}}{\partial y} \chi_{32}^{(n)} = 0 \quad (18)$$

$$\chi_{52}^{(n)} + \frac{\partial h_2^{(n)}}{\partial x} \chi_{32}^{(n)} + \tilde{u}_2^{(n)} = 0 \quad (19.1)$$

or

$$\cos \alpha_n \cos \beta_n p_{52}^{(n)} - \sin \alpha_n \cos \beta_n p_{12}^{(n)} - \cos \alpha_n \sin \beta_n p_{62}^{(n)} = \tilde{\tau}_{x2}^{(n)} \quad (19.2)$$

$$\chi_{42}^{(n)} + \frac{\partial h_2^{(n)}}{\partial y} \chi_{32}^{(n)} + \tilde{v}_2^{(n)} = 0 \quad (20.1)$$

or

$$\cos \alpha_n \cos \beta_n p_{42}^{(n)} - \sin \alpha_n \cos \beta_n p_{62}^{(n)} - \cos \alpha_n \sin \beta_n p_{22}^{(n)} = \tilde{\tau}_{y2}^{(n)} \quad (20.2)$$

$$\chi_{32}^{(n)} + \tilde{w}_2^{(n)} = 0 \quad (21.1)$$

or

$$\cos \alpha_n \cos \beta_n p_{32}^{(n)} - \sin \alpha_n \cos \beta_n p_{52}^{(n)} - \cos \alpha_n \sin \beta_n p_{42}^{(n)} = \tilde{\tau}_{z2}^{(n)} \quad (21.2)$$

2. Bottom surface of the RVE (6 equations)

$$\chi_{11}^{(m)} + \frac{\partial h_1^{(m)}}{\partial x} \chi_{51}^{(m)} + \left(\frac{\partial h_1^{(m)}}{\partial x} \right)^2 \chi_{31}^{(m)} = 0 \quad (22)$$

$$\chi_{21}^{(m)} + \frac{\partial h_1^{(m)}}{\partial y} \chi_{41}^{(m)} + \left(\frac{\partial h_1^{(m)}}{\partial y} \right)^2 \chi_{31}^{(m)} = 0 \quad (23)$$

$$\chi_{61}^{(m)} + \frac{\partial h_1^{(m)}}{\partial x} \chi_{41}^{(m)} + \frac{\partial h_1^{(m)}}{\partial y} \chi_{51}^{(m)} + 2 \frac{\partial h_1^{(m)}}{\partial x} \frac{\partial h_1^{(m)}}{\partial y} \chi_{31}^{(m)} = 0 \quad (24)$$

$$\chi_{51}^{(m)} + \frac{\partial h_1^{(m)}}{\partial x} \chi_{31}^{(m)} - \tilde{u}_1^{(m)} = 0 \quad (25.1)$$

or

$$\cos \alpha_m \cos \beta_m p_{51}^{(m)} - \sin \alpha_m \cos \beta_m p_{11}^{(m)} - \cos \alpha_m \sin \beta_m p_{61}^{(m)} = \tilde{\tau}_{x1}^{(m)} \quad (25.2)$$

$$\chi_{41}^{(m)} + \frac{\partial h_1^{(m)}}{\partial y} \chi_{31}^{(m)} - \tilde{v}_1^{(m)} = 0 \quad (26.1)$$

or

$$\cos \alpha_m \cos \beta_m s_{41}^{(m)} - \sin \alpha_m \cos \beta_m s_{61}^{(m)} - \cos \alpha_m \sin \beta_m s_{21}^{(m)} = \tilde{\tau}_{y1}^{(m)} \quad (26.2)$$

$$\chi_{31}^{(m)} - \tilde{w}_1^{(m)} = 0 \quad (27.1)$$

or

$$\cos \alpha_m \cos \beta_m s_{31}^{(m)} - \sin \alpha_m \cos \beta_m s_{51}^{(m)} - \cos \alpha_m \sin \beta_m s_{41}^{(m)} = \tilde{\tau}_{z1}^{(m)} \quad (27.2)$$

The subscripts or superscripts m and n are associated with the bottom and top surfaces of the RVE, respectively. α and β are the angles of the slope of the subregion surface along the x and y directions, respectively. There are 23 unknown variables for each subregion (yarn) in the model. For an N number of subregions, Equations (6-27) yield a set of 23*N equations to determine the variables required to obtain the complete three-dimensional stress and strain fields. The above equations are solved by using cubic splines using the Rayleigh-Ritz approximation technique. The three-dimensional stress field of the RVE of the woven composites will be presented.

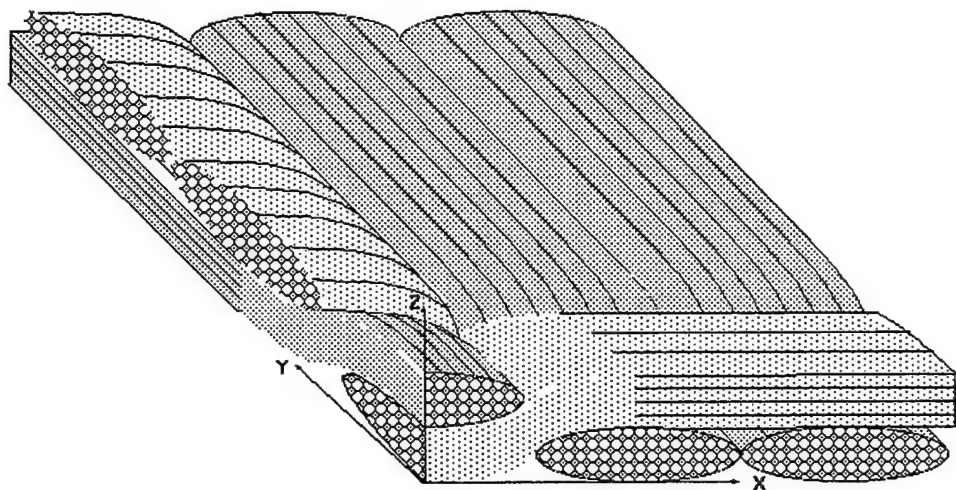
2.5 COMPARISON OF *IN SITU* DAMAGE ASSESSMENT IN UNBALANCED FABRIC COMPOSITE AND MODEL LAMINATE OF PLANAR (ONE-DIRECTIONAL) CRIMPING

In order to develop a basic understanding of damage and failure mechanisms in fabric (woven) composites, a comparative study of *in situ* damage development in two composite systems was performed. The two composite systems, an unbalanced (6:1) five-harness satin (5HS) fabric composite and a model laminate with planar (one-directional) fiber crimping, were tested in tension. The *in situ* damage observation was made by using a portable load frame placed on an optical microscope stage. The damage in the unbalanced fabric initiated in the form of yarn interface cracks, then developed further as intra-yarn delamination before failure. In the case of the model laminate, the damage first appeared as cracks in transverse laminae, then further developed as lamina interface cracks. The fiber breakage that was observed in the wavy region of the model laminate appeared to be limited to the free-edge region of the specimens. The stress analysis of the two composite systems needs to be performed to understand the damage development modes. The damage in the model laminate is expected to serve as a basis for understanding the damage development mechanism in woven composites.

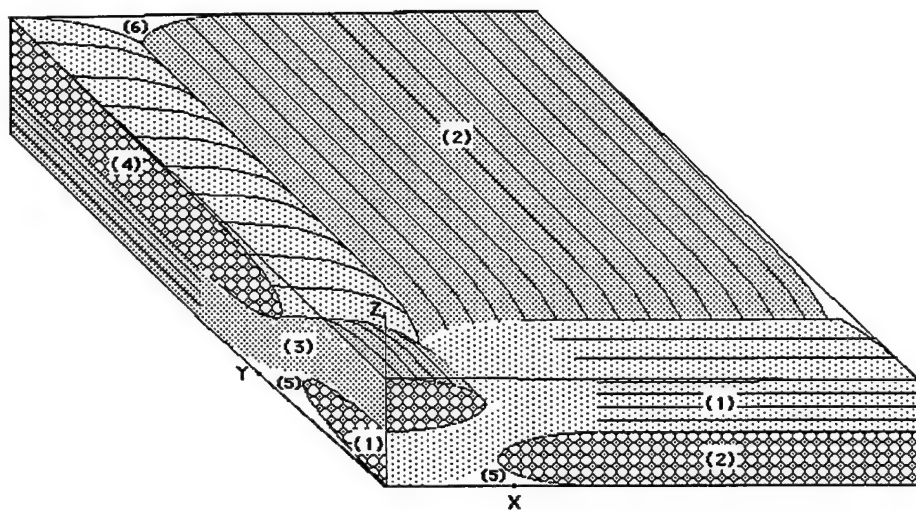
2.5.1 Introduction

The stiffness of fabric (woven) composites is well studied. However, the failure mechanism of this class of composites is not well understood. The prediction of the stiffness of woven composites is relatively simple compared to the prediction of strength, and has been done extensively in the literature, such as Zhang [19], Naik [20], Hahn [21], Yurgartis [22], Marrey [23], etc., to cite a few. Chou and Ko [24] provided a broad overview of this class of composites. However, the effect of yarn nesting and the failure mechanisms of woven composites are not well investigated, although some work has been done in this area. Naik [25], Karayaka [26], and others reported studies of the yarn nesting effects on the failure behavior of woven composites based on two-dimensional stress analysis. In the vicinity of yarn crimping of two-dimensional fabric (woven) architecture, two perpendicular yarns crimp over and under to each other. Due to the perpendicular yarn crimping, even under the application of simple unidirectional load, the stresses in the vicinity of the yarn crimping are three-dimensional (Whitcomb [27]), Figure 46. Hence, two-dimensional stress analysis is not expected to offer a basic understanding of the failure mechanism of this material. A three-dimensional stress analysis complimented with appropriate experimental observation identifying the stress components causing the failure is necessary to develop a basic understanding of failure mechanism of woven composites. In this study, an experimental effort is carried out towards identifying the stress components causing failure in woven composites.

Due to the presence of two perpendicular yarns crimping at the failure location, there exists a difficulty in identifying experimentally the influence of the stress components on the failure of two-dimensional woven composites, as observed by Roy [18, 28]. Thus, a model composite is fabricated to simulate the fabric yarn crimping only in one direction (in a plane), Figure 47. In the vicinity of the planar yarn crimping, the stress field is two-dimensional (except for edge effects). Thus, the model composite, to some extent, simplifies the process of understanding the influence of the stress components on the failure of the composite in the vicinity of the yarn crimping. For the convenience of defining the waviness in the model laminates, the ratio of the yarn (or lamina in this case) waviness amplitude, α , to the length of the wave, λ , is defined as the lamina waviness ratio. In addition to the damage observation in the model laminate, an unbalanced (6:1) commercial woven composite, which is extensively used in space structures, was also tested in tension. Since the fiber reinforcement in the warp direction



(a)



(b)

Figure 46. (a) Schematic of the Weaving Pattern of a Fabric Composite, (b) A Realistic Representation of an RVE of a Fabric Composite where Adjacent Yarns of the Same Weave Patterns Are Squashed Together to Represent a Subregion of the RVE. The RVE has six subregions.

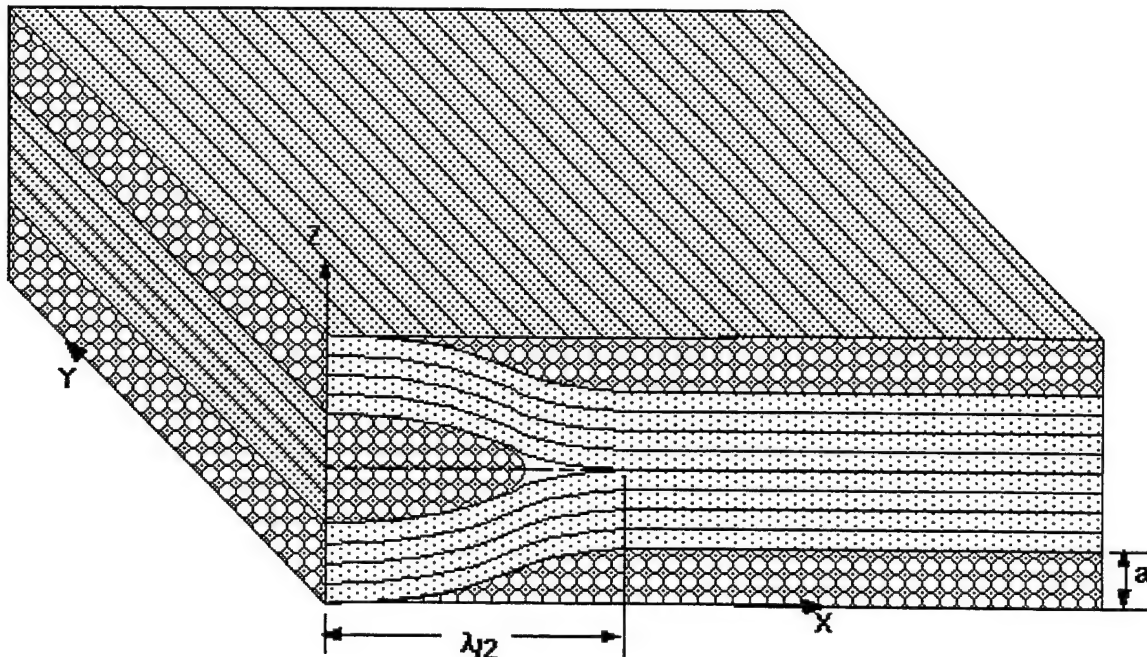


Figure 47. Schematic Representation of the Model Laminate.

of the (6:1) unbalanced composite is approximately six times that in the fill direction, the influence of the fill crimping on the damage development in the warp direction is expected to be small. Thus the model system, besides the effects due to the weaving architecture, should closely represent the mechanical response of the unbalanced composite. The objective of this work is to compare the damage evolution process in these two systems with a view of using the data towards understanding the failure mechanism in realistic woven composites.

2.5.1.1 Unbalanced (6:1) Woven Composite Laminate

The damage initiation in woven composites usually occurs in the form of yarn-interface cracks in the vicinity of yarn crimping [18]. Due to weaving of the yarns, identification of a particular lamina interface in a laminate especially containing a large number of woven laminae is somewhat difficult. Thus, for the ease of identifying the lamina interface a two-lamina thick warp-aligned laminate, $[0]_{2T}$, was fabricated for this study. The 5HS weave architecture of the woven lamina was reinforced with 3K and 1K of T300 graphite fiber tows, embedded in Epon 938 epoxy, in the warp and fill directions, respectively. The weave contained 1.18 and 0.59 tows per mm (30 and 15 per inch), in the warp and fill directions respectively, to provide the (6:1) unbalanced reinforcement. The unit cell size of the composite was 4.23 mm in

the warp direction and 8.47 mm in the fill direction. Thus, in order to cover more than a unit cell of the composite, strain gages of 12.7 mm in length were used to measure to reliably determine the stiffness of the composite. The cross-sectional micrographs of the unbalanced composite along the warp and fill directions are shown in Figure 48. The warp and fill yarn waviness ratios of the composite were 0.032 and 0.076, respectively.

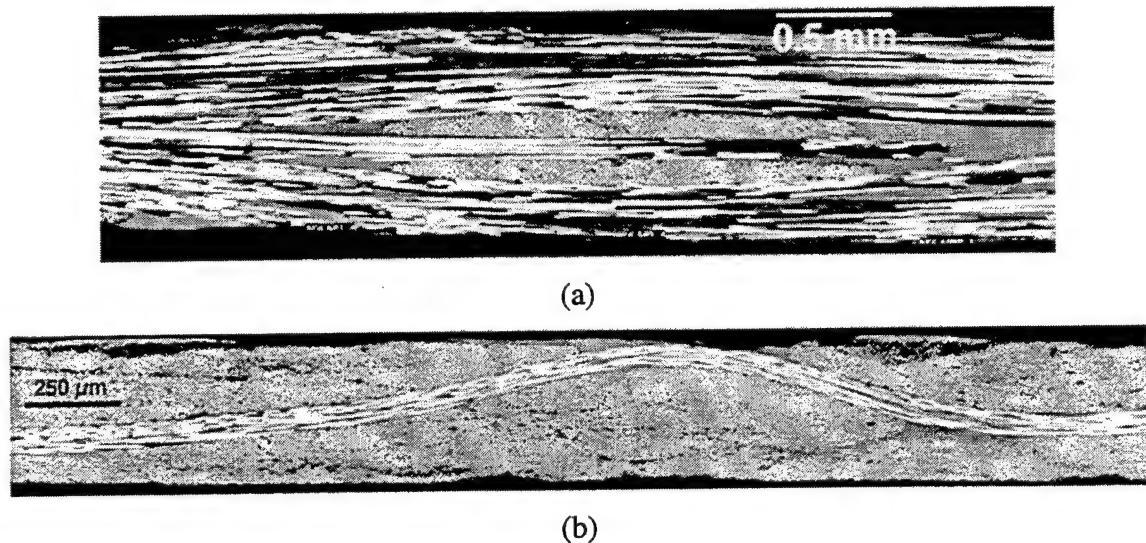


Figure 48. Cross-sectional Micrograph of the Unbalanced (6:1) Fabric (Woven) Laminate before Loading. (a) Along the warp direction, (b) Along the fill direction.

2.5.1.2 Model Laminate

The yarn crimping in woven (fabric) composites, as discussed before, occurs in two perpendicular directions as shown in Figure 46, while the model system with simulated planar (one-directional) crimping is illustrated in Figure 47. The laminates were made from AS4/3501-6 graphite/epoxy unidirectional prepgs. The waviness in the composite laminates was produced by inserting strips of unidirectional plies perpendicular to the longitudinal direction of the laminates. The lamina waviness ratios were varied by selecting different lay-up sequences of cross-ply laminates and different strip widths. However, the model laminate of lamina waviness of 0.027, which was close to that of the woven composite laminate in the warp direction, was used in this study. The cross-sectional micrograph of the model laminate used in this study, before testing, is shown in Figure 49. The geometrical configuration

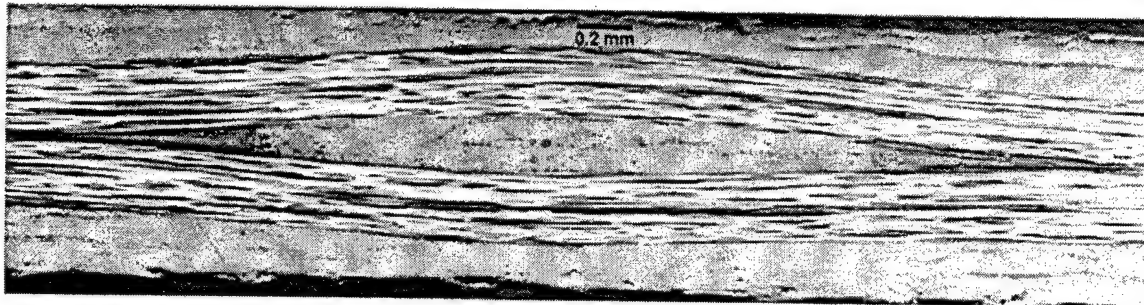


Figure 49. Cross-sectional Micrograph of the Model Laminate.

of the model laminates was characterized by the lamination sequence away from the wavy region, lamination sequence at the mid-section of the wavy region, and the lamina (yarn) waviness ratio. Consequently, a new laminate notation was used for the model laminates to indicate these characteristics. For example, the notation used for the model laminate shown in Figure 49 was $([90_2/0_2]_S, [90/0_2/90]_S, 0.027)$, indicating the lamination sequence away from the wavy region, mid-section lamination sequence of the wavy region, and the lamina waviness ratio, respectively. The differences between the model laminate and the woven composite was that the model laminate only contained lamina waviness in the longitudinal direction (with no waviness in the transverse or fill direction) and no weaving architecture (intertwining of yarns) was present in the model laminate. The model laminate was, thus, used to provide a guideline to distinguish the effect of the weaving architecture (a 3D effect) from the directional lamina crimping.

2.5.2 Experimental Procedure

The objective of the present work, as stated before, was to generate experimental data on damage development in the two composites stated above, which will later be correlated with stress analysis for assessing damage and developing failure criteria for woven composites. Among the available damage detection techniques, e.g., acetate film replication, fluorescent dye resin impregnation, etc., the *in situ* microscopic observation of damage under load was found to be more promising than any other damage detection techniques. The specimens were tested in tension. To observe and record the *in situ* damage development through a microscope, a portable load frame was used for this study, Roy [28]. The far-field strain and the strain near the wavy region of the model laminate were measured with 1.57 mm (0.062 in) strain gage installed at 12.7 mm (0.5 in) and 0.38 mm (0.015 in) strain gage installed at 2.0 mm (0.078 in) away from

the middle of the wavy region, respectively. The strain on the 5HS woven composite specimen was measured by a 12.7 mm (0.5 in) strain gage installed at the mid-gage length. The specimen configuration used for this study is shown in Figure 50. The stress-strain curves of the two composites (the model laminate and that of the woven composite), which were used as guidelines to correlate specimen strains with the damage development, were obtained by testing the specimens with an MTS servo-hydraulic test frame. The representative stress-strain curves of the two systems are shown in Figures 51 and 52.

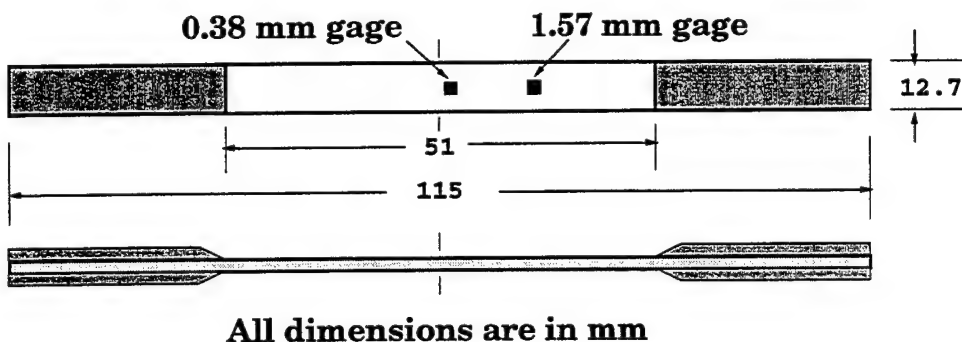


Figure 50. Specimen Configuration of the Model Laminate Showing Location of the Strain Gages. The specimen configuration of the woven composite was the same with strain gage installed at the middle of the gage section.

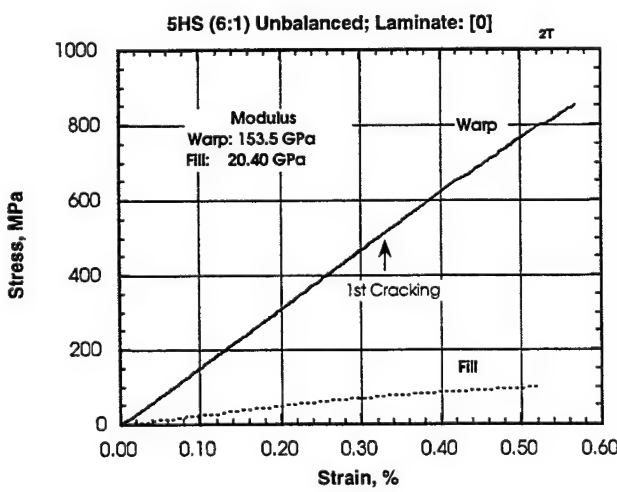


Figure 51. Stress-Strain Curves of the Specimens Prepared in the Warp and Fill Directions of the Unbalanced 5HS (6:1) Woven Composite Laminate Subjected to Tensile Loading.

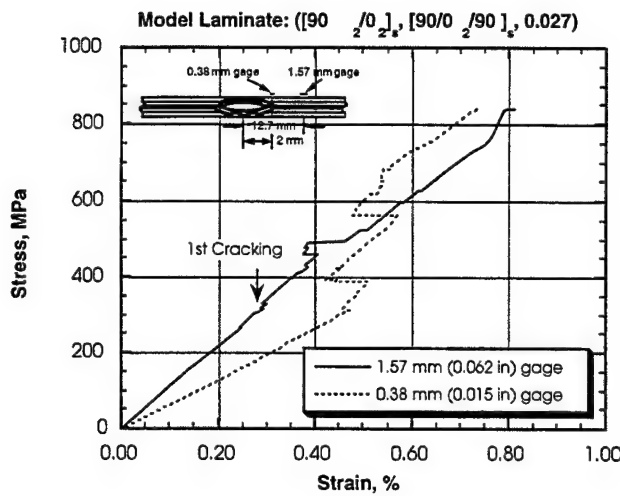


Figure 52. Stress-Strain Curves of the Model Laminate Subjected to Tensile Loading.

2.5.3 *In Situ* Damage Observation

The specimens were loaded in tension in the portable load frame placed on a microscope stage. The specimens were loaded incrementally by increasing the gas pressure to the inflatable diaphragm of the load frame through a pressure regulator. The load and strains were recorded at each load step, and the edges of the specimens were simultaneously observed through the microscope for damage. The photographs of the specimen edge were taken using a digital 35-mm camera connected to the microscope for later retrieval and analysis. The experimental set-up for the procedure is described in [28]. The *in situ* observed damage in the two material systems is discussed below.

2.5.2.1 5HS Unbalanced (6:1) Laminate ($[0]_{2T}$)

The stress-strain curves of the laminate in the warp and fill directions are shown in Figure 51. The modulus (stiffness) of the laminate (being 6:1 unbalanced) in the warp direction was expected to be about six times that in the fill direction. However, the measured modulus of the laminate in the warp direction was found to be 7.53 times that in the fill direction. The extra compliance of the fill direction (or extra stiffness of the warp direction) may be due to the fact that the fill yarn waviness ratio was 2.4 times that in the warp direction. An attempt was made to observe damage for loading in the fill direction, but the failure of the laminate was catastrophic. Thus, no *in situ* damage observation was possible for loading in the fill direction.

However, in order to compare the damage evolution process with model laminate, woven laminate was tested in the warp direction for the *in situ* damage observation. Before any load application, the cross section of the specimen was inspected with an optical microscope. No process-induced cracks were visible on the specimen cross section. Upon application of incremental loading with the portable load frame, the first cracking (accompanied by an audible noise) occurred at a strain level of 0.35 percent ($3550 \mu\epsilon$), which was about 63 percent of the failure load. The first cracking appeared as interface cracks near the tip of the fill yarn bundles, as shown in Figures 53(a) and 53(b). With further increasing load, the yarn interface crack propagated along the interface from the tip of the yarn to the midsection of the yarn. At about 98 percent of the failure load (strain of $5690 \mu\epsilon$) intra-yarn delamination occurred near multiple sites of the yarn crimping, as shown in Figures 54(a) and 54(b). No fiber breakage was visible on the specimen cross-section at this strain level. However, visual inspection of the surface of the specimens, upon unloading, seemed to indicate that the delaminations of this nature occurred at other crimp locations along crimp lines, see Figure 55. Finally, the failure of the warp specimens occurred at the damaged locations along the crimp lines. Due to catastrophic failure, as mentioned before, no detailed observation was made on the failure mode of the fill specimens (i.e., loading in the fill direction of the composite). The failure modes of the warp and fill specimens of the unbalanced fabric composite are shown in Figure 56.

2.5.2.2 Model Laminate ($[90_2/0_2]_S$, $[90/0_2/90]_S$, 0.027)

The experimental procedure for the model laminate was the same as that of the unbalanced woven composite laminate. The model laminate contained lamina crimping only in the longitudinal direction. Thus the damage, except for the free-edge effects, should occur all throughout the width of the specimen. Both the edges (upper edge and lower edge) of the specimen, Figure 57, was inspected *in situ* for through-width damage assessment. The representative stress-strain curves of the model laminate is shown in Figure 52. The initial modulus (stiffness) of the laminate determined from the strain measured with the 1.57 mm gage was found to be 64.86 GPa. The 0.38-mm strain gage installed near the end of the crimp was used to record the local strain in the longitudinal direction, which is to be used in validating the analytical model. The first cracking in the model laminate occurred as a crack in the 90° lamina

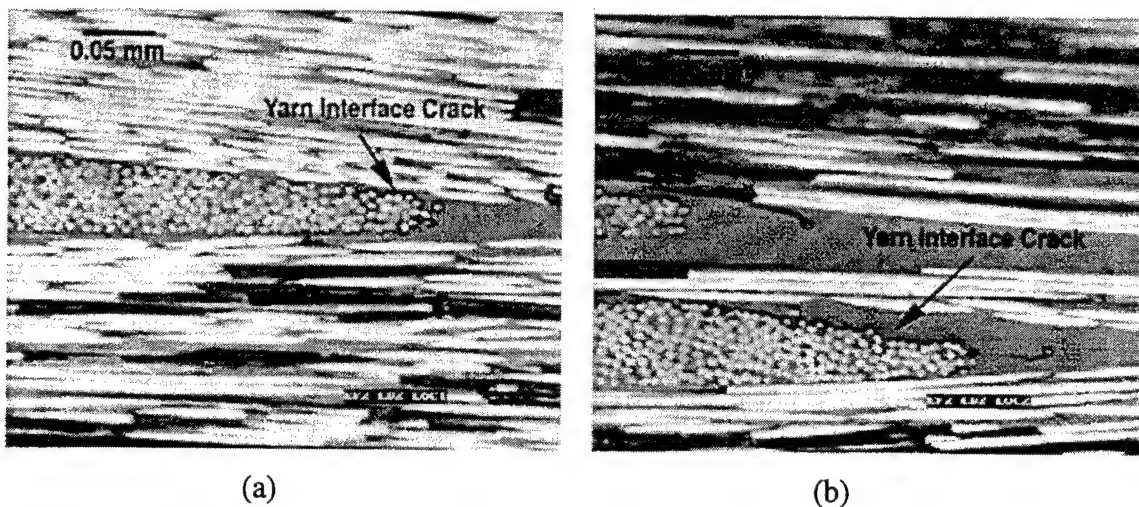


Figure 53. *In situ* Cross-sectional Micrograph of the 5HS Unbalanced (6:1) Woven Composite Specimen at Two Different Locations Indicating Initiation of Yarn Interface Cracks at 65 Percent of Failure Load (strain level: $3550 \mu\epsilon$).

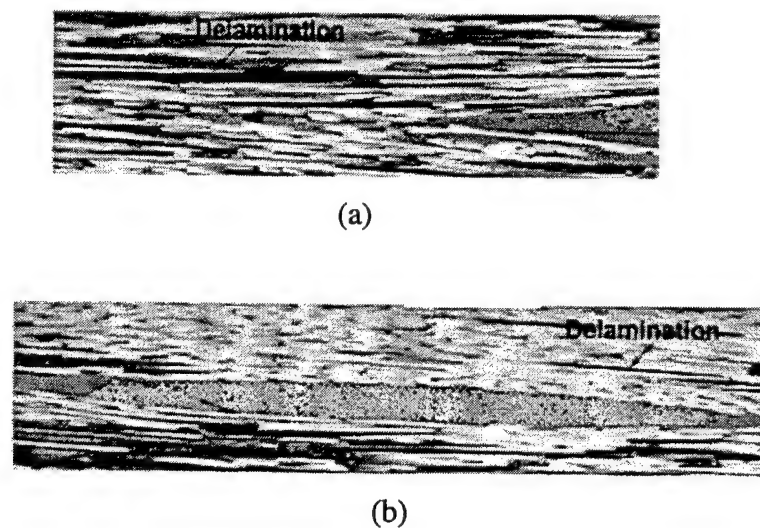
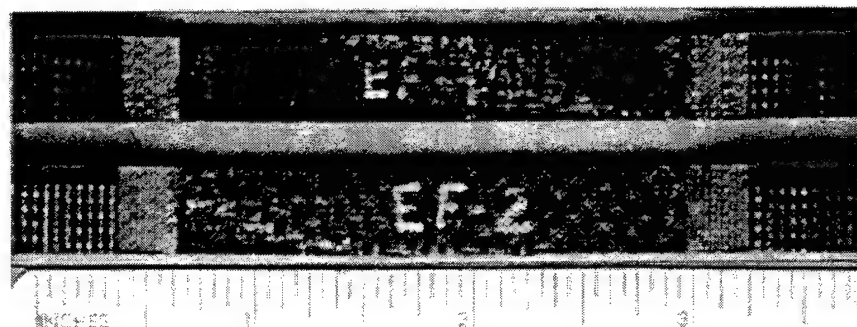
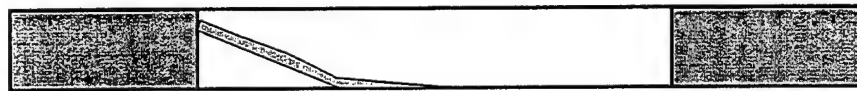


Figure 54. *In situ* Cross-sectional Micrograph of the 5HS Unbalanced (6:1) Fabric Composite Specimen at Two Different Locations Revealing Delaminations in the Vicinity of Yarn Crimping at 98 Percent of the Failure Load (strain level: $5690 \mu\epsilon$).



(a)



(b)

Figure 55. Surface of the Warp Specimens of Unbalanced Fabric Composite Revealing Damage Path. (a) Damaged specimens loaded up to 98 percent of the failure load, (b) Sketch of the damage locations of the specimens shown in (a).



Figure 56. Failure Modes in Warp and Fill Specimens of the 5HS Unbalanced Fabric Composites, Respectively.

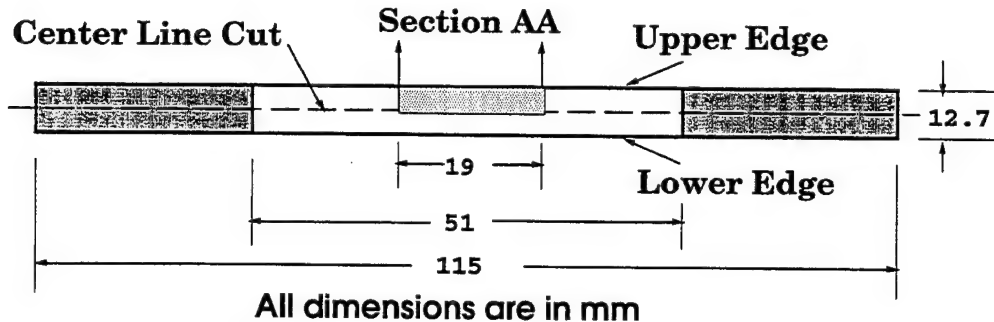


Figure 57. Specimen Geometry Description for the Damage Evolution Study.

near the wavy region, Figure 58, at a far-field strain of 0.37 percent ($3700 \mu\epsilon$). This crack propagated through out the width of the specimen, confirmed by the *in situ* observation of the lower edge of the specimen. It is to note that the mode and the far field strain for the first cracking in the case of other model laminates tested before, Roy [28], was the same as this model laminate [28]. With increasing load, the cracks in the 90° laminae grew further and started to branch out as interface cracks at the $0^\circ/90^\circ$ lamina-interface, Figures 59(a) and 59(b), at a far-field strain of 44 percent ($4360 \mu\epsilon$). The crack in Figure 59(a) is the same crack as shown in Figure 58, which was longitudinally at a distance of 1.76 mm away from the mid-point of the crimp. For convenience, the wavy region of the laminate is also denoted as lamina crimp location in this study. The crack in Figure 59(b) was located near the mid-point of the lamina crimp. These two cracks were located at different lamina crimp angles. Thus, the stress analysis for propagation of cracks like the two in Figure 59 should aid in developing yarn-interface crack growth criterion, which potentially will be used to understand the interface damage development process such as the yarn-interface cracks observed in the unbalanced woven composites earlier in this study.

Upon further load increase on the model laminate, some fiber breakage in the wavy region was visible at 90 percent of the failure load. Figure 60 shows such fiber breakage on the upper edge of the specimen. In order to inspect whether this type of fiber breakage occurred throughout the width of the specimen, the lower edge of the specimen was also microscopically observed. Figure 61 shows the *in situ* micrograph of the lower edge of the specimen at the same load level as was for Figure 60. The specimen was rotated longitudinally

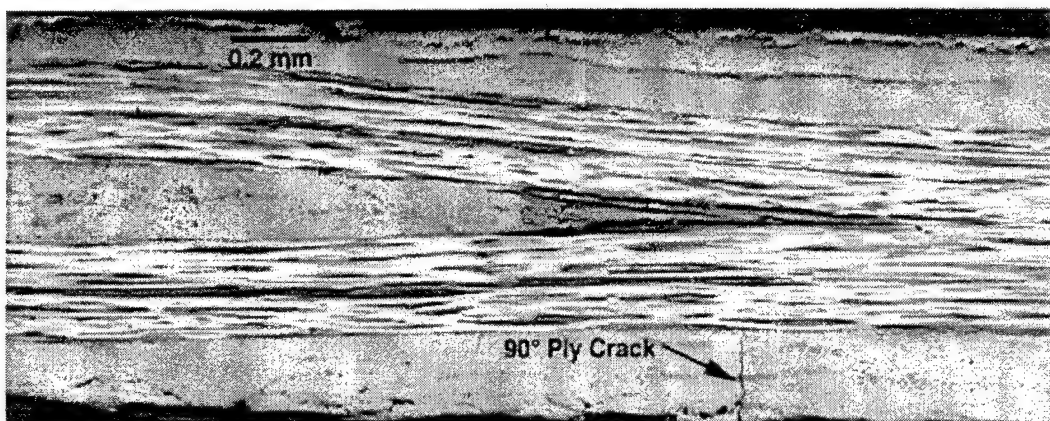


Figure 58. *In situ* Cross-sectional Micrograph of the Model Laminate at 37 Percent of Far-Field Strain ($3700 \mu\epsilon$). The crack is longitudinally 1.76 mm away from the middle of the specimen (mid-point of the ply crimp).

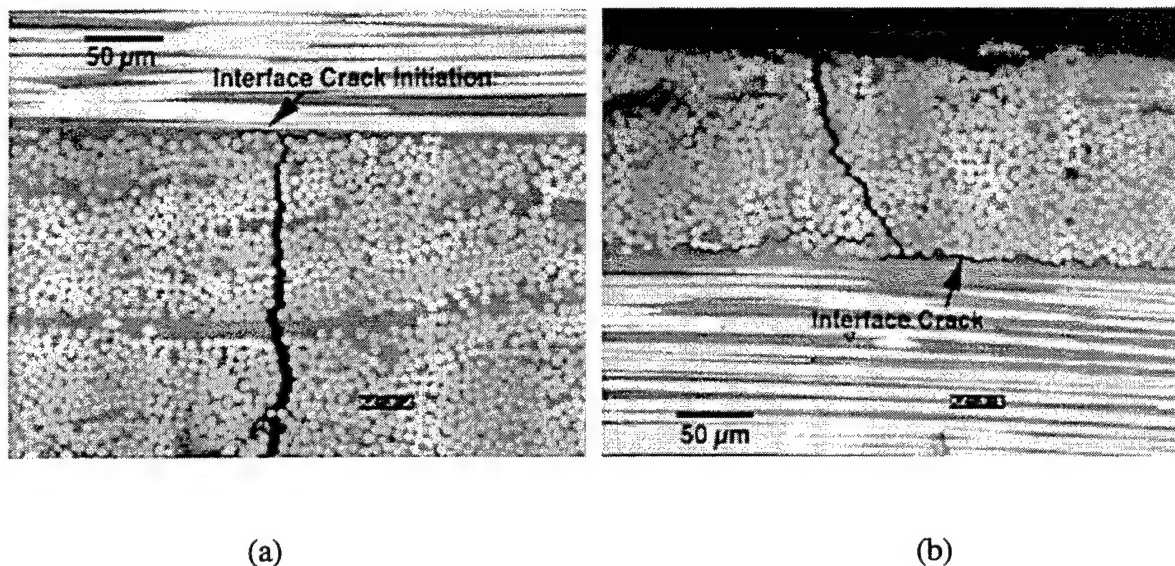
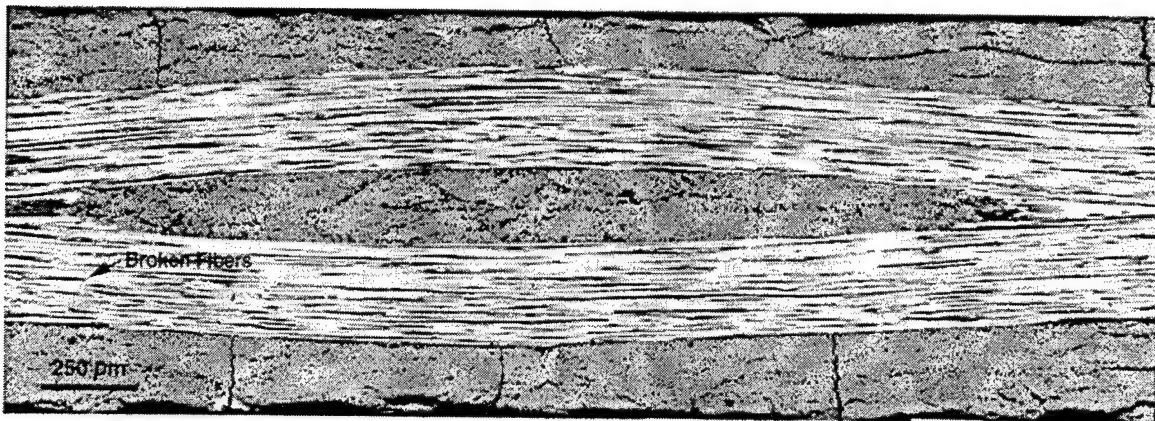
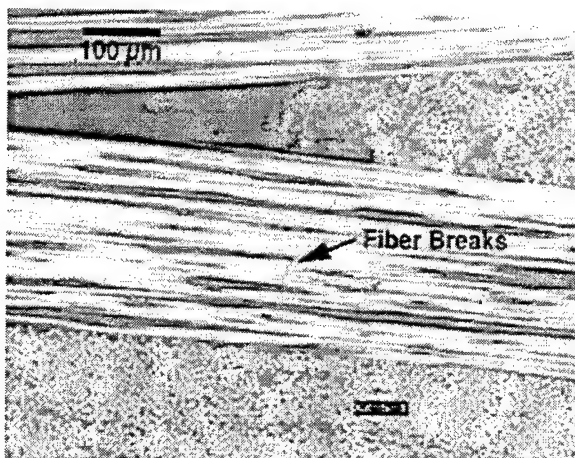


Figure 59. *In situ* Cross-sectional Micrographs of the Model Laminate at 44 Percent of Far-Field Strain ($4360 \mu\epsilon$): (a) Crack Shown in Figure 58, (b) Crack Located at the Vicinity of the Mid-point of the Lamina Crimp.



(a)



(b)

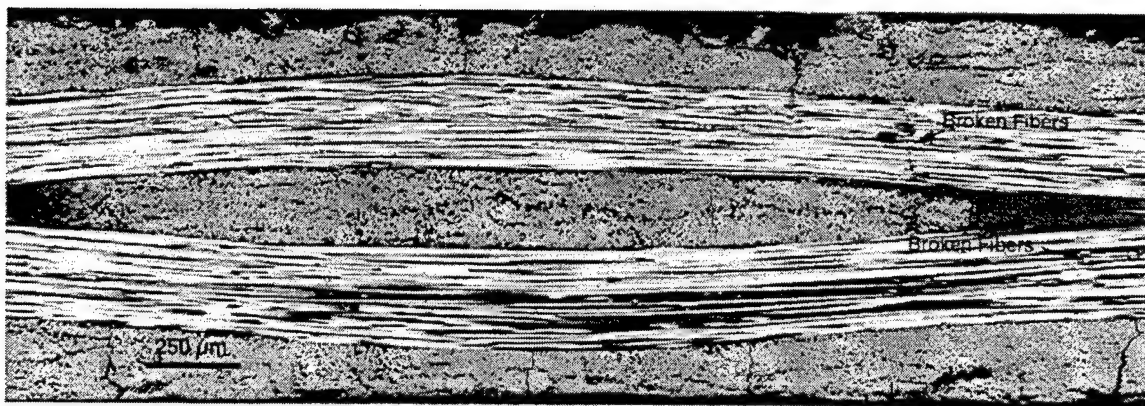
Figure 60. (a) *In situ* Micrograph of the Upper Edge of the Specimen at 90 Percent of the Failure Load. (b) An enlarged view of the area in (a) containing the broken fibers.

to take the micrograph of the lower edge, i.e., the top boundary of the micrograph in Figure 61 corresponds to the bottom boundary of that in Figure 60. The locations of the 90° cracks in these figures matched one to one, which implied that all the 90° cracks went throughout the width of the specimen (also confirmed by taking an x-ray image of the damaged specimen). However, the locations of broken fibers on these two edge micrographs did not have one to one matching. Further, to check whether any of these fiber breakages occurred in the interior of the specimen, the specimen was cut longitudinally along the centerline, as shown in Figure 57. A portion of

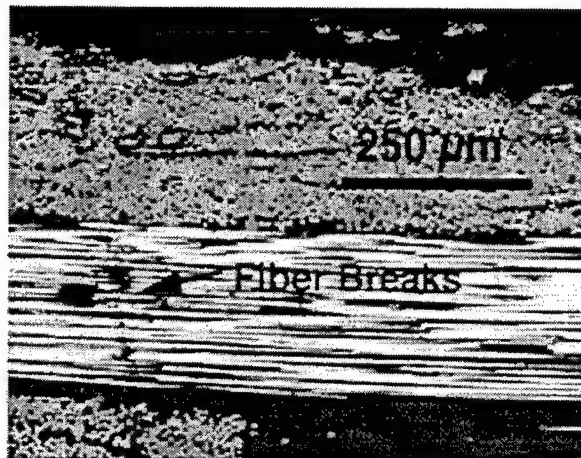
the cut edge of the specimen (Section AA, Figure 57) was polished to microscopically observe for broken fibers. The micrograph of the cut centerline edge is shown in Figure 62, which does not reveal any visible fiber breakage. The micrographs in Figures 60-62 thus implied that the fiber breakage did not occur throughout the width of the specimen. Further, this model laminate did not fail in the wavy region, like the other model laminates tested in another study of waviness ratio close to the present one [28]. All these observations, thus, implied that the fiber breakage mostly occurred close to the free-edge and was probably due to the free-edge stresses.

2.5.4 Conclusions

In order to develop an understanding of damage mechanism in woven composites, a comparative study of damage evolution in a commercial 5HS unbalanced (6:1) woven composite and a model laminate with planar crimping subjected to tensile loading was performed. The yarn waviness of the unbalanced woven composite along the warp direction was close to that of the model laminate. The damage development in the case of the woven composite was primarily in the form of cracking at the yarn interface and intra-yarn delamination near yarn crimping locations. Whereas, in the model laminate, the damage initiation was as cracks in the 90° laminae, which further grew as lamina-interface cracks. Some fiber breakage was also observed in the wavy region of the model laminate, but that fiber breakage phenomenon appeared to be restricted to the free-edge region. No large-scale lamina-interface crack was observed near the wavy region in the model system. However, the stress analysis for crack propagation, like that which occurred in the wavy region of the model laminate, should provide a stepwise understanding for developing yarn-interface crack growth criterion, which may lead to identifying the influence of the local stress components on the interface damage development process such as the yarn-interface cracks observed in the unbalanced woven composite used in this study.



(a)



(b)

Figure 61. (a) *In situ* Micrograph of the Lower Edge of the Specimen at 90 Percent of the Failure Load. (b) An enlarged view of the area in (a) containing the broken fibers.

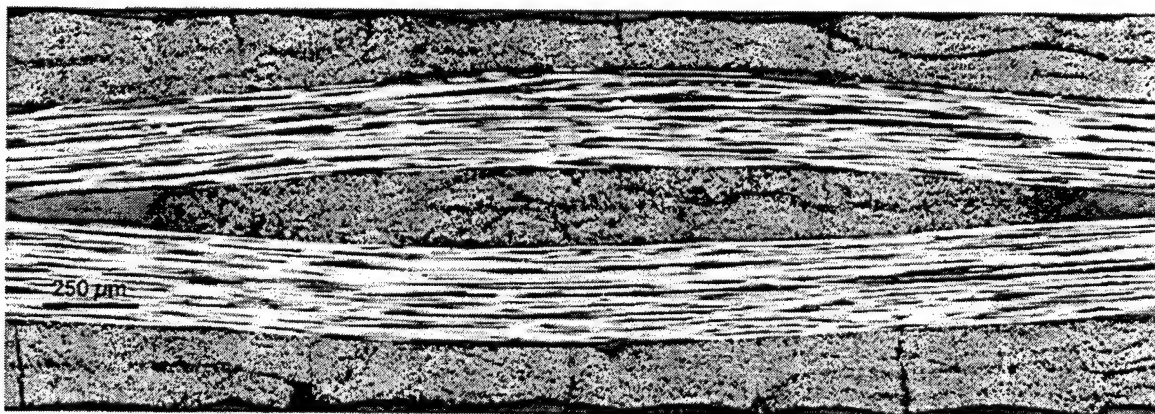


Figure 62. Edge Micrograph of Section AA Shown in Figure 57.

SECTION 3

PROCESSING SCIENCE OF COMPOSITES

3.1 INTEGRATION OF SENSORS FOR INTELLIGENT COMPOSITES PROCESSING

3.1.1. Neural Network for Prediction of Reaction Rate, Degree of Cure, Viscosity and dc-Resistance

Neural network models for the reaction rate viscosity and dc-resistance for Hercules 3501-6 resin have been developed and verified. The studies have shown that temperature and degree of cure can be used to predict the reaction rate, viscosity, and dc-resistance of the resin during cure with a high degree of accuracy. The use of neural network for modeling offers certain advantages over the conventional analytical model. The neural network models are easier to develop and tend to give better prediction simply because of the large number of parameters used for the network. It should be pointed out that although a large number of model parameters are used, *a priori* knowledge of the interactions of these parameters are not required. In particular, the neural network rate model implicitly contains information on the Tg of the resin at various degrees of cure such that the reaction actually stops at temperatures below Tg; while an analytical reaction rate model, such as the Arrhenius type rate equation, always predicts complete reaction given long enough time.

These models have also been incorporated into a one-dimensional heat transfer model which allows prediction of temperature distribution within a part during processing.

3.1.2 Neural Network for Prediction of Specific Volume Change During Cure

Some work has been done using neural network to model the specific volume change during cure for 3501-6. The neural network approach is expected to work well with better specific volume data obtained under constant temperature ramp rates. The approach is the same as the use of neural network for reaction rate prediction. In this case, the change in specific volume during cure is related to the temperature and the degree of cure.

Four sets of data have been processed. The inconsistency in the initial slopes at lower temperatures (below, say, 70°C) as shown in Figure 63 was thought to have been caused by noncondensable dissolved gas. By removing this gas volume (subtracting a quantity that is linearly proportional to temperature change), the corrected specific volumes show good

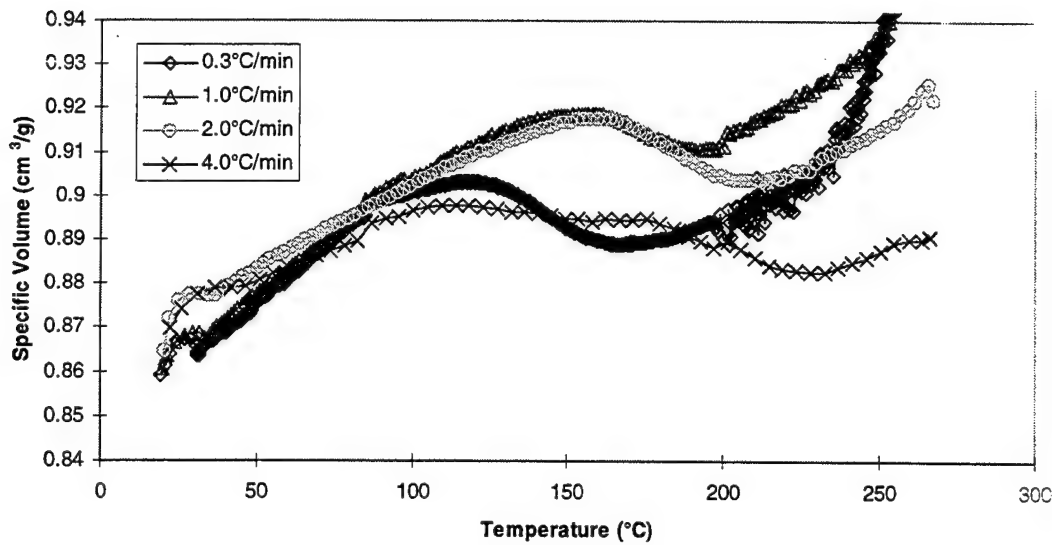


Figure 63. Specific Volume of 3501-6 During Cure (Raw Data).

agreement at the lower temperatures as can be seen in Figure 64. This correction was applied to data from previous experiments, and it was found that the inconsistencies in data might be eliminated by this correction.

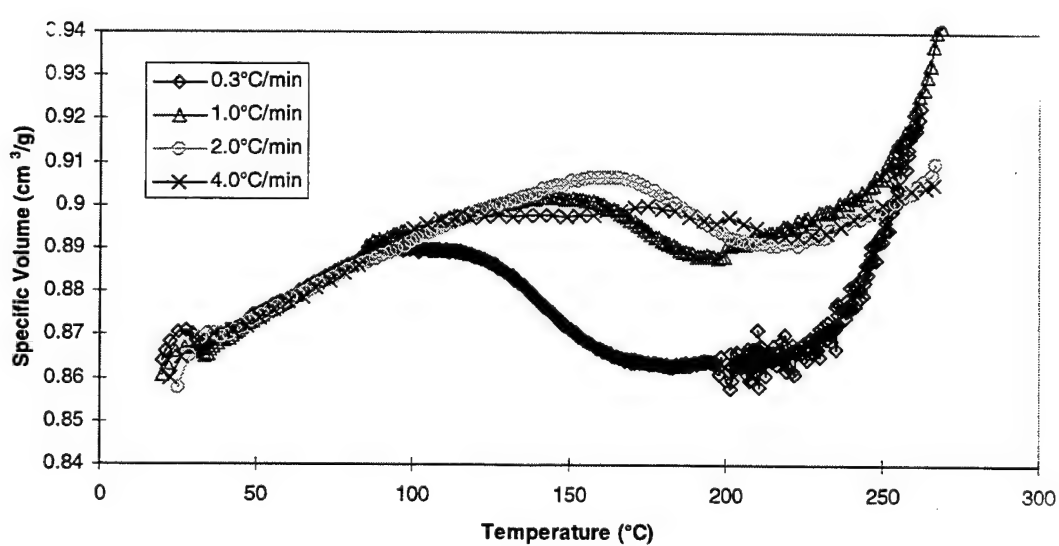


Figure 64. Specific Volume of 3501-6 During Cure (After Correction for Volume of Noncondensable Gas).

However, further experimentation indicated that the variations might have been caused by dissolved moisture rather than noncondensable gas as indicated by a very large volume change at about 310°C in Figure 65. The samples were tested under a constant pressure of 10 MPa, which is close to the vapor pressure of water at this temperature. Further work is required to resolve the problem.

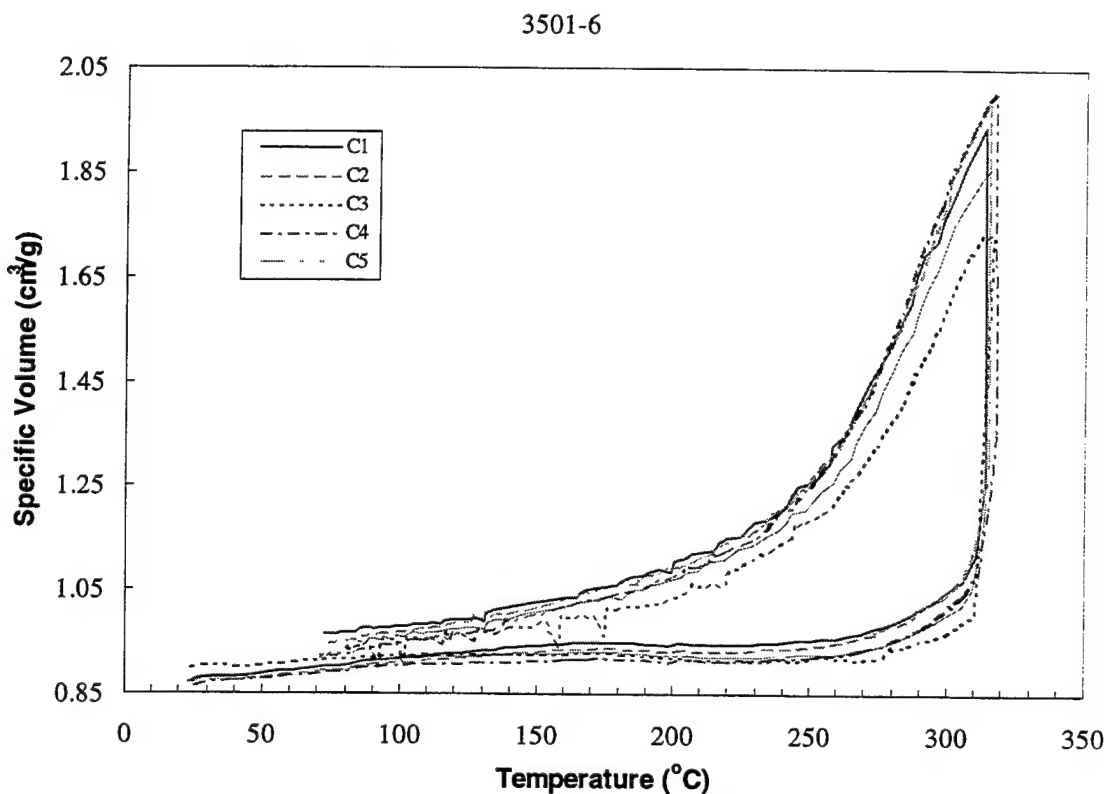


Figure 65. Specific Volume of 3501-6 During Cure.

3.1.3 Thermal Conductivity Measurement

Software for shutter control and temperature measurement has been completed and tested. A simple method has been developed for thermal diffusivity determination based on the slope and intercept of the temperature response on the backside of the specimen to a constant heat flux on the front side. However, tests have shown that for high conductivity material, unless

the sample is sufficiently thick, the rapid response in temperature results in a very small intercept that leads to very large errors in determining the thermal diffusivity.

3.2 LOW-COST RESIN INFUSION PROCESSING

Historically the vast majority of aerospace composite parts have been fabricated through hand lay-up of preprints followed by autoclave consolidation and cure. Recent efforts to reduce the cost of composite parts have led to a number of research initiatives. One initiative is the use of braided, woven, or sprayed dry preforms which utilize machines rather than humans to achieve the proper fiber orientations. This approach reduces both touch labor and raw material costs. A variety of techniques have been developed to infiltrate this dry preform with resin to make the final part. Among these are RTM, SCRIMP and RFI.

Our desire is to develop a low-cost process which can be used to manufacture quality, high fiber volume parts ranging from production units of one to several thousand. The process should ideally require only low-cost or *in situ* tooling (foam core), minimize raw material waste, minimize touch labor, minimize consolidation pressures (outside autoclave) and be highly reliable (large integrated preforms will represent substantial investment because of their size). The SCRIMP process seems best suited to meeting these goals; however, it must be adapted for conventional aerospace preforms and resins. The unique approach UDRI has chosen to pursue, for dry preform resin infusion, is termed Pressure Assisted Vacuum Bag Resin Infusion, PAVBRI.

The PAVBRI system that UDRI is currently building consists of a computer-controlled peristaltic pump to be used for pumping the resin at desired locations in the preform, and a 24-channel output board for controlling line and tool heaters, resin manifold gates and vacuum manifold gates. The system will also have 40 channels for data acquisition to be used for temperature and resin ionic viscosity measurements.

The resin system under investigation is an aerospace grade epoxy from 3M, called PR520. It is a 177°C cure, toughened epoxy which is premixed and stable at room temperature. The resin's curing agent is a solid, in suspension with the resin. The solid melts and goes into solution at approximately 150°C. This resin mix presents both an opportunity and challenge because the resin can have a very low viscosity and long pot life if kept below 150°C, but there is a chance that injection prior to placing the solid into solution could result in filtering by the fiber

bed. One approach to this problem is to heat the injection line to a high temperature to achieve resin solution rather than the whole resin pot.

The fiber preforms to be investigated will be aerospace grade materials with industry acceptance. Carbon and glass fabrics of various constructions have been evaluated in terms of their compressibility by pressing a 16-ply, warp-aligned lay-up between two plates which are mounted in the Instron load frame. A compressibility curve representing fiber volume versus pressure has been generated to determine the maximum achievable fiber volume for a particular consolidation pressure, such as 14.7 psi for a vacuum bag. The results of this study are summarized in Table 7 by determining pressure requirements for achieving 50, 55, and 60 percent fiber volumes. As expected, it is not possible to achieve fiber volumes of 55 percent with conventional fabrics using only vacuum bag pressure. Ongoing efforts to increase the net fiber volume using a vacuum bag cure include selection of new fabrics and preconsolidation techniques.

TABLE 7
SUMMARY OF FABRIC COMPRESSION STUDIES

Sample No.	PVF	PVF	PVF	Description
	50% psi	55 % psi	60% psi	
PAVBRI-A	12	34	105	Glass, 2x2, twill
PAVBRI-B	7	20	65	Glass, uniweave, 95x5
PAVBRI-C	79	250	*****	Carbon, 3HS
PAVBRI-D	19	42	91	Carbon, plain weave
PAVBRI-E	45	190	*****	Carbon, plain weave
PAVBRI-F	23	76	*****	T650-35, uniweave, UGH155-12"-PW
PAVBRI-G	12	37	155	T650-35, G105-42"-8HS
PABBRI-H	140	*****	*****	Glass, plain weave
PAVBRI-I	8	17	45	T300, 8HS, 24x25
PAVBRI-J	27	83	*****	T300, plain weave, 3K, 12.5x12.5

SECTION 4

CARBON-CARBON AND CARBONACEOUS MATERIALS/TASK 4

4.1 CARBONIZATION OF PITCH AND OTHER CARBON-CARBON PRECURSORS

Thirty-three carbonization runs were made during the reporting period. A variety of materials were run including pitch resin, phenolic composites, high char yield resins, University of Akron fibers, natural materials, pitch foams, and pitch fibers. The carbonization furnace, pitch reactor, and incinerator are now all connected to allow simultaneous operation of the furnace and reactor, greatly increasing the amount of experiments that can be run.

4.2 CHARACTERIZATION VAPOR-GROWN CARBON FIBERS

In the last year there has been three lots of vapor-grown carbon fibers from Applied Sciences Inc. (ASI) for x-ray diffraction analysis (XRD). This work is in support of the Air Force CRADA with ASI. The primary measurement for these fibers is degree of graphitization (g_p) with crystallite size and other crystalline phases as secondary measurements of interest.

The first lot of fibers consisted of four samples. The XRD results are summarized in Table 8. These four samples have significantly lower degrees of graphitization compared to previous Pyrograf III™ fibers ($g_p = 0.6 - 0.7$) [29]. The two samples of PR-12 were essentially identical (single entry in Table 8) with a $g_p \approx 0.4$ but there is another peak near turbostratic carbon which constitutes a significant portion of the fiber. There is also amorphous diffraction in these samples. The PR-18 samples also showed a turbostratic carbon peak but it constituted much less material than in the PR-12 samples. They also contained amorphous material. The degrees of graphitization are given in the table below. The graphite in "Dark" PR-18 was very similar to PR-12 while the "Light" PR-18 had a degree of graphitization even lower than PR-12. The second lot of fibers consisted of 10 samples; the results are shown in Table 9. Samples # 1, 5 through 7, and 9 all had degrees of graphitization in the 40 percent region, similar to the PR-12 and PR-18 samples from lot #1. Samples #2 and 8 had g_p s lower yet (22 and 32 percent) but were still graphitic. Samples #3, 4, 10 had some turbostratic carbon but no graphite diffraction. In fact, sample #4 was mostly amorphous with barely enough turbostratic carbon to detect and sample #10 was dominated by the amorphous content. The only sample in this lot to show any peaks in addition to graphitic carbon was # 8, which showed a peak apparently from the catalyst.

TABLE 8
XRD RESULTS FOR LOT #1 PYROGRAF III™ FIBER

Sample	d-spacing (nm)		g _p
PR-12	0.3407		0.387
	0.352	Amorphous and turbostratic carbon	
PR-18	Dark	0.3409	0.363
		0.356	Amorphous and turbostratic carbon
	Light	0.3424	0.183
		0.362	Amorphous and turbostratic carbon

TABLE 9
XRD RESULTS FOR LOT #2 PYROGRAF III™ FIBERS

No.	Designation		d-spacing (nm)	g _p	L _C (nm)	G (%) ^a
1	AN5-1	sh 1-5	0.3408	0.375	6.5	79
2	AN2-110	sh 81-90	0.3421	0.220	5.7	72
3	AN2-109	sh 61-70	0.3459	b	3.2	0
4	AN2-109	sh 1-10	0.3445	b	3.6	0
5	AN2-105	sh 1-7	0.3409	0.366	5.8	20
6	AN2-108	sh 31-40	0.3406	0.391	9.9	30
7	AN2-108	sh 61-70	0.3405	0.410	10.0	45
8	AN2-104	sh 41-50	0.3413	0.318	9.2	30
9	AN2-110	sh 41-50	0.3401	0.451	7.4	56
10	AN4-98	sh 1-40	0.3467	b	4.0	0

a. Percent of graphitic carbon out of the total graphitic and turbostratic carbon.

b. Turbostratic carbon

According to ASI's description of the samples, the catalyst is injected 2" beyond the endcap in #3 and through a different port in #4. Apparently where the catalyst is injected is important to the process. Also the fibers are not the same as-grown versus fattened (#10) in the Pyrograf-I™ reactor.

There has always been some turbostratic carbon and amorphous diffraction in Pyrograf-III™ samples but the some of this lot's samples no longer show graphitic carbon. Also, the amount of turbostratic carbon relative to graphitic was always low. This is still true for samples # 1 and 2 but for samples #5 through 9 the ratios of carbon types are closer to 50 percent or less as seen in the last column in the table.

There were only two fiber samples in the third lot of fibers (see Table 10). Both of these fibers had low degrees of graphitization and relatively small crystallite sizes. This is a bit surprising considering the ANX fiber was an unthickened fiber which should have the greatest degree of graphitization. The AN2 sample was essentially turbostratic.

TABLE 10
XRD RESULTS FOR LOT #3 PYROGRAF III™ FIBERS

Designation	d-spacing (nm)	g_p	L_c
ANX-100 145	0.3428	0.134	3.2
AN2-178	0.3440	0.006	4.1

4.3 INTELLIGENT PROCESSING OF CARBON-CARBON

This effort involves developing sensors to determine processing parameters that effect pitch processing. The current sensor being used is the Cahn TGA connected to a Hewlett-Packard GC/MS. Real-time measurements have been attempted with limited success. The problems encountered are in the transfer line mechanism which is heated to facilitate the transfer of gases from the TGA to the GC/MS. Currently the gas stream is collected in a separate vessel. The gas condenses on the sidewalls and then solvent is used to extract the samples for injection into the GC/MS. Toluene is used as the primary solvent along with methanol and acetone. This technique has provided some insight into the types of materials coming off the pitch powders.

The toluene-extracted samples yield high molecular weight materials such as pyrene, fluoranthene and phenanthrene. These materials consist of multiple fused benzene rings. The current effort focuses around development of a transfer line system that can accommodate the high temperatures needed to completely transfer the gas stream from the TGA to the GC/MS. This involves heating the top portion of the Cahn with heating tape while maintaining the transfer line temperatures above 350°C. Once the transfer line is complete, operational tests will be conducted and the unit transferred to the carbonization furnace.

4.4 SINTERED CARBON PROCESSING

The rapidly increasing number of potential applications for carbon products and carbon-carbon composites have found limited commercial success due to material design complexities and the high cost of manufacture. Traditionally, these materials would be produced by repeated impregnation, carbonization, and graphitization, or by chemical vapor infiltration of a fiber pre-form. This investigation focuses on the broadening of a technique originally referred to as binderless graphite and more recently called sintered carbon. The intent is to identify conditions and a process window in which fibers or precursor fibers may be compacted in a press mold, and sintered to produce a high-density, self-reinforced carbon material in a single step (without the need for densification). This process should be much lower cost than any current processes due to the significant reduction in process time and complexity.

4.4.1 Sintered Pitch Panels

Details of the initial work can be found in last year's annual report [29 and 30]. A follow-up study was made using a large batch of pitch powder having ~9.4 percent wt. gain and pressing at increasing pressures and temperatures (shown in Table 11). These panels were made in the same 2" by 6" mold as the initial study using the same mold filling, pressing, and removal. These panels were all made on the small press used in the initial study.

The resulting panels showed very good compaction and sintering properties, but lacked extraordinary strength. The results compared well with panels produced with 8 percent and 10 percent weight gain in the previous study and confirmed the repeatability of the in-house sintered carbon process. The observations of the panels are also shown in Table 11, but none of these panels are bloated, warped, cracked or spalled.

TABLE 11
PRESSING CONDITIONS AND PROCESSING SUCCESS

<u>Sample ID</u>	Pressing Conditions			Pressing Results		
	<u>Temp. (°C)</u>	<u>Pressure (psi)</u>	<u>Bloating</u>	<u>Warpage</u>	<u>Cracks</u>	<u>Spalling</u>
25-500	25	500	0	0	0	0
25-1625	25	1625	0	0	0	0
75-1675	75	1675	0	0	0	0
75-5000	75	5000	0	0	0	0
150-500	150	500	0	0	0	0
150-2750	150	2750	0	0	0	0
225-2750	225	2750	0	0	0	0
225-5000	225	5000	0	0	0	0

The mechanical testing of the carbonized panels and the carbonization results are shown in Table 12. Char yields were all approximately 79 percent with uniform shrinkage in all directions. The volumetric changes were greater than char yield which means the samples should have had a greater density than the starting panels. Mechanical evaluation of carbonized and graphitized flexural coupons confirmed the relatively low strengths of the non-reinforced carbons.

Additional sintering work now requires the addition of fibers to the pressing matrix to see if the ability to make panels out of pitch can be extended to making composites.

4.4.2 Composite Panel Production

In order to produce a uniform distribution of pitch powder within as well as between the tows of fiber, a water-based suspension prepegging technique was developed. Colloidal suspensions of pitch powder in water were produced by high shear rate mixing of 30-40 percent powder, 10 percent glycerin, 1 percent poly(acrylic acid), and <1 percent Triton X100

TABLE 12
PHYSICAL AND MECHANICAL RESULTS DATA

<u>Sample ID</u>	<u>Strength</u>	<u>Modulus</u>	<u>Char Yield</u>	<u>Changes in</u>		
	<u>(psi)</u>	<u>(ksi)</u>	<u>(%)</u>	<u>Length</u>	<u>Width</u>	<u>Thickness</u>
25-500	609	211	79.1	0.86	0.86	0.85
25-1625	Na	Na	79.1	0.87	0.87	0.85
75-1675	927	545	79.3	0.86	0.86	0.85
75-5000	1478	1066	79.1	0.86	0.86	0.85
150-500	106	216	78.8	Na	0.87	0.85
150-2750	243	1166	79.1	0.86	0.86	0.84
225-2750	1369	1351	79.2	0.87	0.90	0.84
225-5000	1754	1349	79.4	0.86	0.86	0.88

(surfactant). The suspensions were placed in the bath of a thermoplastic prepegging die and the fiber was drawn through the die. Dimensions of the final die orifice were of the most critical concern during the development of this process. Although the viscosity of the suspensions could be effected by changing the composition, a larger die could make-up for a mixture that was too thick. More important even than die size was the sharp edge of a ground glass die which acts to break fibers during their passage out of the die. Die pressure is necessary to force the powder into the tows, but this pressure will cause fibers to break if the exit orifice is too sharp or contains rough edges. Once a median die size is determined for a given tow size and fiber type, a precision die should be machined with a small radius at the exit, but unless fiber breakage becomes excessive, cut and ground glass pipets should be sufficient for this study.

Prepegging using furfural alcohol was also attempted using two different catalysts in varying concentrations, but analysis of prepegged tows showed no penetration of powder into the tows. The contrast of this result to the water-based suspensions suggests that the capillary

attraction resulting from the hydrophile-lipophile balance of the suspension mixture draws the powder into the fine interstices between carbon filaments.

The water prepregged fiber tows do not adhere to each other or the drum release ply. The powdered tows were removed from the drum, bundled by hand, and cut into 6" lengths. The 6" tow sections were placed a bundle at a time into the 2" by 6" mold. A tackifier is needed for use with the above prepregging technique in order to use more conventional lay-up techniques.

To date, all composite panels produced using this method contained far too little matrix material to achieve the expected composite properties. In fact, so little matrix was present that the preforms failed to remain compacted after even successive high temperature and pressure compactations vigorous enough to cause severe fiber damage. However, the loosely compacted panels with very little matrix did in fact shrink significantly during carbonization, encouraging additional work in this area. Although not dense enough to machine into mechanical test specimens, the composite panels provided interesting microstructural analysis. PLOM showed a fine mosaic structure present within the fiber tows (Figure 66) and SEM showed sintering of particles within this mosaic structure (Figure 67).

The current development work used AS-4 PAN-based carbon fiber. This was used during development because of its ready availability. Commercially available carbon fibers were evaluated for the most economical selections for developing high stiffness and high thermal conductivity (K). Mitsubishi Chemical K321-10 and Amoco P30X stood out as industry competitors for this emerging market. Both exhibit heat-treatable properties, most notably an increase in thermal conductivity can be induced through high temperature $>2300^{\circ}\text{C}$ heat treatment as is common in carbon-carbon production. In carbon-carbon composites requiring high-K fibers these can be lower cost due to lower process temperatures during manufacture and a more handleable fiber for difficult composite processes. The K321-10 performed much better than AS-4 in the above powder prepregging technique and would result in a lower processing cost due to less fiber breakage and subsequent clogging of the die.

4.4.3 Pitch Analysis - Thermoplasticity

The experimental thermoplasticity test was performed on pitch from each oxidation level used in the original sintering study (2 - 10 percent weight gain) [29]. A standard TMA vertical penetrator equipped with a conical tip probe was used with a 1g load to perform

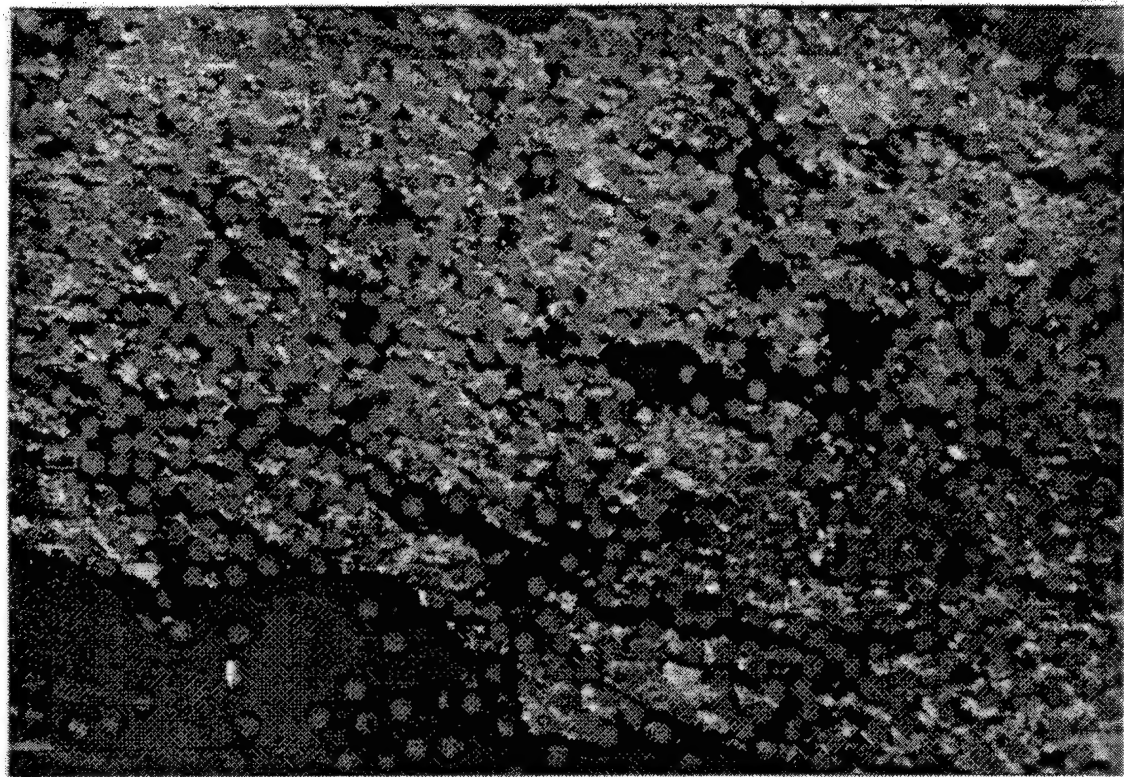


Figure 66. Polarized Light Optical Micrograph Showing Distribution of Anisotropic Powder within the Fiber Tows.

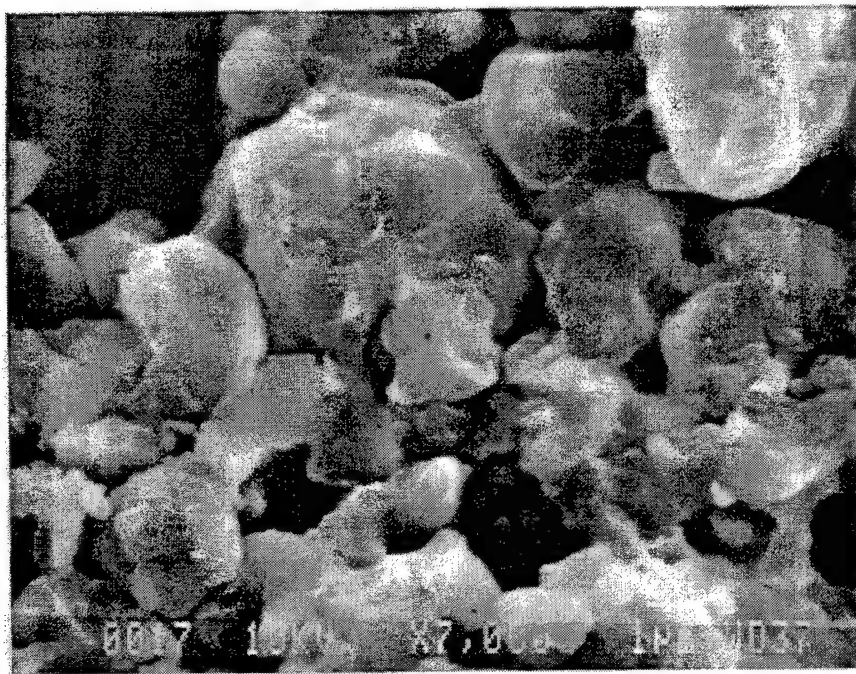


Figure 67. SEM of Sintered Microstructure.

the penetration test. Specimens were prepared by pressing in a 20-mm diameter pellet press under 5000 psi for 5 minutes at room temperature. The penetration curves behaved as expected with similar slopes and decreasing penetration depths with increased oxidation times. However, results of specimens compacted according to the conditions prescribed in the original test matrix (for a range of temperatures, pressures and times) were more complex. These preliminary results were reported earlier [30].

After numerous attempts to understand the behavior of normalized curves of the penetration portion of the test curves, the complete traces of the raw data proved to be more useful. As later confirmed by Huttinger's group [31], slight increases in glass transition temperature can be observed for increasing oxidation times. More interesting were differences in the non-linearity of the thermal expansion prior to the onset of penetration. Several samples expanded due to formation of large pores during the rapid heating rate. The heating rate of 10°C per minute is much higher than the 1-2°C heating rate used during the sintering process and resulted in expansion rates higher than the sample CTE as the gases are trapped in expanding closed pores. As the material began to soften large pores formed, rapidly creating large discontinuities in the penetration curves and rendering the higher temperature data useless for those samples.

4.5 STABILIZATION OF PITCH

4.5.1 Internal Stabilizers

Materials that may act as stabilizers were added to Mitsubishi AR pitch and then pressed into a composite. The pitch was first jet-milled into a fine powder (1-3 μm diameter). The additives were dissolved in tetrahydrofuran (THF) and the pitch added to make a slurry which thoroughly dispersed the additive into the pitch. When the THF was evaporated, the dry pitch/additive mixture was lightly crushed and the powder placed between pieces of T-300 fabric. This sandwich was then pressed together at temperature. Part of the composite was kept for microstructural evaluation and the rest examined after carbonization. Table 13 gives the pressing conditions and additives examined.

Some of the "A" samples were used to test various pressing conditions to produce composites which held together. The 300°C and 100-psi pressing conditions were settled on as a standard for future work. The carbonization results are shown in Table 14. The bloating was very low for composites made under these conditions.

TABLE 13
PRESSING CONDITIONS AND ADDITIVES FOR PITCH COMPOSITES WITH
INTERNAL OXIDANTS

Sample	Press Temperature (°C)	Pressure (psi)	Additive	Additive Level (% of pitch)
A1	250	300	None	0
A2	300	300	None	0
A3	250	0	None	0
A4	300	300	None	0
A5	300	100	None	0
A6	300	100	SC1008 phenolic	100
A7	300	100	SC1008 phenolic	11
A8	300	100	SC1008 phenolic	26
A9	300	100	Furfuryl alcohol	10
A20	300	100	Furfuryl alcohol	26
A11	300	100	None	0
B1	300	100	Benzoquinone	9
B2	300	100	Benzoquinone	25
B3	300	100	Furfuryl aldehyde	10
B4	300	100	Furfuryl aldehyde	26
B5	300	100	Maleic anhydride	10
B6	300	100	Maleic anhydride	28
B7	300	100	None	0
C1	300	100	Benzoquinone	20
C2	300	100	SC1008 phenolic	20
C3	300	100	Furfuryl alcohol	20

TABLE 14
CARBONIZATION RESULTS FOR PITCH COMPOSITES CONTAINING INTERNAL
OXIDANTS

Sample	Matrix Char Yield (%)	Bloating Index	Interlaminar Tensile Strength (psi)
A1	32	4	
A2	33	2	
A3	18	4	
A4	40	0	
A5	34	0	
A6	68	0	
A7	25	0	
A8	29	0	
A9	21	0	
A10	0	2	
A11	21	0	
B1	79	0	
B2	75	0	
B3	77	0	
B4	69	3	
B5	73	0	
B6	64	0	
B7	71	0	
C1	49	4	171.6
C2	50	4	110.3
C3	77	1	31.1

Of the additives attempted in the "A" series, none were as successful in terms of char yield as simply using a phenolic resin as a matrix. A new set of additives was used in set "B" which also allowed a larger amount of pitch to raise the matrix volumes. These additives did increase the matrix char yield. The higher additive loadings resulted in slightly lower char

yield. Set "C" was prepared making larger composite samples (8-ply 2" x 6") for mechanical testing; these samples contained internal stabilizers at the 20 percent level.

Interlaminar tensile strengths (ILT) for the "C" samples were quite low. Examination of the composites showed that only a small amount of pitch was deposited between the fabric layers and significant voids were present within the fiber bundles. The difficulty in getting the pitch uniformly dispersed within the composite is a definite problem. Additional work in this area will be conducted only when good penetration of the pitch into fiber bundles can be accomplished with sufficient pitch retained between bundles to hold the composites together.

An attempt was made to incorporate partial carbonized AR pitch into a composite. The processed pitch was combined with T-300 fabric and melt pressed into composites under nitrogen. While these composites did not bloat on carbonization, the penetration of pitch into the fiber bundles was insufficient to produce composites which held together. No further work in this area is planned.

4.5.2 FTIR Studies of Pitch

Additions to the FTIR spectra database on pitches continued in this reporting year. Data on carbonized and partially carbonized AR was added which showed that the loss of aromatic hydrogens in the lower wavelength region accessible to the *in situ* fiber optic sensor is easy to follow by FTIR. Other pitches examined were Aerocarb-80 and the Conoco bicomponent pitches as well pitches at various states of stabilization.

Quantification of oxidation levels is still not possible but curve fitting of the spectra of stabilized Aerocarb-80 pitch revealed that the peak at 1600 cm⁻¹ started to broaden on oxidation but not to the same extent as AR. This peak's position remained fixed in Aerocarb-80 while in the AR pitch the peak shifted slightly higher frequencies. This data supports the concept that an additional oxygen containing moiety is absorbing near 1600 cm⁻¹ in AR but why the chemistry of this pitch should be different from Aerocarb-80 is unknown.

4.5.3 Thermal Oxygenation Study

An investigation of oxidation temperature and the potential to induce oxygen uptake while limiting oxidative reaction was initiated after discussions with C. C. Fain of Clemson University. Jet-milled Mitsubishi AR mesophase pitch was treated in air at 150°C for varying times (24 - 196 hrs), and at 140, 160, 170, and 180°C for 48 hours each. The amount of

weight gain was linear with time at 150°C as shown in Figure 68. There also appeared to be a linear increase in weight gain with temperature through 170°C as expected [32] (see Figure 69). The ability of the pitch to pick up oxygen at higher temperatures was restricted as the 180°C sample picked up the same weight in 48 hours as did the 150°C sample. The 6 percent oxygen uptake standard in our laboratory can be attained in only a few days at these lower temperatures.

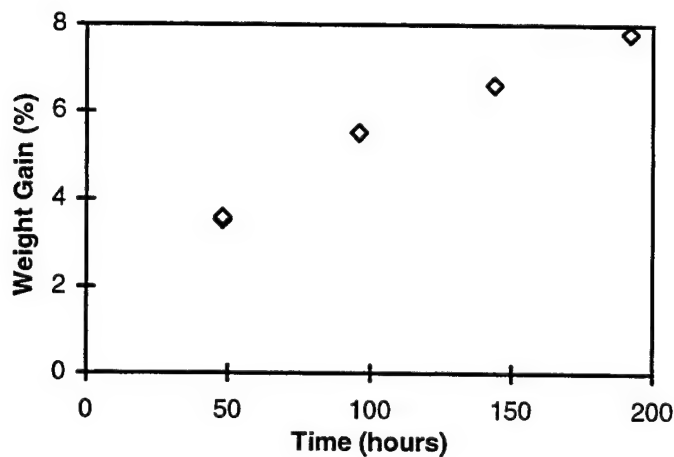


Figure 68. Weight Gain of AR Pitch in an Air Oven as a Function of Time at 150°C.

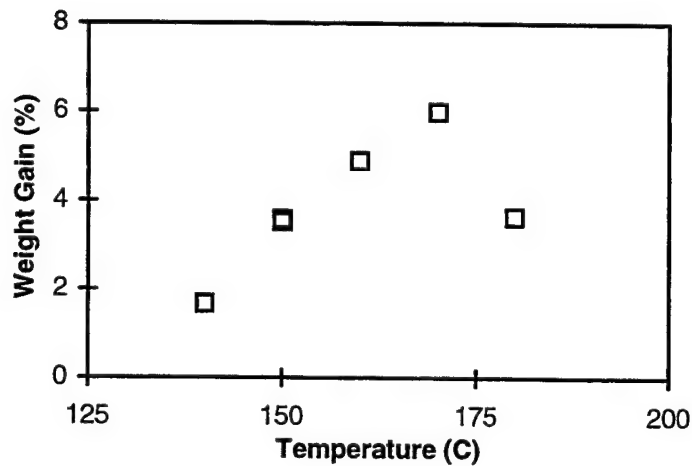


Figure 69. Weight Gain of AR Pitch in an Air Oven as a Function of Temperature for 48 Hours.

Pellets were made from this pitch and carbonized. The superiority of the lower temperature oxygenation was demonstrated by the fact that the pitch heated to 170°C still bloated slightly. This indicates nonuniform oxygen uptake due to partial reaction at that temperature. Pellets made from the pitches oxygenated at 160°C for 48 hours and at 150°C for 144 hours and longer did not bloat.

The thermoplasticity test [31] (a modified TMA test) gave good correlation between temperature of oxidation and oxygen weight gain versus the penetration and bloating temperatures. The higher oxidation weight gains expanded to a higher temperature before penetration. This can be seen in Figure 70 where the 150°C for 48 hours pitch behaved the same as the 180°C pitch for 48 hours; both pitches gained about 3.5 percent oxygen. Pitch which had gained ~6 percent oxygen was the 170°C for 48 hours and the 150°C for 144 hours also shown in Figure 70 which were not penetrated until much higher temperatures. Samples with weight gains in excess of 6 percent also did not bloat during this test confirming the required level of stabilization.

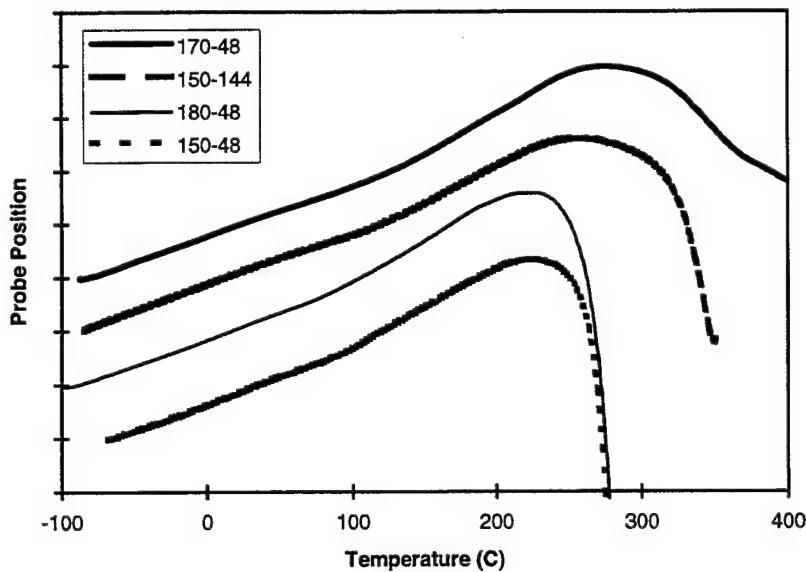


Figure 70. Expansion and Penetration for Several Buttons Made with Pitch Treated at the Temperatures and Times Listed.

Since the oxygen isn't supposed to react with the pitch at these lower temperatures, several tests were conducted on the pitch. The first was a simple weight loss study

which showed the pitch does not lose any mass on sitting; therefore the pitch could be stored between treatment and use.

FTIR on the oxygenated pitch showed the same ether, carbonyl, and hydroxyl peaks as in pitch oxygen stabilized at higher temperatures. This indicates that at least some of the oxygen does react. Even if the oxygen does react, the pitch behaves significantly different than pitch stabilized at higher temperatures: it feels wet and sticky while the stabilized powder is dry with hard crusty regions.

Several composites were made from the oxygenated pitch from Clemson University. This pitch was essentially identical to our 160°C for 48 hours. The composites were made in the same fashion as the internal oxidants composites with the pitch powder placed between T-300 fabric sheets and pressed together. Table 15 has the conditions of the composite fabrication.

TABLE 15
PRESSING CONDITIONS FOR “FAIN” STABILIZED PITCH COMPOSITES

Sample	Press Temperature (°C)	Pressure (psi)	Pitch
U1	300	100	Unstabilized
U2	300	250	Unstabilized
U3	300	1500	Unstabilized
U4	300	4000	Unstabilized
F1	300	100	Fain stabilized
F2	300	250	Fain stabilized
F3	300	1500	Fain stabilized
F4	300	4000	Fain stabilized

A simple bloating index from 0 to 4 was used to rank the panels as they appeared coming out of the carbonization furnace. The panels made with pitch stabilized according to Dr. C. C. Fain’s process did not bloat at all. They also had better char yields than the composites made with unstabilized pitch (see Table 16). The ILTs of these carbonized composites was

TABLE 16
CARBONIZATION RESULTS FOR "FAIN" STABILIZED PITCH COMPOSITES

Sample	Matrix Char Yield (%)	Bloating Index	Interlaminar Tensile Strength (psi)
U1	74	2	66.1
U2	59	3	60.2
U3	81	0	177.5
U4	77	1	69.4
F1	81	0	44.5
F2	71	0	20.8
F3	83	0	12.1
F4	80	0	79.7

measured and all were very low. The composites made with the Fain stabilized pitches had lower ILTs than the unstabilized pitch even though the bloating was much less.

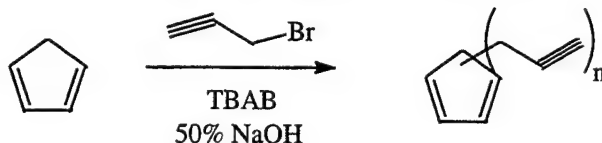
Again, the difficulty in getting the pitch uniformly dispersed within the fiber bundles was a problem. Additional work in this area will be conducted when good penetration of the pitch into fiber bundles can be accomplished.

4.6 EVALUATION OF A NEW HIGH CHAR YIELD RESIN

Carbon-carbon composites are composed of carbon fibers held together by a carbon matrix. A fiber preform and a matrix capable of carbonizing are pyrolyzed. The char yield or amount of carbon that remains as part of the matrix determines how many times a resin is reimpregnated into the composite and pyrolyzed. The lower the char yield of the matrix, the more reimpregnation and pyrolysis steps are needed to fully densify the carbon-carbon composite.

The class of polymers examined here is based on propargyl substituted cyclopentadiene. This work was started in the previous year [29]. This resin is composed of 95 percent carbon by weight and has the potential of producing a very high-char yield composite. TGA measurements showed up to 95 percent char yield in the composites and over 80 percent in neat resin samples.

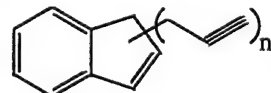
Propargyl- and mixed allyl-/propargyl-cyclopentadiene (PCP & APCP) and propargyl-indene (PI) polymers form the family of high-char yield resins examined as potential matrices for carbon-carbon composites. The resins are synthesized using a five-membered unsaturated ring base, a propargyl halide, and a phase change catalyst in a basic environment [33]:



Several ($n = 2$ to 6) of the propargyl groups add to the ring. The unsaturated additions thermally decompose to form free radicals which can add to other triple or double bonds producing a crosslinked polymer network. Some polymerization begins during the original synthesis, but if kept away from oxygen, the resin remains as a low-viscosity fluid for a long time at room temperature. Allyl halides can be substituted for propargyl or a mix used. Other five-member unsaturated rings can be used instead of cyclopentadiene, such as indene.



APCP



PI

where $n + m = 2$ to 6 in APCP and

$n = 2$ to 4 in PI

4.6.1 SMU Composites

In the first phase of this work, the composites were made at Southern Mississippi University from resin they synthesized. The basic resins were infiltrated into the fibers or preforms which had been placed in a mold. The resin was poured into the mold over fibers and additional fibers and resin added to complete the composite. The mold was heated under sufficient pressure to squeeze out some resin to ensure the fibers were completely wet by the resin. The mold was heated to 250°C and then to 350°C and held for 4-6 hours to completely cure the resin [34 and 35]. The three resins examined in this study were a propargyl-substituted cyclopentadiene (PCP), a 3:1 allyl:propargyl-cyclopentadiene (APCP) and a propargyl-indene (PI). The three fiber forms examined were the ThermalGraph® 6000X preform from AMOCO, a uniaxial AS-4 hand lay-up, and a T-300 plain-weave multi-ply lay-up.

Interlaminar tensile strength (ILT) specimens (average of three for each composite) were cut after carbonization for a modified button measurement. The composites

were carbonized by heating at 2°C/min. to ~900°C in a nitrogen atmosphere. Microscopy samples were cut from samples before and after carbonization. The samples were vacuum infiltrated with a fluorescently dyed potting resin and then polished by ordinary resinographic techniques. The polished plugs were examined with a Nikon Optiphot FXL microscope in both bright-field and fluorescent illumination. Images were obtained using 35-mm film and a CCD digital camera. Image-1 image processing software was used to measure the fiber volumes and void content in the composites. Density measurements were made on composite specimens using the Archimedes displacement method with water and on cured neat resin specimens using a pycnometer and toluene.

The results of this study are summarized in Table 17 for the carbonization char yields, microscopy, and interlaminar tensile testing. They were also the subjects of two papers presented at national meetings [35 and 36].

Fiber volumes were measured in the as-cured composites and are shown for within bundles for the woven fiber composites or in the regions away from large voids for the other fiber composites. The overall fiber volumes are also calculated. Reasonable fiber volumes were obtained in these composites: 54 to 62 percent in woven bundles and 51 to 66 percent in the other composites.

Char yields for the composites were calculated from weight loss during carbonization. The matrix char yields were calculated based on the total char yield, measured fiber volumes and measured resin density (1.54 g/cm³). The density of the resin had to be measured using toluene because the resin was highly hydrophobic.

The apparent material density of the composites was measured and, because of the high resin density and high fiber content, was dominated by the density of the respective fibers. The cured composites had bulk densities of 1.4 g/cm³ (AS-4 and T-300 composites) and 1.65 g/cm³ (ThermalGraph® 6000X composites).

The percent voids in the as-cured composites were high relative to typical composites indicating that the processing was less than optimum. After carbonization, the void level increased as expected. The PCP composites all had void contents typical of that found in carbonized phenolic composites (14-19 percent). The PI composites had a larger void volume of 32 percent, and the APCP composites was even higher (see micrographs in Figures 71 and 72).

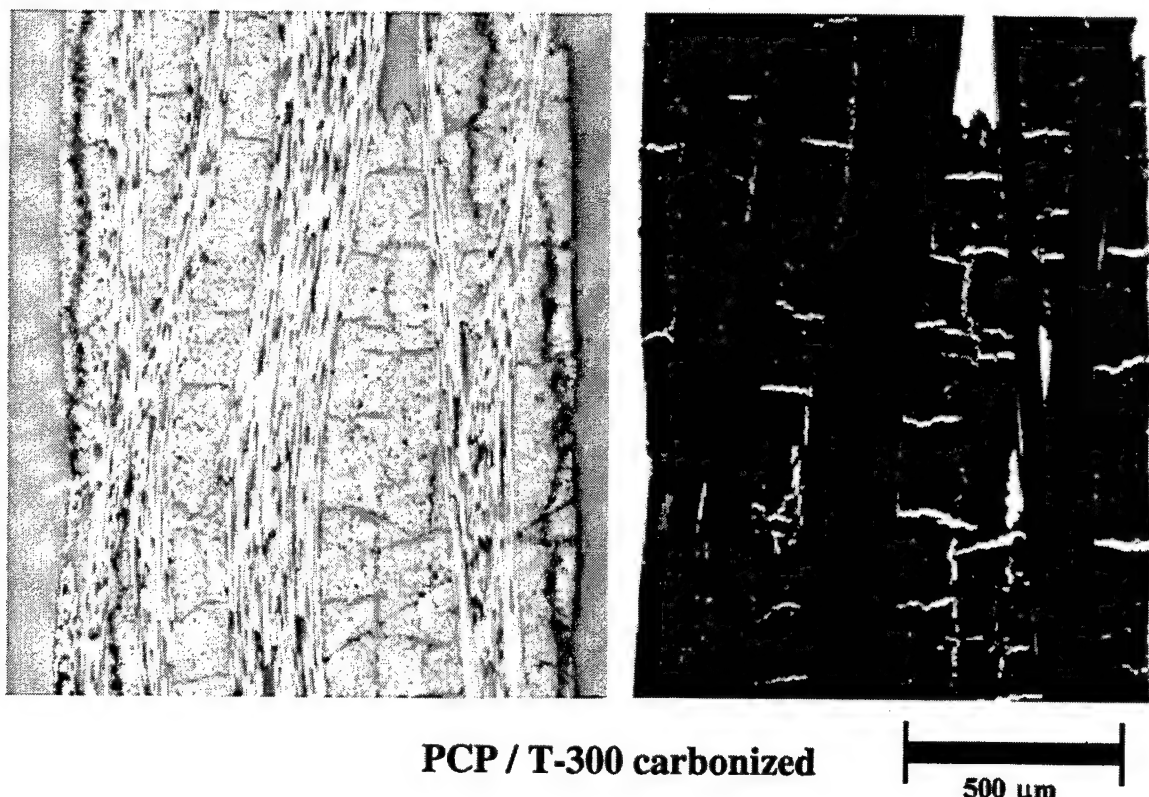


Figure 71. Bright-Field and Fluorescence Optical Micrographs of PCP Composites.

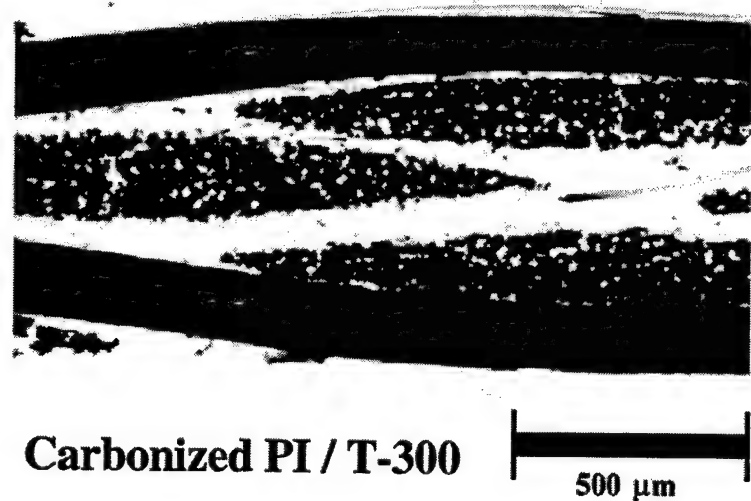


Figure 72. Fluorescence Optical Micrograph of a PI Composite.

TABLE 17
SUMMARY OF RESULTS FOR PCP COMPOSITES

Resin	Fiber	Fiber Volume (%)		Matrix Char (%)	Voids (%) As-cured	Carbonized	Interlaminar tensile strengths	
		Overall	Bundle				(MPa)	(psi)
PCP	ThermalGraph®	63.2	66.0	80	4.3	19.2	2.07	300
PCP	AS-4	48.2	51.2	77	5.9	17.6	1.00	145
PCP	T-300	55.2	62.0	75	6.4	13.6	1.30	189
APCP	T-300	48.6	54.0	55	5.6	58.0	Na	Na
PI	T-300	52.8	58.0	68	5.0	32.4	Na	Na

After carbonization, the PI and APCP composites could not be tested for ILT; the composites fell apart during cutting. The PCP composites were tested and found to have reasonable strengths (1 to 2 MPa). These are the same general strengths as carbonized phenolic composites.

Composite density measurements (Archimedes displacement) gave bulk densities of 1.61 g/cm³ for the PCP/ ThermalGraph® 6000x composites with apparent material densities of 1.93 g/cm³. The material densities are consistent with the high fiber density of the ThermalGraph® 6000x. Carbonized composites had bulk densities of 1.62 g/cm³ on the ThermalGraph® 6000x composites and 1.37 g/cm³ on AS-4 and T-300 composites reflecting the increased void fraction after carbonization.

Propargyl-substituted resins (PCP) do show promise as carbon-carbon composite matrix resins with ILT strengths of the carbonized composite better than similar carbonized phenolic composites. This matrix has 77 percent resin char yield in the composites. The mixed allyl- and propargyl-cyclopentadiene and propargyl-indene matrices lost too much mass in their composites for use as carbon-carbon matrix resins.

4.6.2 In-House Composites

A mixed allyl and propargyl cyclopentadiene resin was synthesized in-house and made into a composite using T-300 plain-weave fabric. The resin behaved as expected from the literature and proved to be reasonably easy to make. This APCP composite was carbonized to give an overall 90 percent char yield.

A larger amount of the pure PCP resin from Southern Mississippi University was also made into a composite but because of changes in the availability of the process equipment, the composite was cured in a press open to the air. An exotherm in the resin ruined the experiment and no composite was produced.

A small amount of the neat propargyl cyclopentadiene resin was cured to obtain samples for density measurements. The resin was oven cured between flat plates at 250°C for several hours without an exotherm problem. Pycnometry on this resin using water proved to be difficult due to the resin's high hydrophobic nature. Toluene used as a solvent produced a resin density of 1.16 g/cm³. The density of the carbonized resin was measured at 2.0 g/cm³ by the same technique. X-ray diffraction of the carbonized resin clearly showed the presence of graphene sheets but no graphitic order. The latter is not unexpected, given the maximum resin temperature was only ~900°C.

4.6.3 In-House Resin Synthesis

Synthesis of propargyl cyclopentadiene resin (PCP) was attempted. The initial attempt demonstrated the need to completely eliminate oxygen during synthesis. Synthesis of all allyl- and 3:1 mixed allyl- and propargyl-cyclopentadiene resins (ACP and APCP) was completed without difficulty in a hood. Synthesis of 1:1 mixed allyl- and propargyl- and all propargyl-cyclopentadiene resins (APCP and PCP) was completed in a glove box. This proved successful in eliminating oxygen from the system and no curing of the resin was evident.

Prepreg was fabricated from AS-4 fiber and both epoxy and phenolic resins (SC1008) for use as reference materials (SC1008). Panels were laid up from this prepreg and cured. Similar work winding prepreg with the ACP and APCP resins was not as successful. The new resins have turned out to have viscosities too low to give sufficient tack to the wound fiber prepreg for subsequent handling. Only a few of the planned panels could be laid-up.

Thermal analysis and viscosity measurements were made on all the resins. The new resins did not show a significant viscosity rise until ~250°C, by which time they had lost a considerable amount of mass. Volatile material amounting to 50 percent of the total mass has been measured coming off the resin mixtures; work is now underway to determine if this is simply unreacted starting material (very likely from the literature) or something else. If it is

unreacted starting material then it could be recycled in a production environment; however, the economics of this class of resins will be less attractive.

Experiments infiltrating fiber preforms (RTM or VARTM) will be conducted using these new resins if the volatile problem is solved. Concern over health and safety issues prevent any curing of composites until the volatile material is removed. Since considerable effort has been expended synthesizing these resins, the infiltration experiments will be done only after the volatile analysis is complete.

4.7 PITCH-BASED GRAPHITIC FOAMS

Graphitic foams produced by Air Force engineers have developed to the point of refining the processing parameters to obtain desired porosity and bubble sizes. Work was initiated to gather measurements on foams in a systematic fashion in coordination with government processing studies. Microscopy using fluorescent and polarized light was performed to obtain microstructural data and Archimedes displacement measurements were obtained for density.

Mitsubishi AR pitch is jet milled into 1-2 μm sized powder, the powder pressed into short round cylinders (or pucks). The pucks are placed in a pressure reactor vessel, pressurized with gas, heated to temperature, and pressurized to the final pressure. After the desired time at temperature and pressure, the pressure is released which foams the liquid pitch and simultaneously lowers the temperature to solidify the pitch. The foam puck is immediately removed to a stabilization oven and then carbonized.

4.7.1 Foams Produced Using Nitrogen Gas

Eight foam samples were obtained using a statistical 2^4 matrix of processing parameters; two levels of four parameters. In this study, the blowing gas for foaming was nitrogen. The processing parameters varied, which included initial gas pressure (at start of pitch heat up), the final gas pressure (before release for foaming), the final temperature in the vessel, and the time held temperature and pressure.

These foams had porosities of 41 to 90 percent with consistent results between the two methods of measurement (see Table 18). The microscopy estimate of the foam cell sizes showed the lower porosity samples having the smaller more uniform cells. The apparent material density of the foams averaged 1.9 g/cm^3 . Other details of this work have been published [37].

TABLE 18

PROCESSING AND CHARACTERIZATION OF FOAMS PROCESSED WITH N₂.

Initial Pressure	Processing			Characterization			
	Final Pressure	Foaming Temperature	Hold Time	Porosity (microscopy)	App. Bulk Density g/cm ³	Apparent Density g/cm ³	Porosity (displacement) %
500 psi	1500 psi	270 °C	30 min	87.6 %			
500 psi	1500 psi	250 °C	15 min	86.2 %	0.282		
200 psi	1000 psi	270 °C	30 min	79.0 %			
500 psi	1000 psi	250 °C	30 min	41.2 %	0.8		
200 psi	1000 psi	250 °C	15 min	37.1 %			
500 psi	1000 psi	270 °C	15 min	78.5 %	0.186	1.927	90.4 %
200 psi	1500 psi	250 °C	30 min	43.7 %	0.177		
200 psi	1500 psi	270 °C	15 min				

4.7.2 Foaming Produced Using Carbon Dioxide Gas

Eight foam samples were obtained using a statistical 2^3 matrix of processing parameters; two levels of three parameters. In this study, the blowing gas for foaming was CO₂. The processing parameters varied, which included gas pressure (the initial pressure was set to obtain the desired final gas pressure after the gas was heated), the final temperature in the vessel, and the time held temperature and pressure.

These foams had porosities of 43 to 94 percent with consistent results between the two methods of measurement (see Table 19). The microscopy measured the foam cell sizes; three of the blowing conditions produced cells 40 to 50 μm in diameter with the other conditions having considerably larger cells. The apparent material density of the foams was 1.8 g/cm³. Other details of this work have been published [38].

Again the conclusion from this study was that the lower temperature gave smaller cell sizes which gave the foams better mechanical properties. The other two parameters didn't produce any significant structural variations.

4.7.3 Modeling of Bubble Growth

The geometric model bubble growth model developed several years ago [39] to calculate the strain in foam ligaments was reprogrammed. The calculations can now be done in Excel for whatever expansion range is desired. Ligament strain can be calculated as a function of volumetric expansion along with porosity and other related parameters. Measurements of local alignment and mechanical response are now needed to verify and expand the model. A comparison of the model to the porosity measurements in the CO₂ processing experiment is shown in Figure 73.

The porosity versus volume expansion results for the CO₂ foams matched the model trends very well; the absolute measured values were about 10 percent high. This is most likely a result of the model assuming completely uniform expansion which may not be the case in actual foams. Skin layers and uneven expansion near the edges may account for the discrepancy. More work is needed to obtain a wider range of foam measurements to compare to the model.

TABLE 19
PROCESSING AND CHARACTERIZATION OF FOAMS PROCESSED WITH CO₂

Initial Pressure	Processing			Mechanicals			Characterization				
	Final Pressure	Foaming Temp.	Hold Time	Modulus	Strength	Porosity (microscopy)	Estimated Pore size	Density	App. Bulk Density	Apparent Density	Porosity (displacement)
455	1007	270	30 min	0.64 ksi	0.081 ksi	94.6 %	301 μm	0.106 g/cm ³	1.806 g/cm ³	94.1 %	
460	1023	270	15	1.04 ksi	0.041 ksi	93.9 %	339 μm	0.137 g/cm ³	1.720 g/cm ³	92.1 %	
658	1579	270	30	34.0	0.356 ksi	84.8 %	297 μm	0.352 g/cm ³	1.899 g/cm ³	81.4 %	
656	1420	270	15	35.8	0.374 ksi	78.6 %	262 μm	0.288 g/cm ³	1.860 g/cm ³	84.5 %	
468	946	260	15	38.0	0.987 ksi	68.3 %	217 μm	0.378 g/cm ³	1.810 g/cm ³	79.1 %	
678	1519	250	15	584.	7.75 ksi	64.4 %	35 μm	0.735 g/cm ³	1.568 g/cm ³	53.1 %	
474	1001	250	30	723.	15.00 ksi	45.8 %	45 μm	1.013 g/cm ³	1.778 g/cm ³	43.0 %	
680	1579	250	30	666.	10.58 ksi	47.8 %	40 μm	0.866 g/cm ³	1.658 g/cm ³	47.8 %	

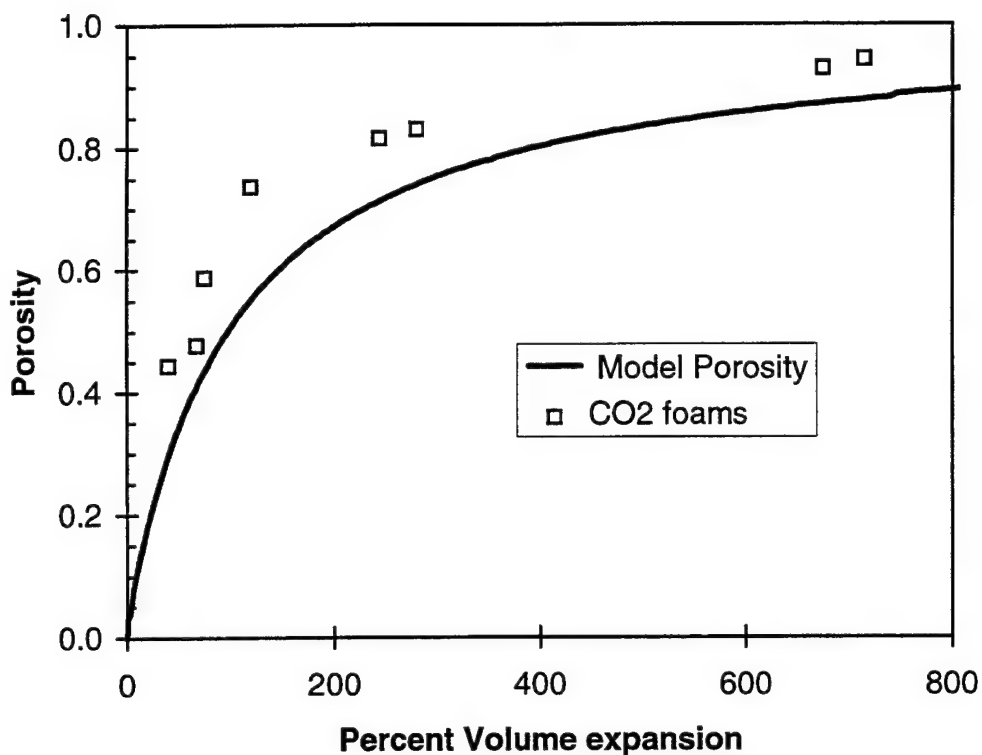


Figure 73. Comparison between Model Predictions and Measured Porosity versus Volume Expansion in CO₂ Blown Carbon Foams.

4.7.4 Foam Net-Shape Processing - Microscopy Studies

Government in-house researchers produced four foam specimens. These foams were several attempts to produce net-shape forms. Details of the foam uniformity, cell sizes, and differences among the production techniques were desired.

As part of the Wright Connection teachers' programs for the Air Force, these foams were characterized by microscopy. This contract's personnel were directly involved in helping the teachers plan the sample cutting and observation; instructing the teachers in techniques involved in sample preparation, microscopy, and image manipulation; and almost exclusively in the final measurements and interpretation of the data.

The four samples and their methods of production are listed in Table 20 and photographs are shown in Figure 74. The three production methods were: extruded, molded, and free expansion. Extruded meant that a normal discotic preform was foamed and the still hot foam was pressed (or extruded) into a mold of the desired shape (rectangular in all of these samples). Molded means a foam preform was placed within a metal mold in the foaming

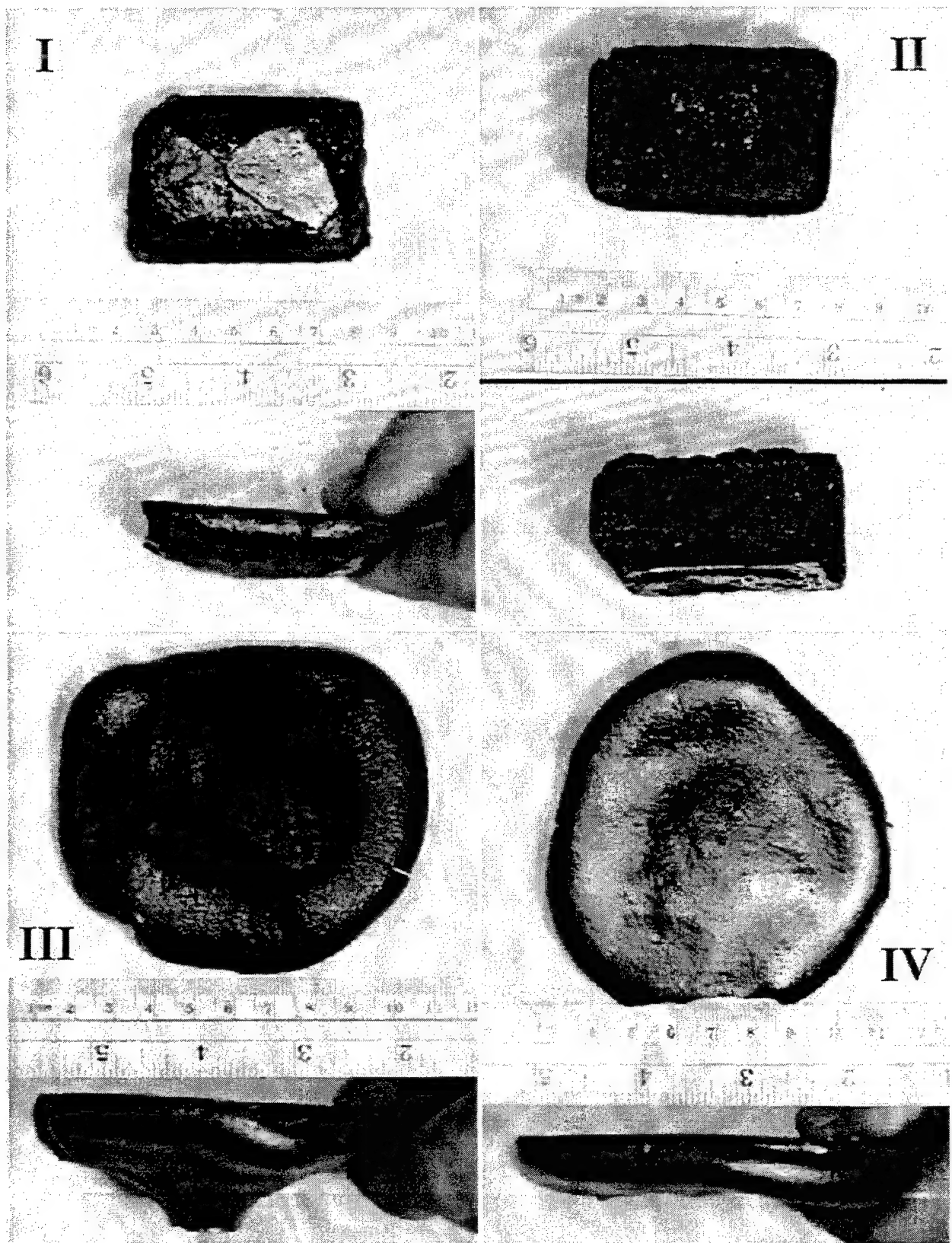


Figure 74. Photographs of "Net-Shaped" Foams.

TABLE 20
NET-SHAPED PROCESSING SAMPLES

Sample Number	Production Number	Production Method
I	053097A	Extruded
II	060397A	Molded
III	060397B	Free Expansion
IV	060397C	Free Expansion

chamber and allowed to foam and fill the mold. The mold was open on the top and bottom so as not to restrict the height of the final foam. Free expansion consisted of cutting the preform into the desired cross-section before foaming and allowing the foam to expand without restriction.

Nitrogen was used as the foaming gas in all the foams under identical temperature and pressure conditions. The foams were oxygen stabilized and carbonized using the standard conditions used for all foams. Samples I and II retained their rectangular cross-sectional shape forming rounded rectangular parallelepiped solids referred to simply as "rectangular". Samples III and IV expanded into roughly circular cross-sectional shapes forming short cylinders or disks referred to as "cylindrical".

After carbonization, the foams were cut into several pieces to allow the observation of the bubbles at several locations and orientations. Figure 75 shows a schematic of the rectangular samples' cutting diagram. Each quadrant was cut from the foam and three of those quadrants cut to expose surfaces facing in different directions. Quadrant A was reserved for SEM and other tests. Quadrant B was cut to reveal surfaces normal to the foam's long in-plane direction, quadrant C was cut to reveal surfaces normal to the foam's short in-plane direction, and quadrant D was cut to reveal surfaces normal to the through-the-thickness direction.

The cylindrical foams were cut according to the diagram in Figure 76. One half of the sample marked "A" was kept for SEM and other tests. Other specimen's cut were "B" to reveal surfaces normal to the cylinder radial direction, "C" to reveal surfaces normal to the hoop direction, and "D" was cut to reveal surfaces normal to the through-the-thickness direction.

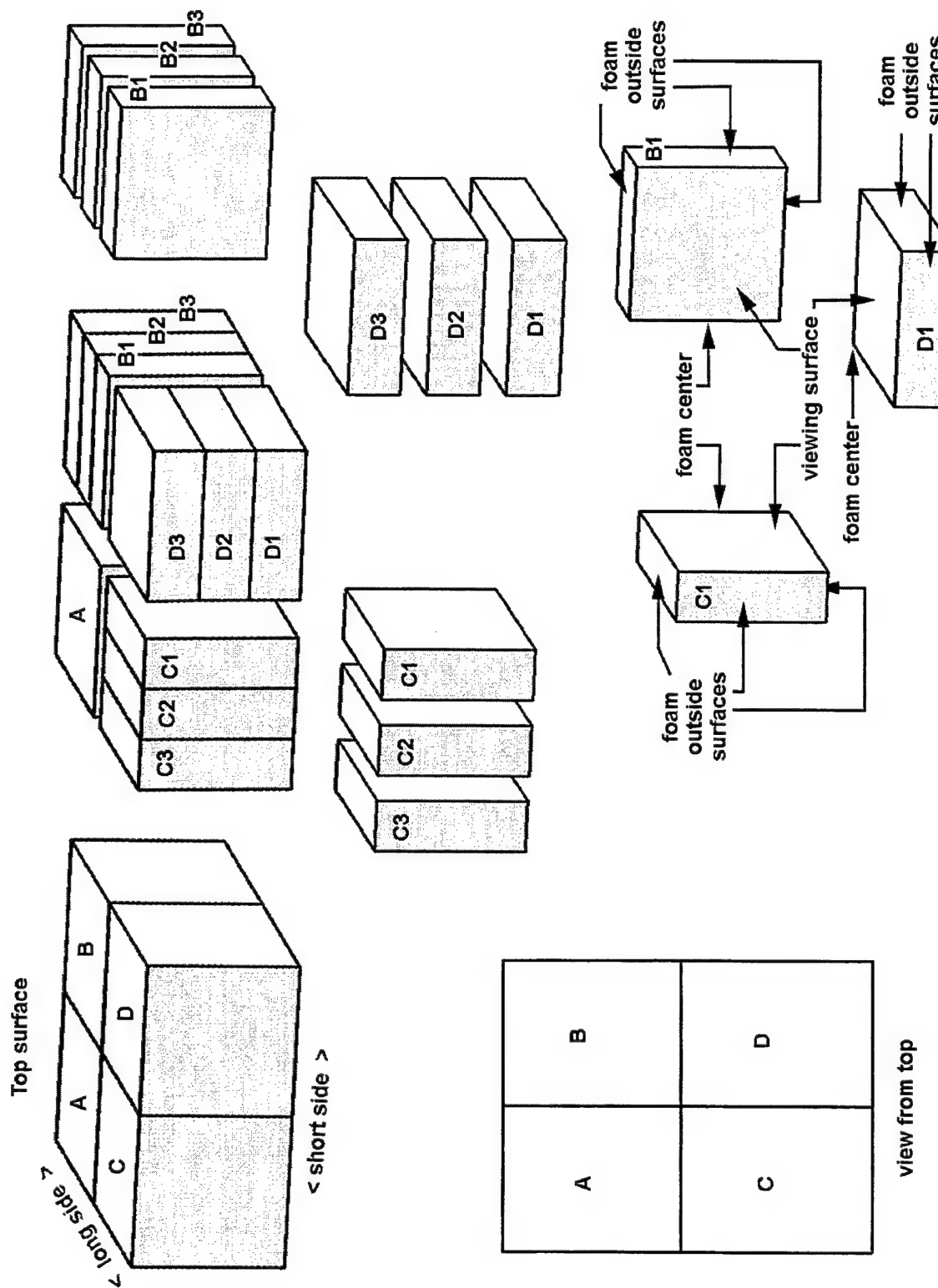


Figure 75. Cutting Diagram for the Rectangular Foam Blocks.

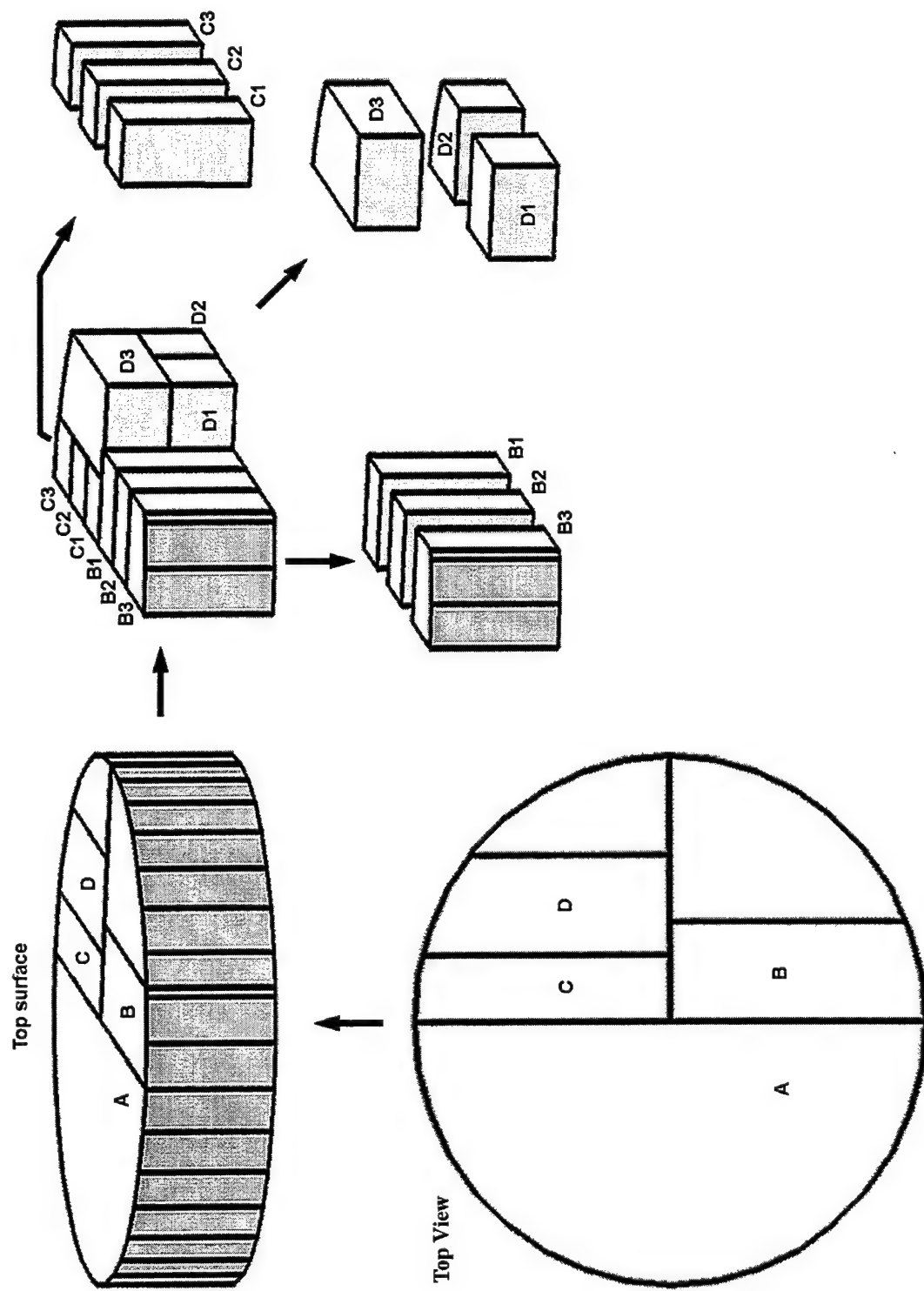


Figure 76. Cutting Diagram for the Cylindrical Foam Blocks.

Great care was taken to mark and maintain the sample orientations so that it would be known where in the samples the micrographs were obtained from and in what direction the surfaces were facing. These cut specimens were potted in fluorescent resin and polished. Over 4,000 digital photographs were obtained by the Wright Connection teachers on the optical microscope.

Image analysis of the images to measure porosity was straightforward. There did not appear to be a significant variation in porosity as a function of processing path, position in the foam samples or orientation of observation. The foams had average porosity values of 81 to 82 percent. Deviations from the average in any particular view were due more to potting resin infiltration differences than from sample variations.

Measurement of the bubble sizes was not as easy. The usual automated measurements are based on the assumption that each bubble can be separated from its neighbor by the cell wall. Then by measuring the observed bubble diameter or intersection lengths the true average diameter can be calculated. In the open celled carbon foams, the bubble walls have collapsed (at least partially) making it impossible for the computer to separate cells. The human eye can distinguish the individual bubbles using subtle clues; however, our current software is incapable of recognizing those clues.

Measuring the bubble diameters on images is tedious and time consuming but a good estimate of sizes can be obtained by measuring the number of bubbles in a fixed area. Square images (selected from a larger one from the regions of interest) all the same size were used. The bubbles completely enclosed by the square and those partial bubbles crossing the boundary in only one direction are counted. That is to say one counts the partial bubbles crossing the left edge but not the right edge (and top but not bottom) so that the area covered by the counted bubbles are consistent. By knowing the area of the square, the number of bubbles enclosed in that area, and simple geometry an average diameter can be calculated. This method was used to measure the average cell sizes shown in the following figures.

Figure 77 shows the cell (or bubble) sizes as a function of viewing direction in the center of each specimen. The B samples were cut to view along the long or radial directions of the foams, C samples were cut to view along the short or hoop directions, and D samples were cut to view along the z-axis or through-the-thickness direction. Basically, no major differences

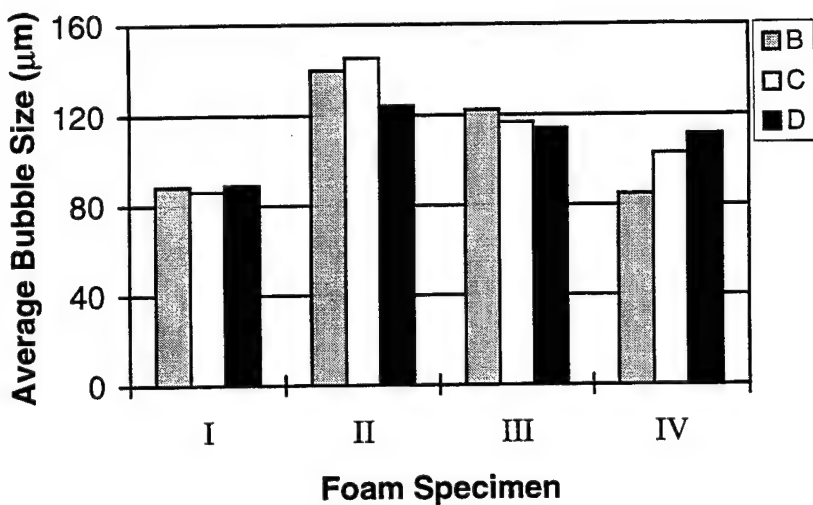


Figure 77. Average Bubble Sizes in the Center of the Foam Specimens as a Function of Viewing Direction. B is along the long or radial direction, C is along the short or hoop direction, and D is along the z-axis or through-the-thickness direction.

were noted which means that the bubbles are isotropic in this part of the foams. There were some differences among the foam specimens but this can be seen more easily in Figure 78. This figure shows the average bubble sizes in the central part of the foam specimens as a function of location within the foam. The measurements were taken at the center of the foam and then at several other locations towards the outer part, but not to the very edges of the foams. The

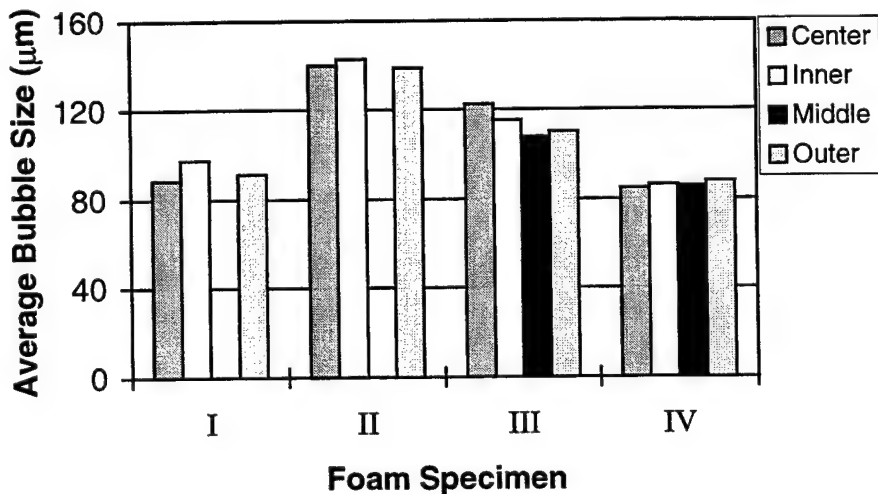


Figure 78. Average Bubble Sizes in the Central Part of the Foam Specimens as a Function of Location from the Center of the Foam to the Outer Part (But Not at the Edges).

average bubble size of foams I and IV is slightly more than 80 μm , foam III is 110 to 120 μm , and foam II is about 140 μm . The difference in the largest to smallest bubble sizes is shown in Figure 79. More interesting is the differences from the center of the foams to the outer edges. Figure 80 shows the size averages. Only foam II appears to show much difference with the edges having a much smaller average size bubble than the center areas. What is not reflected in this figure is that the regions picked to count cells deliberately avoided some regions. In foam I there were regions containing collapsed cells, apparently crushed during the extrusion operation. This is shown in Figure 81. Also, very large cells several millimeters in diameter were present in the latter three foams especially along the bottom edge, these regions were also avoided. These very large bubbles can be seen in Figure 82.

Cell size and porosity was relatively uniform for all the "net-shape" processing samples. Extrusion apparently crushes some cells but this could be dependent on the temperature of the foams and extruding molds which was not examined. Foaming a shaped preform without restrictions results in a circular foam the same as a circular preform. Foaming into a mold produces the best net shape, the final foam retaining the shape of the mold.

4.8 AD HOC ACTIVITIES

Thermal diffusivity equipment: A FORTRAN program was written to curve fit the temperature change versus time data. The results are both quickly attained and in good agreement with other methods of analysis. The results from the program on data collected in-house were in good agreement with results from other laboratories on the same samples.

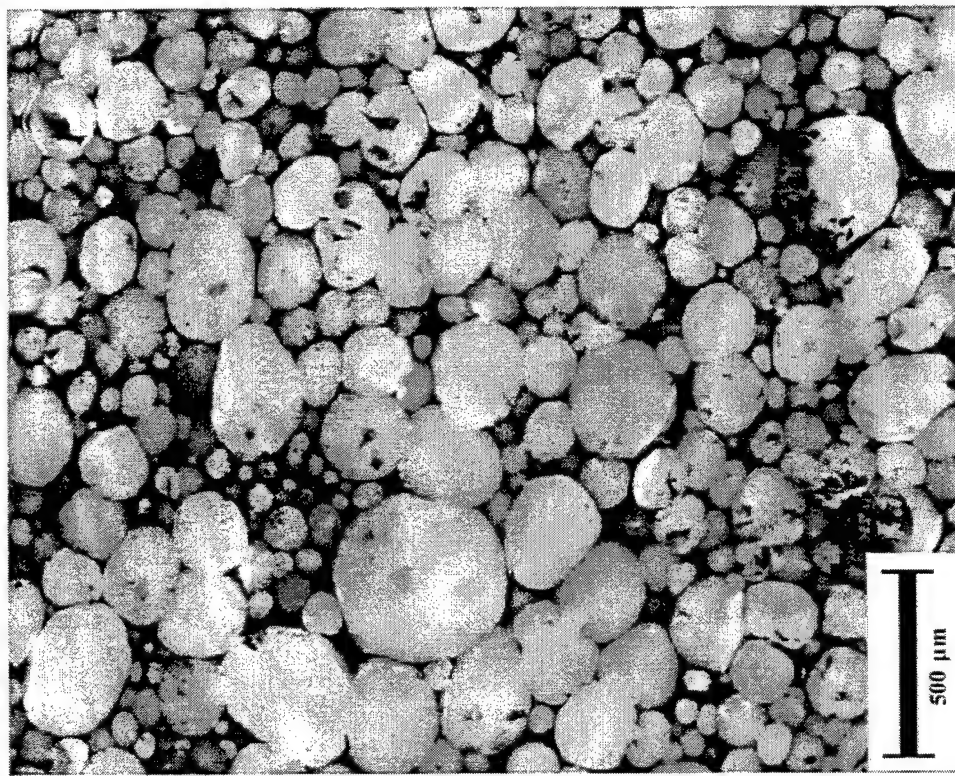
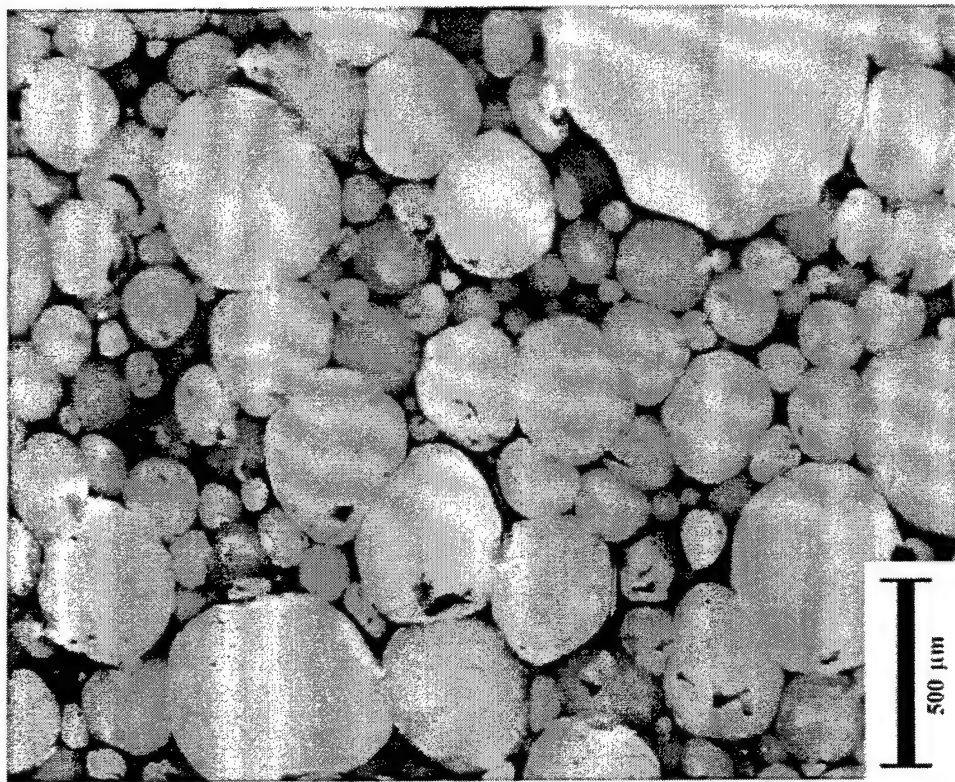


Figure 79. Examples of Small-Cell (Left) and Large-Cell (Right) Regions in Foams.

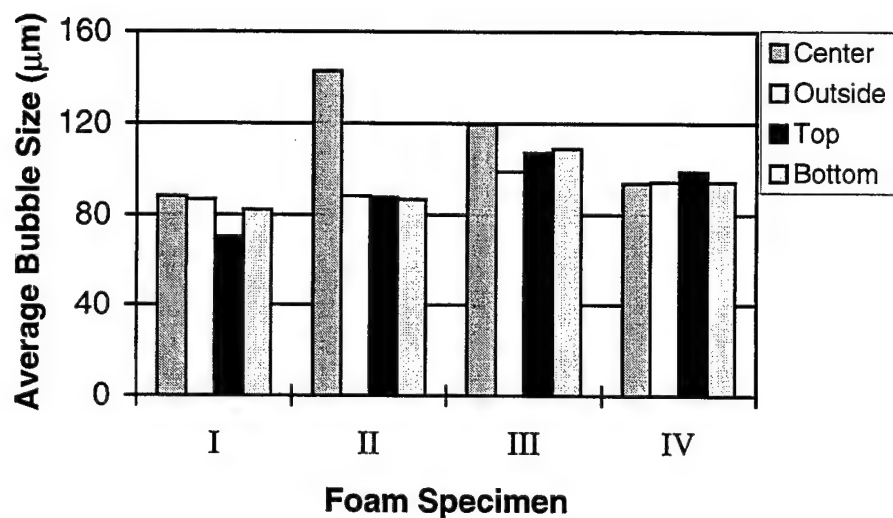


Figure 80. Average Bubble Sizes in the Central Part of the Foam Specimens as a Function of Position from the Center of the Foam to the Outside Edge, Top Edge and Bottom Edge.

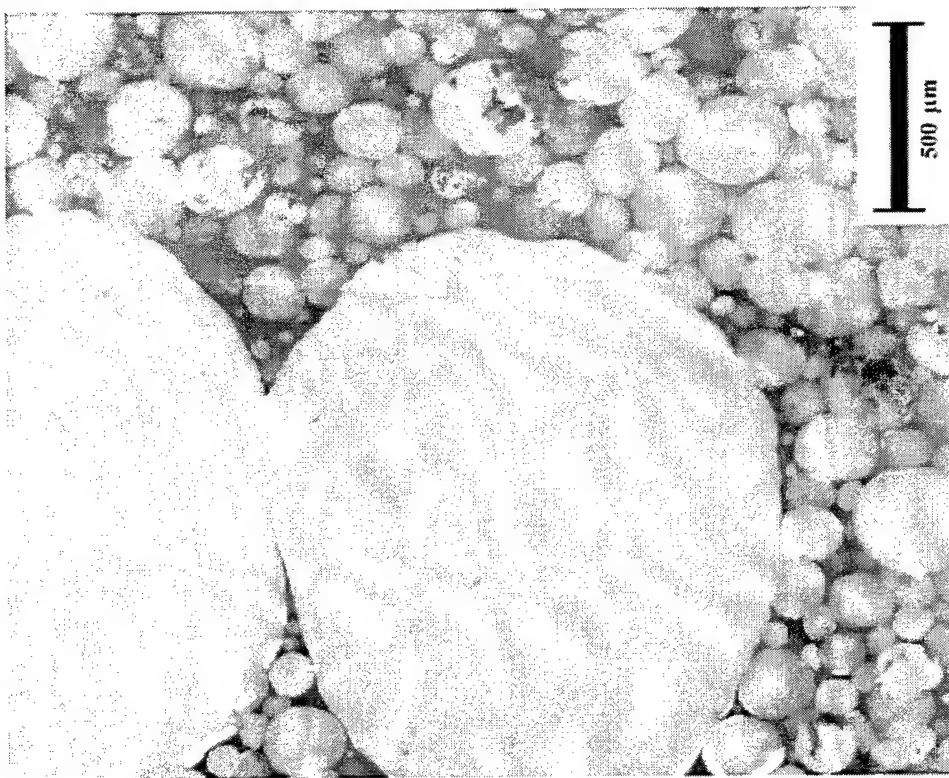


Figure 82. Example of Occasional Very Large Cells.

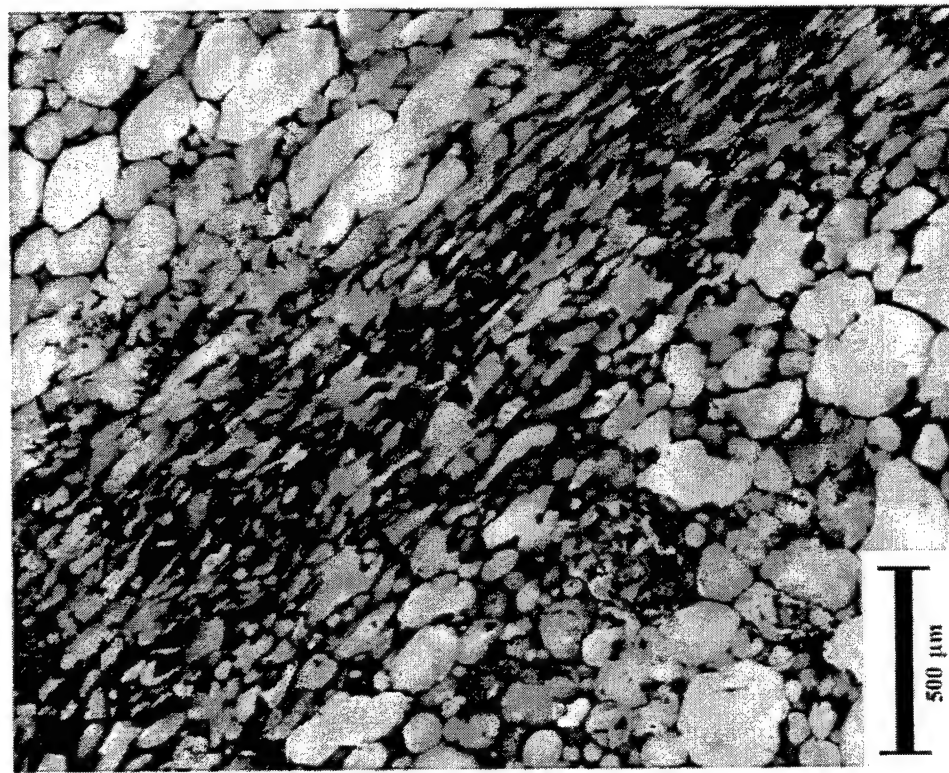


Figure 81. Example of Crushed Cells.

SECTION 5

REFERENCES

1. Saunders, C. B., et al. (1993). Characterization of Matrix Polymers for Electron-Beam-Cured Fiber-Reinforced Composites. *Irradiation of Polymeric Materials*. ACS Symp. Series No. 527, E. Reichmanis, C. Frank and J. O'Donnell, eds. American Chemical Society (p. 305).
2. Iverson, S. L., et al. (1992). Radiation Curable Composites: Environmental Advantages. *Proc. Int. Symp. on Applications of Isotopes and Radiation in Conservation of the Environment*, Karlsruhe, Germany, International Atomic Energy Agency, Vienna.
3. Crasto, A. S., R. Y. Kim and J. P. Mistretta. (1996). Rehabilitation of Concrete Bridge Beams with Externally-Bonded Composite Plates. Part II. *Int. SAMPE Symp. 41* (pp. 1269-1279).
4. Bishopp, J. A., L. Davies and J. J. Haslam. (1993). Chemical and Mechanical Characterization of Adhesive Matrices. *Int. J. of Adhes. and Adhes. 13* (2) (pp. 111-119).
5. Ahn, K. J., Y. S. Eom, Y. T. Shim and J. C. Seferis. (1994). Characterization of Structural Adhesives for Load-Bearing Composite Structural Applications. *Composite Structures 27* (pp. 57-64).
6. Crasto, A. S., R. Y. Kim, C. Fowler, and J. P. Mistretta. (1996). Rehabilitation of Concrete Bridge Beams with Externally-Bonded Composite Plates. Part I. *Int. Conf. on Composites in Infrastructure 1* (p. 857).
7. Park, C. H. and H. L. McManus. (1994). Thermally Induced Damage in Composite Space Structures: Predictive Methodology and Experimental Corelation. *Proc. of American Society of Composites 9* (pp. 161-168).
8. McManus, H.L., D. E. Bowles, and S. S. Tompkins. (1996). Prediction of Thermal Cycling Induced Matrix Cracking. *J. Reinforced Plast. Compos. 15* (pp. 124-139).
9. Kim, R. Y. and A. S. Crasto. (1995). Dimensional Stability of Composites in Space: CTE Variations and Their Prediction. *Proc. Int. Conf. Compos. Mater. ICCM-10, Vol. IV* (p. 513).
10. Kim, R.Y., A. S. Crasto, and G. A. Schoeppner. (1997). Measured and Predicted Changes in Laminated CTE Due to Microcracking. *Proc. of the American Society for Composites, Technomic*.
11. Schoeppner, G. A. and N. J. Pagano. (1997). Stress Fields and Energy Release Rates in Cross-Ply Laminates. *International Journal of Solids and Structures*.

12. Reissner, E. (1950). On a Variational Theorem in Elasticity. *Journal of Mathematics and Physics* 29 (pp. 90-95).
13. Pagano, N. J., G.A. Schoeppner, R. Y. Kim and F. L. Abrams. (1997). Steady State Cracking and Edge Effects in Thermo-Mechanical Transverse Cracking of Cross-ply Laminates. Paper presented at ASME Summer Meeting in Chicago, IL.
14. Donaldson, S. L. and A. K. Roy. (1997). Experimental Studies on Composite Bonded Joints. Presented at the 11th International Conference on Composite Materials (ICCM-11), Australia.
15. Chin, J. W. and J. P. Wightman. (1996). Surface Characterization and Adhesive Bonding of Toughened Bismaleimide Composites. *Composites: Part A*, Vol. 27A. (pp. 419-428).
16. Schoeppner, G. A. and N. J. Pagano. (1996). Stress Fields and Energy Release Rates in Cross-Ply Laminates. Submitted to *International Journal of Solids and Structures*.
17. Bogdanovich, A. E. and N. Rastogi. (1996). 3-D Variational Analysis of Bonded Composite Plates. *Proceedings of the ASME Aerospace Division*, AD-Vol. 52. 1996 International Mechanical Engineering Congress and Exposition, Atlanta, GA. (pp. 123-143).
18. Roy, A. K. (1994). Experimental Observation of Damage in 8HS Fabric Composites in Tensile Loading. *Proc. 9th Technical Conference*. American Society for Composites. Technomic Publishing. Lancaster, PA. (pp 1273-1280).
19. Zhang, Y. C. and J. Harding. (1990). A Numerical Micromechanics Analysis of the Mechanical Properties of a Plain Weave Composite. *Computers and Structures*. Vol. 36. No. 5 (pp 839-844).
20. Naik, N. K. and V. K. Ganesh. (1992). Prediction of On-axes Elastic Properties of Plain Weave Fabric Composites. *Composites Science and Technology*. Vol. 45 (pp 135-152).
21. Hahn, H. T. and R. Pandey. (1994). A Micromechanics Model for Thermoelastic Properties of Plain Weave Fabric Composites. *Journal of Engineering Materials and Technology*. Vol. 116 (4) (pp 517-523).
22. Yurgartis, S. W. and J. P. Maurer. (1993). Modeling Weave and Stacking Configuration Effects on Interlaminar Shear Stresses in Fabric Laminates. *Composites*. Vol. 24 (pp 651-658).
23. Marrey, R. V. and B. V. Sankar. (1995). Micromechanical Models for Textile Structural Composites. NASA CR 198229.

24. Chou, T. and F. K. Ko. (1989) *Textile Structural Composites*. Chapter 7, Elsevier, New York, USA.
25. Naik, N. K. and V. K. Ganesh. (1994). Failure Behavior of Plain Weave Fabric Laminates Under In-Plane Shear Loading. *Journal of Composites Technology & Research*. Vol 16 (1) (pp 3-20).
26. Karayaka, M. (1994). Deformation and Failure Behavior of Woven Composite Laminates. *Journal of Engineering Materials and Technology*. Vol. 116 (2) (pp 222-232).
27. Whitcomb, J. D. (1991). Three-Dimensional Stress Analysis of Plain Weave Composites. *Composite Materials: Fatigue and Fracture*. Vol. 3 ASTM STP 1110. American Society for Testing and Materials. Philadelphia, PA (pp 417-438).
28. Roy, A. K. (1996). *In Situ* Damage Observation and Failure in Model Laminates Containing Planar Yarn Crimping of Woven Composites. *Mechanics of Composite Materials and Structures*. Vol. 3 (pp 101-117).
29. Crasto, A. S., et al. (1997). *Improved Technology for Advanced Composites* (WL-TR-97-4013) US Air Force Technical Report.
30. Hill C. S., D. P., Anderson, & W. A. Price. (1997). Effects of Pressing Conditions on Sintering of Carbon. *23rd Biennial Conference on Carbon Extended Abstracts*, II.462.
31. Hoffman, W. R. and K. J. Huttinger. (1993). Modeling of the Apparent Viscosity of Pitches and Mesophases at Linear Temperature Increase up to 500°C. *Carbon* 31 263.
32. Corne, L. P. and C.C. Fain. (1993). *Oxygenated Pitch and Processing Same*. U.S. Patent No. 5,225,070 (July 6, 1993).
33. Mathias, L. J. and J. Muthiah. (1994) *Polymer Composites* 15 464.
34. Tregre, G. J. (1997). Ph.D. Dissertation Dept. of Polymer Science, So. Miss. Univ. Hattiesburg, MS.
35. Anderson, D. P., M. I. Martinez, A. K. Roy, G. J. Tregre, and L. J. Mathias. (1997). Carbon-Carbon Composites from a New Class of High-Char Yield Resins. *23rd Biennial Conference on Carbon Extended Abstracts*, II.476.
36. Anderson, D. P., M. I. Martinez, A. K. Roy, G. J. Tregre, and L. J. Mathias (1997). Carbon-Carbon Composites from a New High-Char Yield Resin. Proceedings of at the 21st Annual Conference on Composites, Materials, and Structures held at Cocoa Beach, FL (in press).
37. Kearns, K. M. and D. P. Anderson. (1997). Microcellular Graphitic Foam Processing. *Proceedings of ICCM-1*. Gold Coast. Australia.

38. Anderson, H. J., D. P., Anderson, and K. M. Kearns. (1997). Microcellular Graphitic Foam. *23rd Biennial Conference on Carbon Extended Abstracts*, II.4. Penn State, PA.
39. Anderson, D. P., K. E. Gunnison, and J. W. Hager. (1992). Ligament Structure of Open-Cell Carbon Foams and the Construction of Models Based on that Structure. *Novel Forms of Carbon, MRS Symp. Proc.* 270 47.

PUBLICATIONS, PRESENTATIONS, AND PATENTS

The following is a list of presentations, publications, and patents that were generated during this contractual period.

Roy, A. K. and D. P. Anderson. (1997). *In Situ Damage and Failure Observation in Model Carbon-Carbon Laminates Containing Planar Yarn Crimping*. Paper presented at the 21st Annual Conference on Composites, Materials, and Structures held at Cocoa Beach, FL.

Anderson, D. P., M. I. Martinez, A. K. Roy, G. J. Tregre, and L. J. Mathias (1997). *Carbon-Carbon Composites from a New High-Char Yield Resin*. Paper presented at the 21st Annual Conference on Composites, Materials, and Structures held at Cocoa Beach, FL.

Ciminelli, D., C. S. Hill, and D. P. Anderson. (1997). *Processing of Sintered Carbon for Thermal and Structural Composites*. Paper presented at the 21st Annual Conference on Composites, Materials, and Structures held at Cocoa Beach, FL.

Kearns, K. M. and D. P. Anderson. (1997). *Microcellular Graphitic Foam Processing*. Proceedings of ICCM-11. Gold Coast, Australia

Anderson, H. J., D. P. Anderson, and K. M. Kearns. (1997). *Microcellular Graphitic Foam*. Paper presented at the 23rd Biennial Conference on Carbon at Penn State, PA.

Anderson, D. P. and A. W. Phelps. (1997). *Diamond Structure Observed in Pyrograf-III™ Vapor-Grown Carbon Fibers*. Poster presented at the 23rd Biennial Conference on Carbon at Penn State, PA.

Hill, C. S., D. P. Anderson, and W. A. Price. (1997). *Effects of Pressing Conditions on Sintering of Carbon*. Paper presented at the 23rd Biennial Conference on Carbon at Penn State, PA.

Anderson, D. P., M. I. Martinez, A. K. Roy, G. J. Tregre, and L. J. Mathias. (1997). *Carbon-Carbon Composites from a New Class of High-Char Yield Resins*. Paper presented at the 23rd Biennial Conference on Carbon at Penn State, PA.

Roy, A. K. (1997). *Comparison of In Situ Observation in Unbalance Woven Composite and Model Laminates of Planar Crimping*. Proceedings of 13th Technical Conference of the American Society of Composites.

Roy, A. K. (1997). *Three-Dimensional Mixed Variational Stress Analysis for Textile Composites*. Presented at ASME/ASCE/SES Summer Meeting. Northwestern University, IL.

Donaldson, S. L., J. Y. Song, and A. K. Roy. (1997). *Research Issues in the Repair of Composites*. Presented at the 1997 Offshore Technology Conference, Houston, TX. pp. 209-214.

Donaldson, S. L. and A. K. Roy. (1997). *Experimental Studies on Composite Bonded Joints*. Presented at ICCM-11, Australia.

Roy, A. K., S. L. Donaldson and G. A. Schoeppner. (1997). *Bonded Joints of Unidirectional and Cross-ply Laminates: An Experimental Study*. Presented at the 38th AIAA SDM Conference, Orlando, FL.

Crasto, A. S. and R. Y. Kim. (1996). *Environmental Durability of a Composite-to-Composite Adhesive Bond in Infrastructure Applications*. SAMPE Technical Conference Proceedings. (28) pp. 837-849.

Thorp, K. E., A. K. Roy and A. S. Crasto. (1996). *The Effect of Isothermal Aging on the Relaxation Spectra of AFR700B*. SAMPE Technical Conference Proceedings. (28) pp. 797-806.

Thorp, K. E. and A. S. Crasto. (1997). *The Effect of Aging Environment on the Structure and Properties of AFR700B*. High Temple Workshop Proceedings. (12) pp. K1-K31.

Crasto, A. S. and R. Y. Kim. (1997). *Hygrothermal Influence on the Free-Edge Delamination of Composites under Compressive Loading*. Composite Materials: Fatigue and Fracture (Sixth Volume). ASTM STP 1285, E. A. Armanios, ed., American Society for Testing and Materials.

Crasto, A. S., et al., (1996). *Improved Technology for Advanced Composites*. WL-TR-96-4026. U. S. Air Force Technical Report.

Crasto, A. S., R. Y. Kim J. P. Mistretta and M. Dougherty. (1997). *Rehabilitation of Concrete Bridge Beams with Fiber-Reinforced Composites*. International SAMPE Symposium Proceedings (42).

Crasto, A. S., R. Y. Kim, B. P Rice. (1997). *Electron Beam Cure of Composite for Aerospace Structures*. International Conference on Composite Materials Proceedings, ICCM-11.

Kim, R. Y. and A. S. Crasto. (1997). *Initiation of Free-Edge Delamination in a Composite Laminate under Fatigue Loading*. International Conference on Composite Materials Proceedings, ICCM-11.

Schaff, J. and R. Y. Kim. (1997). *Damage Initiation and Progression for Basic Laminates with Holes Part I. Unidirectional and Angle-ply*. Presented at the ASC Annual Meeting in Dearborn, MI.

Kim, R. Y., A. S. Crasto, and G. A. Schoeppner. (1997). *Measured and Predicted Variation in Laminate CTE due to Microcracking*. Presented at the ASC Annual Meeting in Dearborn, MI.

Pagano, N. J., G. A. Schoeppner, R. Y. Kim, and F. L. Abrams. (1997). *Steady-State Cracking and Edge Effects in Transverse Cracking of Cross-ply Laminates*. Presented at the ASME Summer Meeting in Chicago, IL.

Rice, B. P. and C. W. Lee. (1996). *Novel, Low-Cost Sensors for Intelligent Process Control*. Proceedings of the 28th ACS Central Regional Meeting, Dayton, OH.

Crasto, A., R. Kim, and B. Rice. (1996). *Characterization of Electron Beam-Cured Resins and Composites*. Presented at the Electron Beam Curing of Composites Workshop, Oak Ridge, TN.

Rice, B. P. (1996). *Hygrothermal Studies on Fluorinated Polyimides – A Physical Characterization*. Proceedings of SAMPE Technical Conference 28.

Lee, C. W. and B. P. Rice. (1996). *Modeling of Epoxy Cure Reaction Rate by Neural Network*. Proceedings of SAMPE Technical Conference 28.

Rice, B. P. (1997). *Characterization of High-Temperature Polyimides*. Proceedings of High Temple Workshop XVII.

Crasto, A. S., et al., (1997). *Core Programs of High-Performance Composite Materials*. WL-TR-97-4013.